MSNW

FINAL REPORT
TECHNOLOGY DEVELOPMENT FOR TAPERED-WIGGLER FREE-ELECTRON LASERS

Submitted to
OFFICE OF NAVAL RESEARCH

Submitted by
MATHEMATICAL
SCIENCES
NORTHWEST, INC.

April 1984

C.11.240.01.10

FINAL REPORT

TECHNOLOGY DEVELOPMENT FOR TAPERED-WIGGLER FREE-ELECTRON LASERS

DARPA Order No. 3818

Contract No. N0014-82-C-0704

Contract Effective Date: 1 July 1982

Contract Expiration Date: 29 February 1984

Submitted to

OFFICE OF NAVAL RESEARCH
Arlington, Virginia 22217

By

MATHEMATICAL SCIENCES NORTHWEST, INC.
2755 Northup Way
Bellevue, Washington 98004

Jack Slater
Principal Investigator
(206)827-0460

April 1984

TABLE OF CONTENTS

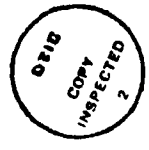

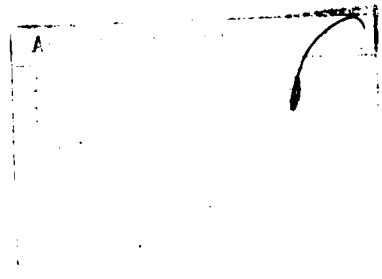

A1

LIST OF FIGURES

LIST OF TABLES

SUMMARY

This report addresses technology required for high-power visible free-electron lasers. The work follows logically from recent demonstrations of electron kinetic energy conversion to optical energy in tapered-wiggler free-electron lasers (FEL). The tapered-wiggler FEL differs from the first demonstrated nontapered version in that it allows a much larger fraction of electron energy to be converted to optical energy in a single pass through the wiggler magnet. This conversion, now demonstrated as high as 4 percent, may lead to high-power, high-efficiency devices if an e-beam recovery stage is added downstream of the wiggler.

The technology addressed is that necessary for the transition from the current 10 μm amplifiers to 0.5 μm oscillators. These two regimes differ dramatically in two ways. First, the physics of the oscillator is more complex than for the existing low-gain amplifiers because the optical wave in the oscillator is not predetermined by an injector. For example, modeling shows that the energy extraction in the oscillator may be significantly reduced by the action of self-generated optical sidebands displaced slightly from the primary wavelength. Second, a higher level of electron and photon beam control is required to get proper physical overlap of these beams at shorter wavelengths. This has direct impact on the e-beam, wiggler, and optics technology necessary for the short-wavelength experiment. Of particular importance is the combination of electron beam emittance and current required, which are at the state-of-the-art levels for the visible experiment.

Models have been developed to describe both the transverse and longitudinal mode structure of the FEL. The transverse-mode analysis shows that the FEL can operate at high output beam quality with only modest beam control aperturing. The longitudinal-mode analysis shows the effect of the predicted, but yet unobserved, sideband instability. Simulations for a realistic visible-wavelength system show that the extraction efficiency is reduced to about half if the instability is unsuppressed. It is shown that

frequency selectivity in the optical cavity is a viable means of suppression.

Wiggler magnet design for short-wavelength operation is considered from the standpoint of maximizing gain and extraction. This includes identifying basic parameters of the wiggler as well as e-beam requirements to maximize the electron-photon interaction. A 10 μm wiggler was constructed for testing various design features. It has undergone extensive field testing, but has not operated on the electron beam line in this program.

Optical-cavity analysis shows that alignment tolerances may be a critical factor in high-power short-wavelength systems. The problem stems from the extreme alignment sensitivity of near-concentric cavities. Such cavities provide the necessary small spot size at the wiggler and large spot size at the end mirrors. It is proposed here that this problem can be solved by the use of a novel ring resonator concept. Analysis shows that this ring is compatible with glancing-incidence optics (for cavity length reduction) and that at the parameters of interest this ring has an order of magnitude improved alignment tolerance over the linear near-concentric cavity.

Also included in this report are details of the 4.2 percent electron energy extraction obtained in the joint Mathematical Sciences Northwest/Boeing Aerospace Company experimental effort. This measurement is made in an amplifier configuration at 10.6 μm using a CO_2 laser probe beam and 20 MeV electron beam from the Boeing Linac. This extraction is the highest achieved to date in a Compton-regime FEL.

Section 1

OVERVIEW

Recent demonstrations of high-efficiency tapered-wiggler FEL amplifiers have improved the near-term prospects for obtaining a high power, high efficiency, visible laser. Efficiencies of 3.5 and 4.2 percent for conversion of electron kinetic energy to 10.6 micron radiation have been achieved at LANL[1-1] and MSNW/Boeing[1-2], respectively. These values are in a range that could lead to system efficiencies of ~ 20 percent if electron energy recovery is incorporated. By contrast, the original Stanford[1-3] and recent LANL[1-4] infrared oscillators, both operating with non-tapered wigglers, achieved only 0.2 percent extraction. The larger extraction afforded by the tapered wiggler results from variation of wiggler parameters, magnetic wavelength or field amplitude along the length, so that a resonant interaction is maintained as electrons decelerate. Achieving high deceleration requires high photon field strength and, *therefore high photon power, so as a consequence* the gain is low when the extraction is high. This limits the ability to achieve oscillation at high extraction, and thus far oscillation with tapered wigglers has not been achieved at extractions exceeding 1 percent.[1-5]

There are clearly defined technology hurdles between the existing infrared oscillator and amplifier results and a high power visible system. Outstanding issues are the higher electron beam brightness needed, and optical cavity configurations compatible with high power and the smaller beam size. If the e-beam brightness is defined as I/ϵ_n^2, where I is the peak current and ϵ_n is the normalized emittance, a brightness increase of about two orders of magnitude is needed to go from 10 micron to 1/2 micron experiments with equivalent gain and extraction. High brightness sources are already available; an example is Stanford's superconducting accelerator,[1-6] but it provides roughly a factor of 20 too low current for the applications of interest. Concerning optics, it is apparent that the small beam size of the FEL is not well matched to the large mirrors

required for high power systems. Existing proposals for high power FEL cavities typically result in awkward overall lengths and high sensitivity to mirror alignment. In addition to these technology issues, there are also basic physical phenomena which threaten the tapered wiggler concept. In particular, an instability has been predicted, but not yet observed, which may lead to loss of extraction by growth of an optical sideband displaced roughly 1 percent from the nominal operating frequency.

This final report addresses key issues of the basic technologies and physics needed to make the transition to high power visible systems. The MSNW work reported here is part of a cooperative effort with Boeing Aerospace Company. The tapered-wiggler measurements included were made at the Boeing Radiation Effects Laboratory. The scope of the MSNW work includes the following areas as they relate to short wavelength systems.

1. Wiggler technology, especially concerning emittance acceptance and oscillator start-up.

2. FEL theory relevant to cavity modal properties and sideband instabilities.

3. Concentric optical cavities; applicable to near-term low power experiments.

4. Angularly stable ring cavities; applicable to high power systems.

Also included in this report are details of the 4.2 percent extraction achieved in January 1983. The measured electron energy spectra, with and without the FEL interaction, are shown in Figure 1-1. This is the highest extraction achieved to date in a Compton regime FEL. This result, along with associated parametric measurements, confirms the validity of the straightforward models used to characterize the tapered-wiggler FEL.

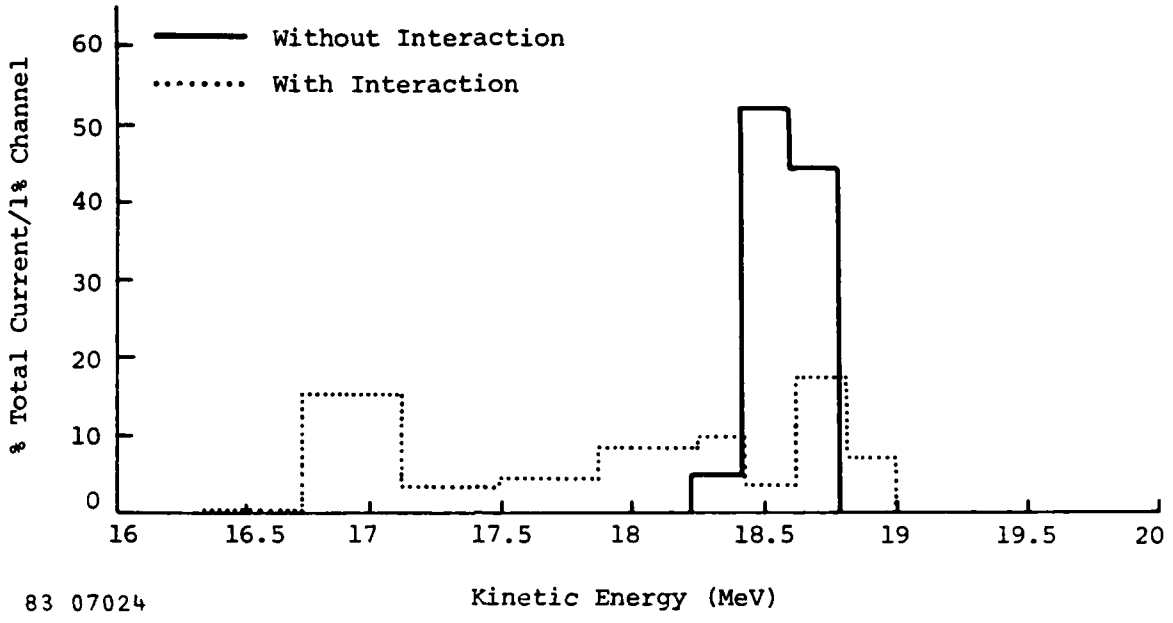

Figure 1-1. Electron Energy Spectra Showing 4.2 Percent Extraction with Tapered-Wiggler FEL.

Listed below is a brief summary of the status of each of the numbered topics above. Details are provided in Sections 3 through 6. The extraction measurements are described in Section 2.

1.1 WIGGLER TECHNOLOGY

The wiggler work is focused on the development of a preliminary wiggler design for visible wavelength oscillators with emphasis on maximum gain, maximum emittance acceptance, and prompt oscillation start-up. In addition to the design work, a new wiggler has been constructed for use in start-up studies at 10 microns using the existing facility. The primary feature distinguishing this wiggler from the original MSNW wiggler is an adjustable taper. Proper taper choice is expected to overcome the unacceptably low small-signal gain of long, tapered wigglers. A portion of the assembled wiggler is shown in Figure 1-2. The wiggler is divided along its length into nine sections, and the taper adjustment is achieved by control of the gap in each section.

An emittance acceptance analysis is used to define e-beam requirements and is used in wiggler optimization for a visible oscillator. Designs have been optimized from the standpoint of both gain and emittance acceptance. One finding is that two-plane focusing dramatically enhances emittance acceptance at short wavelengths. A simple angular canting scheme for generating two-plane focus in planar wigglers has been analyzed, and a successful demonstration of the concept was made by reconfiguring the original MSNW wiggler with canted magnets. The new adjustable-taper wiggler is discussed in Section 3 and the emittance acceptance optimization is in Section 4.

1.2 FEL THEORY

The purpose of the theoretical work is to predict FEL performance as well as to provide a framework in which performance improvement schemes can be assessed. Key items examined are the transverse modal properties in low

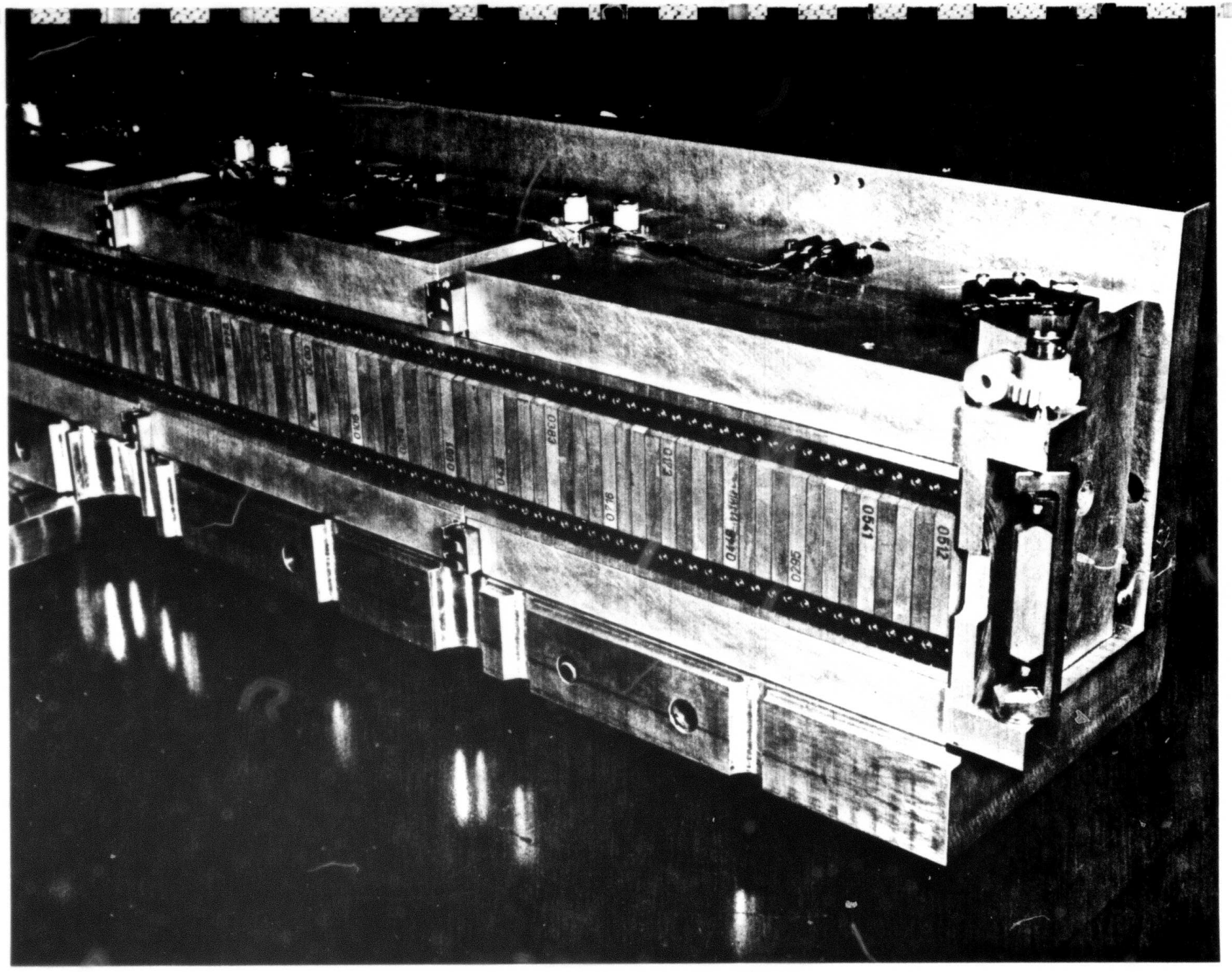

Figure 1-2. Segmented Variable-Taper Wiggler.

gain resonators, and the sideband instability. The low Fresnel number of the FEL optical system requires use of physical optics codes (i.e., including diffraction), and both two- and three-dimensional versions have been developed (this work partly supported by AFOSR). Properties peculiar to the FEL have been identified including a forward-reverse pass asymmetry caused by the one-way gain media, and diffractive steering caused by the narrow bore wiggler. In some cases, this steering dramatically affects the cavity mirror alignment tolerance. Also seen in the simulations is an intracavity beam of nearly diffraction limited quality, which is virtually guaranteed by the low Fresnel number geometry.

The sideband instability analysis is important in that this instability is one of the few fundamental physics issues proposed to date that could threaten the high extraction oscillator concept (another is e-beam instabilities in the accelerator waveguide). The problem has been studied in this contract (also partially supported by AFOSR) for the first time in the parameter space applicable to the visible FEL. Growth of the sidebands is observed and they reduce the extraction efficiency by about one-half. The same simulation shows that the instability can be suppressed by use of frequency selective elements in the optical cavity. An example of extraction as a function of time from e-beam turn-on is shown in Figure 1-3. Comparison of the curves for cases with and without optical filtering shows the beneficial effect of filtering.

The transverse mode analysis and sideband instability are fully discussed in Section 5.

1.3 CONCENTRIC CAVITIES

The near-concentric optical cavity is explored as one means of providing the necessary small spot size at the wiggler with large spots at the end mirrors. The length and alignment tolerances for FEL applications are identified, including the effect of diffractive steering.

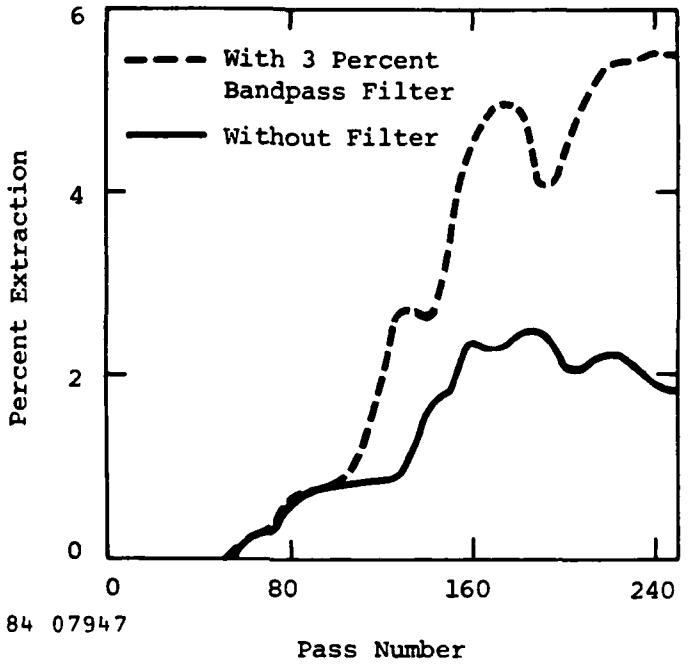

Figure 1-3. Sideband Instability Simulation Shows Frequency Filtering Suppresses Instability and Restores Full Extraction.

A preliminary design suitable for high extraction, low duty factor experiments is described. A 60 meter cavity length provides a mirror loading just below the dielectric coating damage threshold for an optical mode matched to the preliminary wiggler design. Such a cavity can handle circulating powers of several hundred kilowatts averaged over the electron macropulse. If the system is operated at the lowest possible duty factor, namely only one optical pulse in the cavity, the peak power of approximately 6 Gigawatts is sufficient to demonstrate 5 percent extraction.

1.4 RING CAVITY

The concentric cavity is not well suited to high power systems, and for such systems we propose use of a novel ring resonator.[1-7] The difficulty with the high power concentric cavity is that its alignment tolerance falls as $1/r^2$ where r is end mirror radius, and at power levels of eventual interest sufficiently large mirrors are required that alignment becomes a risk issue. This alignment issue can be nearly eliminated by employing a novel resonator design based on an angularly stable semi-confocal ring. When coupled with glancing incidence beam expanders, the ring is well suited to high power systems. The basic geometry is shown in Figure 1-4. The glancing incidence elements are not necessary to the concept but can reduce the cavity length by roughly an order of magnitude. In the cases studied, the ring cavity relaxed the alignment tolerance over an equivalent concentric cavity by an order of magnitude. There are other advantages of the ring as compared to its equivalent concentric cavity. For example, the heat load and figure requirements of the glancing incidence elements are reduced, and diffractive losses at the wiggler are suffered only once per round trip instead of twice. Details are provided in Section 6.

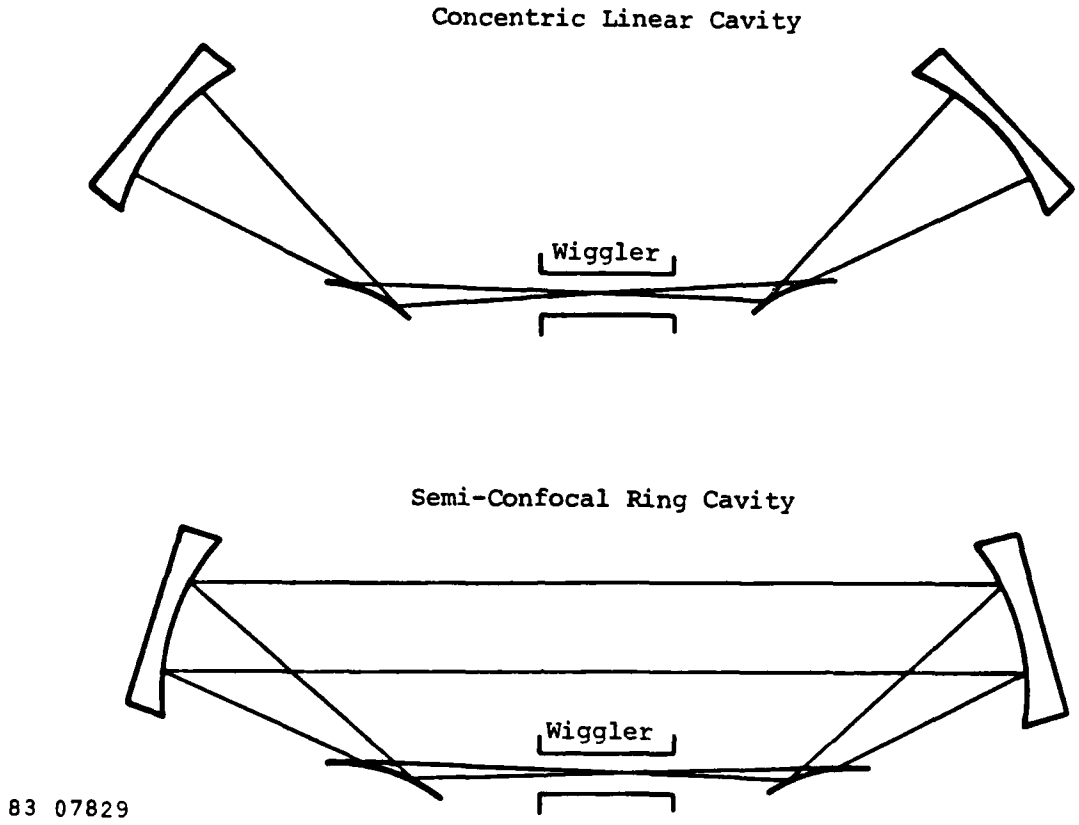

Figure 1-4. Comparison of Ring and Concentric Cavity Geometries. The ring geometry has far less sensitivity to angular mirror misalignment.

REFERENCES

1-1. R.W. Warren, B.E. Newnam, J.G Winston, W.E. Stein, L.M. Young, and C.A. Brau, "Results of the Los Alamos Free Electron Laser Experiment," IEEE J. Quant. Elect. QE-19, 391 (1983).

1-2. W.M. Grossman, J.M. Slater, D.C. Quimby, T.L. Churchill, J. Adamski, R.C. Kennedy, and D.R. Shoffstall, "Demonstration of Large Electron Energy Extraction by a Tapered-Wiggler Free-Electron Laser," Appl. Phys. Lett., 43, 745 (1983).

1-3. D.A.G. Deacon, L.R. Elias, J.M.J. Madey, G.J. Ramian, N.A. Schwettman, and T.I. Smith, "First Operation of a Free-Electron Laser," Phys. Rev. Lett. 38, 892 (1977).

1-4. R.W. Warren, presented at BMD/DARPA FEL Kick-Off Meeting, Los Alamos, January 1984.

1-5. J. Edighoffer, presented at BMD/DARPA FEL Kick-Off Meeting, Los Alamos, January 1984.

1-6. T.I. Smith, "The Stanford Superconducting Linear Accelerator," Phys. Quant. Elect., Vol. 8, 77 (1982).

1-7. J.M. Eggleston, "Angularly Stable Ring Resonators for High Power FELs," in Proceedings of the International Conference on Lasers '83, December 1983.

Section 2

SINGLE PASS MEASUREMENTS

Measurements of electron energy extraction in a 10.6 μm tapered-wiggler amplifier configuration are described and results are compared with theoretically predicted performance. These measurements help validate the high efficiency tapered-wiggler concept and confirm the accuracy of models used to predict oscillator performance. Additional single pass measurements presented in this section include demonstration of a planar wiggler concept for providing two-plane e-beam focusing, as required for adequate emittance acceptance at visible wavelengths, and development of a 10.6 μm small-signal gain diagnostic.

Measurements of electron beam energy extraction at power levels sufficient to demonstrate trapping and deceleration are presented in Section 2.1. The net extraction of 4 percent matches theoretical predictions for this device. Agreement is also found between predicted and observed energy spectra. Extraction was measured as a function of electron beam energy and CO_2 laser beam power, and the results are consistent with predictions of performance at the theoretical limitations. These parametric measurements are presented in Section 2.2. Experimental verification of the two-plane e-beam focusing properties of a planar wiggler with canted pole faces is presented in Section 2.3. Considerations for a small-signal gain measurement at 10 μm are presented in Section 2.4.

2.1 EXTRACTION

Electron-beam energy spectral measurements were made on a tapered-wiggler FEL amplifier. The energy extracted from the electron beam as it passes through the wiggler is an indicator of the trapping properties of the wiggler. Such measurements were made on a 19 MeV electron beam from a traveling-wave linear accelerator which interacted in a tapered-wiggler

with an intense 10.6 μm CO_2 laser beam. The electron spectra show a 4 percent net energy decrease and a 9 percent peak decrease.

These experimental results help validate the concept of the tapered-wiggler FEL as a high-efficiency source of coherent radiation. The first FEL, demonstrated at Stanford,[2-1] had an untapered wiggler. The tapered wiggler[2-2] differs from the Stanford wiggler in that the resonant electron energy of the wiggler magnet varies along its length to maintain a resonant electron-photon interaction as the electrons decelerate. The wiggler can be tapered by varying the wavelength or amplitude of the periodic magnetic field as a function of axial position, providing increased electron-beam energy extraction and increased overall efficiency at the expense of reduced gain.

Not all of the electrons entering the wiggler are trapped in the ponderomotive potential. The nominal trapping fraction for the measurement is about 50 percent, and the net deceleration is about half the peak deceleration. The corresponding energy spectrum has two peaks of roughly equal current, one near the entrance energy and the other at the energy resonant with the wiggler exit. The wiggler used in this experiment has a 9 percent energy taper and a nominal net electron energy extraction of about 4 percent.

Electron beam energy extraction is measured in the FEL amplifier using the configuration shown in Figure 2-1. The wiggler is 2.3 m long, has 100 periods, and is constructed of $SmCo_5$ permanent magnets. It has a 9 percent resonant energy taper at constant synchronous phase, achieved by decreasing the period 13 percent and the peak field strength 8 percent along the length of the wiggler, with fixed gap. In the experiments reported here, the CO_2 laser generates a 40 ns optical pulse, and the linear accelerator typically generates a 0.5 μsec electron beam macropulse consisting of 20 psec micropulses generated at 2.8 GHz. The two beams are timed so that the optical pulse falls upon the longer electron-beam macropulse in the wiggler. During overlap, all of the electron micropulses

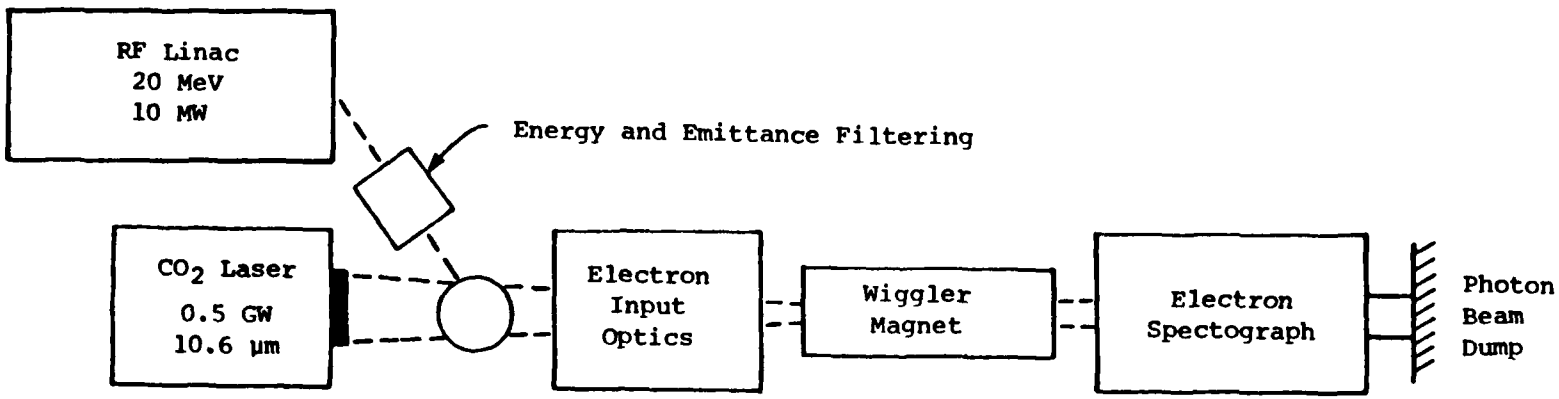

Figure 2-1. Block Diagram of Amplifier Experiment.

are subject to the FEL interaction. The spectrograph follows the envelope of the temporal evolution of the electron-beam energy spectra on a nanosecond timescale, but cannot resolve individual micropulses. The RF linac, electron-beam spectrograph, wiggler magnet, and CO_2 laser used in the extraction experiments are discussed in detail in Reference 2-3.

The Boeing linac is an S-band traveling-wave radio-frequency linear accelerator. Since our last reported results,[2-3] the gun was modified by the addition of a cowling intended to intercept electrons from the perimeter of the cathode and reduce the linac's emittance. Peak micropulse currents are from 2 to 5 amps leaving the accelerator structure, and are lower at the wiggler due to losses in filtering and other losses in transport. The full width energy spread is 2 percent, and the normalized emittance for 100 percent of the charge at the wiggler, defined as $\gamma\pi xx'$, is about 0.01 cm-rad in each plane. The beam is spatially filtered to achieve this emittance and energy spread, and the peak micropulse currents are typically 50 to 200 mA at the wiggler. Since earlier experiments, the emittance filtering slits in the accelerator beamline have been upgraded, and an emittance-measuring wire-scanner has been added just upstream of the wiggler. The emittance filter consists of four independently movable jaws, and is located where no encoding of energy on position should exist. The new jaws are typically used with gaps three times smaller than the previous fixed aperture filter. An emittance-measuring wire-scanning profilometer was located directly upstream of the wiggler and consists of a wire-shadow scanner, a turn-out magnet, and a stopping block. Emittance is deduced by measuring beam size as a function of the strength of an upstream quadrupole magnet.[2-4,2-5] These measurements give the minimum spot size and divergence angle of the beam, allowing the emittance to be computed.

The electron spectrograph has a focal plane with segmented stopping blocks cabled to oscilloscope-channels. The spectrograph has a bandwidth of approximately 200 MHz, and, as used, a minimum of 1 percent energy spread per oscilloscope channel. The use of discrete stopping blocks limits the spectrograph in energy resolution, but has the advantage of

allowing temporal resolution and relatively simple calibration. The CO_2 laser consists of an oscillator-preamplifier-amplifier chain, delivering a fast rising 40 ns pulse. The peak optical power delivered into the wiggler was typically about 0.5 GW based on independent measurements of the pulse shape and the integrated energy.

Electron energy gain or loss resulting from the FEL interaction is measured with the electron spectrograph. In these experiments, the interaction is easily identified in the time-resolved spectra because the optical pulse has different temporal behavior than the electron macropulse. Representative histories of the current into the spectrograph channels during the CO_2 laser pulse are shown in Figure 2-2. Immediately prior to the time of laser overlap, most of the current was entering the spectrograph channel labeled -0.5 percent. It can be seen from the traces that the mean energy is varying on a timescale much longer than the laser pulse, and this variation can be ignored. During peak laser power, nearly 90 percent of the electrons in the nominal input channel are displaced to higher or lower energies. A small amount of current is accelerated to higher energy in the +1.5 percent channel, and the greater fraction is decelerated into the lower energy channels, down to -9 percent. The temporal histories of the channels differ greatly, reflecting the nonlinear nature of the electron trapping as a function of optical power.

An electron beam spectrum measured at the time of peak CO_2 intensity is shown in Figure 2-3. There is a 4 percent shift in the average electron energy assuming the current is evenly distributed within each spectrograph channel. The maximum extraction for any electron is 9 percent. Superimposed upon that data is the electron beam spectrum prior to injection of the CO_2 beam. The curves can be considered as output and input spectrum, respectively, because the macropulse current and spectral content do not change significantly on several nanosecond timescales. The photon pulse had a peak power of about 0.5 GW and the effective power could be less because imperfect optical beam quality (Strehl ratio <1) can only degrade the interaction. The electron spectra are taken with the

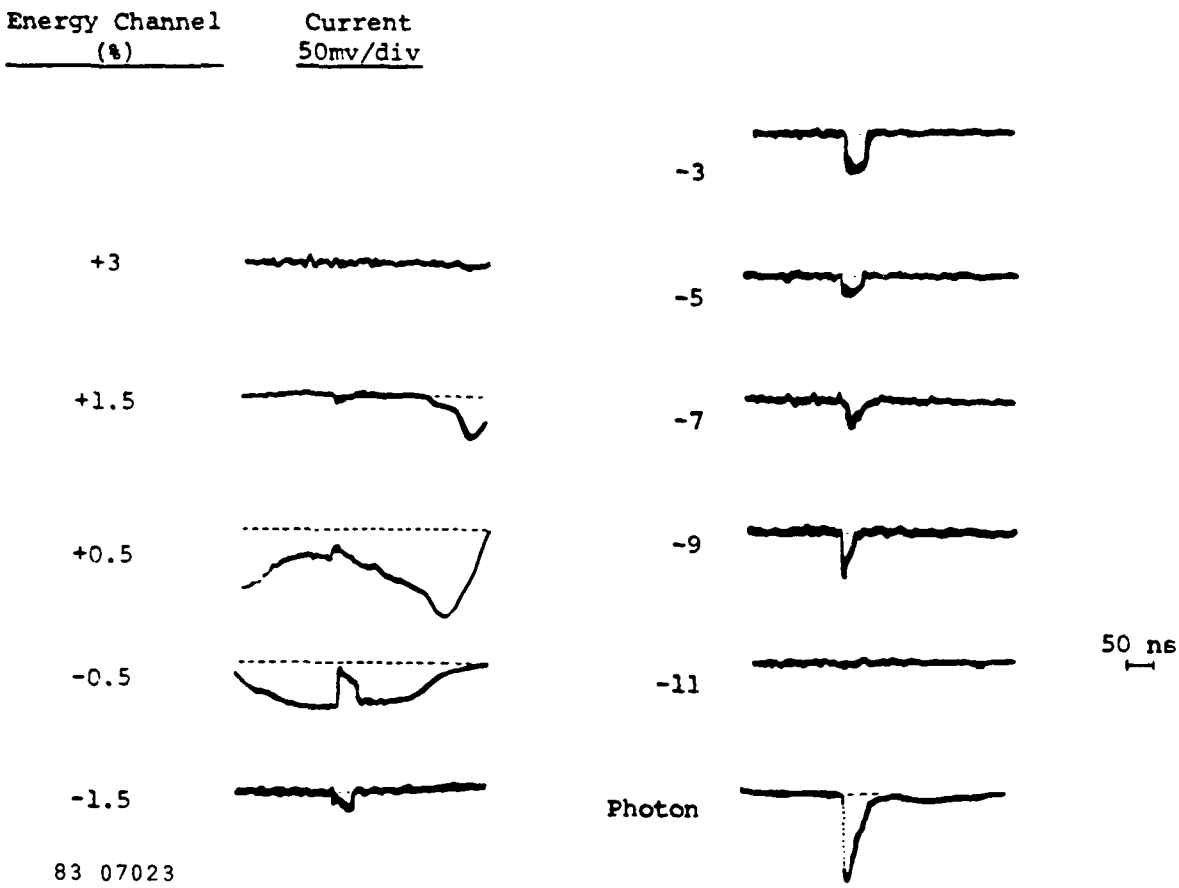

Figure 2-2. Spectrograph Histories During FEL Interaction.

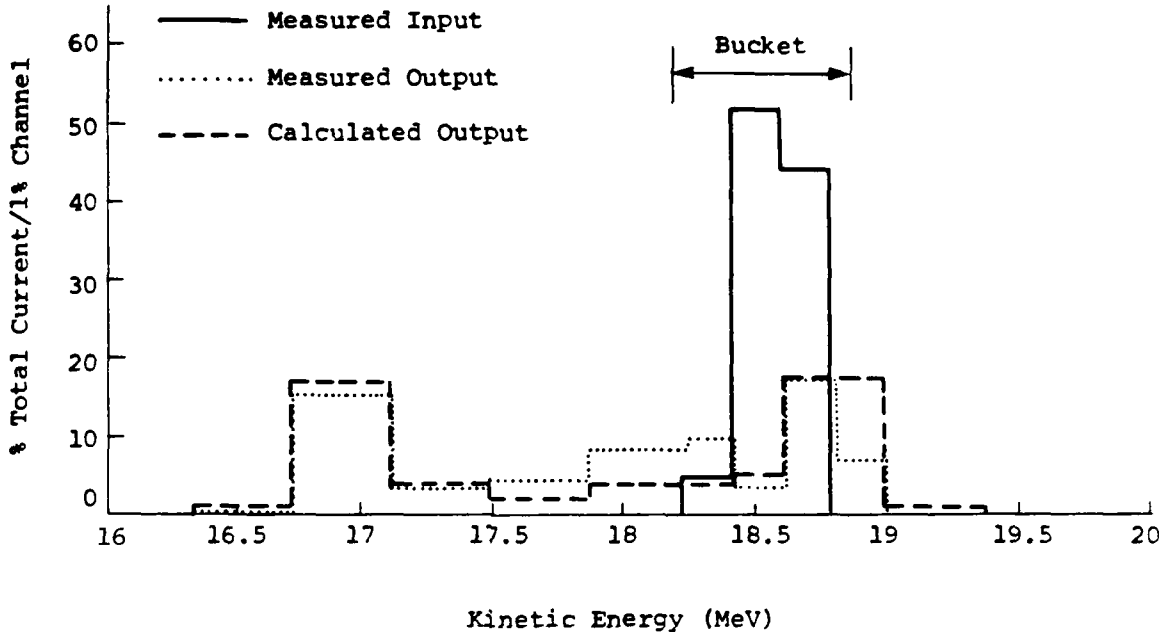

Figure 2-3. Measured Input and Output Electron Beam Spectra for FEL Interaction.

spectrograph channels connected in pairs with combined 1 percent energy acceptance over the range of 18.2 to 19.0 MeV, and 2 percent acceptance elsewhere. For any channel, the uncertainty in current at the time of maximum photon flux is less than 25 percent. An indication of the reliability of the measurements is that the sum of the measured channel currents, which should not vary, typically differ by less than 10 percent between interaction and non-interaction traces. For the data shown in Figure 2-3, the peak micropulse current at the time of the interaction is about 160 mA.

Using the input spectrum of Figure 2-3, an output electron energy spectrum, including the interaction, was calculated by direct integration of the equations for electron energy loss and electron phase in the ponderomotive potential of the FEL interaction.[2-2] In the calculation, it is assumed that the electron-beam and 500 MW optical beams are optimally focused and coaligned, and the optical beam is diffraction limited. A normalized emittance of 0.023 cm-rad at $\gamma = 37$ is assumed for both planes. The effect of emittance is included in the calculation in a two-step process. First the optical electric (E) fields and magnetic (B) fields experienced by each electron are computed as a function of axial position, including the off-axis motion but ignoring the small effect of the FEL on the trajectory. Then, the energy loss is determined in a one-dimensional integration of the energy and phase equation for electrons in the ponderomotive potential well of the FEL using the previously computed E and B fields experienced by each electron. The resulting theoretical electron spectrum, shown as the dashed line in Figure 2-3, corresponds to a net extraction of 4.0 percent and is in excellent agreement with the data. A net extraction of 4.7 percent is predicted for the same parameters, except with zero emittance. This shows that for these parameters the extraction is only weakly dependent on the emittance. The emittance used to give a theoretical curve matching the data was about twice the measured value. This choice of emittance may roughly compensate for simplifying assumptions used in the theoretical model which would otherwise lead to an overestimate of net extraction. These assumptions are that the CO_2 laser

is diffraction limited and that the electron and optical beams are optimally pointed and focused.

2.2 PARAMETRIC STUDIES

Extraction as a function of input energy has been measured over a range of input energies from 18.0 to 19.2 MeV. This data is shown in Figure 2-4. The experimental data was upshifted 1.5 percent in energy to allow for a small uncertainty in spectrograph calibration. Peak extraction is observed near 19 MeV. When the electron energy is detuned below 18.4 MeV, net acceleration of the electrons is seen. Electron deceleration and energy extraction is observed over a range of 3 percent in energy. This implies that net gain is present over an optical bandwidth of twice the energy bandwidth or about 6 percent. The data is in agreement with theoretically predicted curves generated assuming normalized emittances of 0 and .023 cm-rad, perfect focusing, perfect alignment, and a diffraction-limited optical beam. The points shown do not include all the data taken. With misalignment, poor focusing, or other problems, it is always possible to achieve results in which the magnitude of the extraction is too low, but it is not possible to achieve extraction results that are artificially high except by actual measurement errors.

Electron energy extraction has been measured as a function of laser power and is shown in Figure 2-5. Extraction is seen to increase with laser power indicating the onset of trapping, in general agreement with theoretical predictions. The data is taken from three time-resolved electron spectral records. Extraction is found as a function of time and using laser pulse histories, the extraction as a function of laser power is deduced. Again, perfect focusing and alignment are assumed for the theoretical prediction, and a 0.023 cm-rad normalized emittance is used as a rough estimate of all the effects of nonideal preparation of both beams. When the extraction is predicted as a function of laser power for zero emittance, the theoretical results parallel those shown in Figure 2-5, but the extraction is about 1 percent larger.

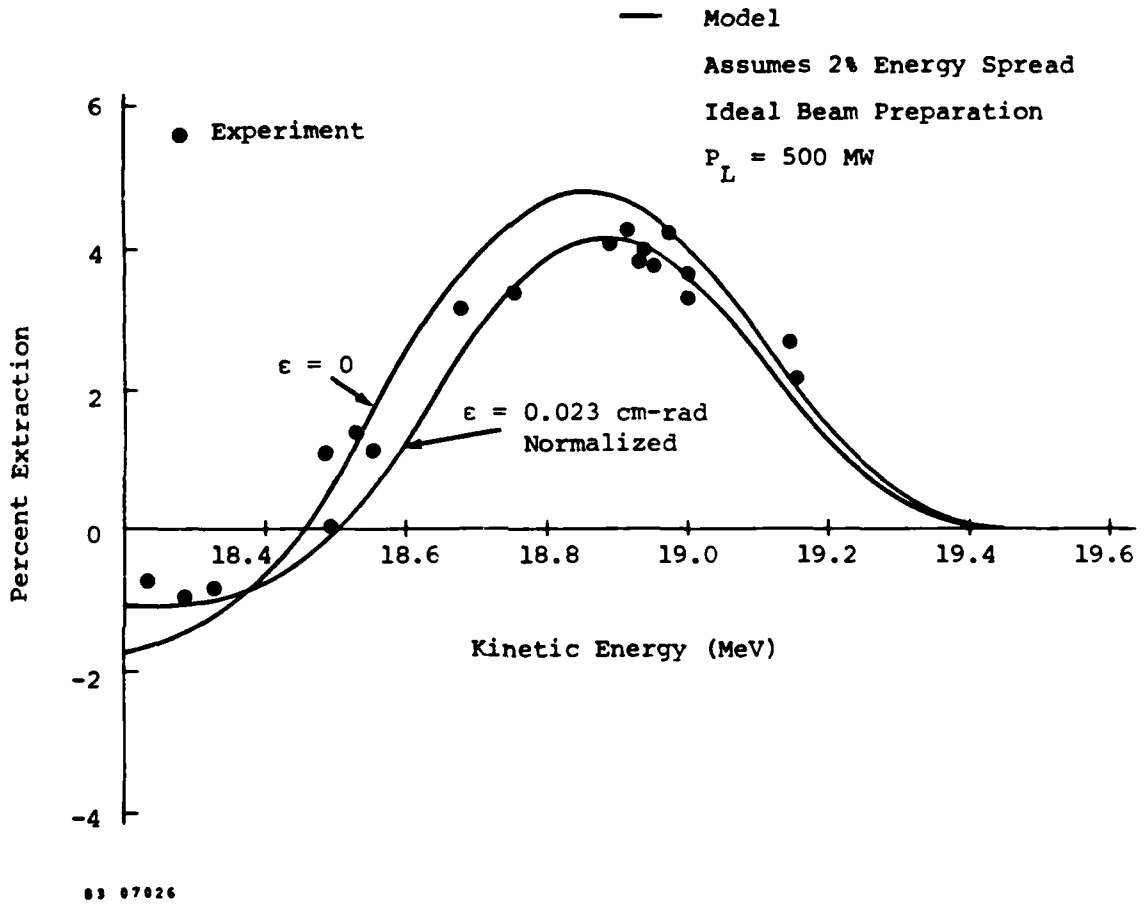

Figure 2-4. Extraction as a Function of Input Energy.

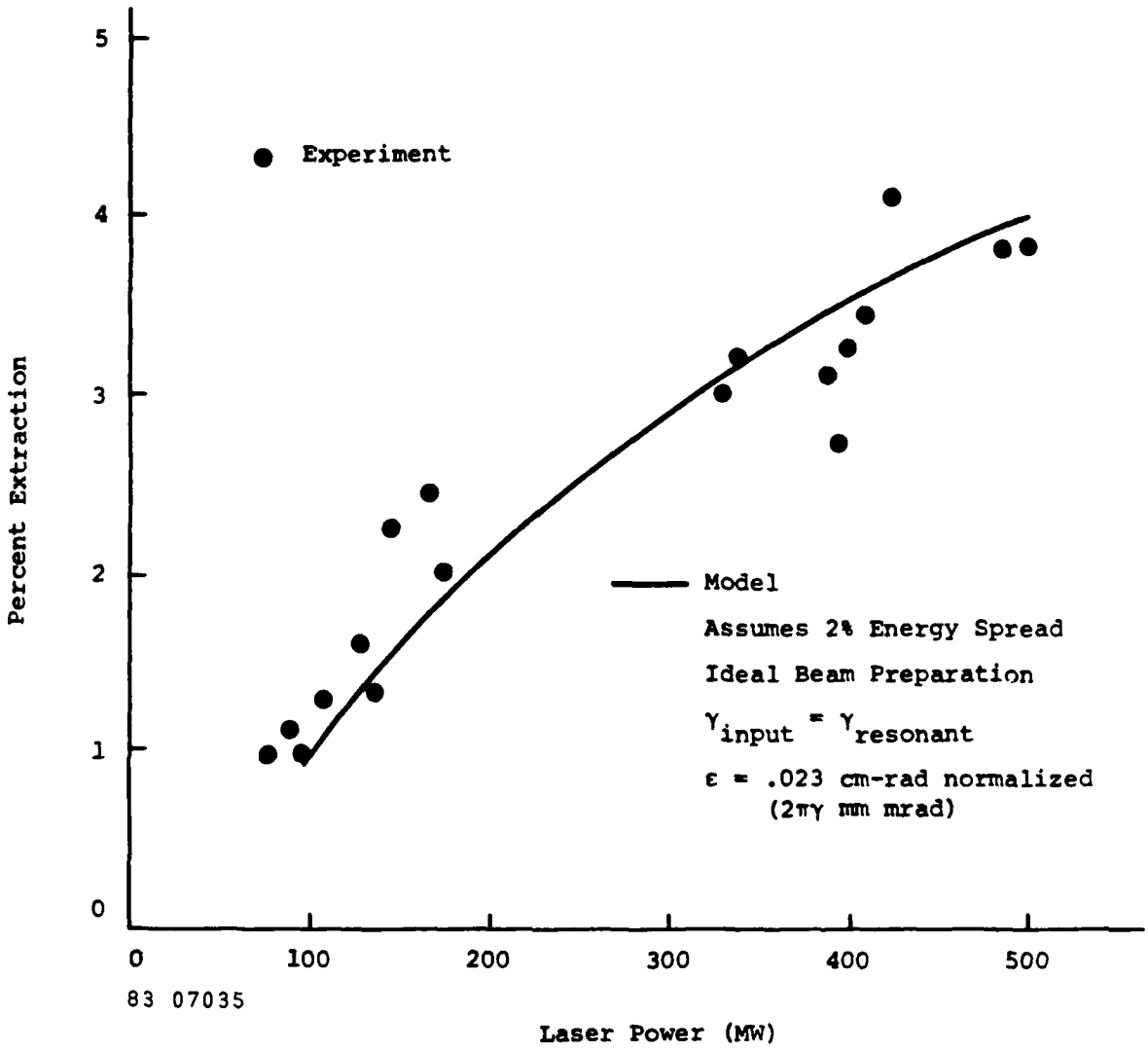

Figure 2-5. Extraction as a Function of Laser Power.

2.3 TWO-PLANE FOCUSING FOR A PLANAR WIGGLER MAGNET SYSTEM

The e-beam focusing properties of linearly polarized wigglers were investigated theoretically and verified experimentally. It was found that angular magnet canting can produce equal e-beam focusing in each of the two transverse directions. Thus the e-beam focusing characteristics of a helical wiggler can be reproduced in a planar wiggler. Planar wigglers naturally focus electrons in only one transverse direction. The required angular canting of the magnets is modest (less than about 5 degrees) and is in a plane which allows closest packing of the magnets and no degradation of the magnetic field on-axis. As described in Section 4.2.2, two-plane focusing substantially enhances the emittance acceptance of longer wigglers, particularly at short photon wavelengths. Recent magnet canting experiments using the 10 μm linearly-tapered wiggler have shown two-plane focusing and betatron wavelengths matching predictions.

2.3.1 Magnet Geometry

The magnet geometry and nomenclature are shown in Figure 2-6. The wiggler consists of a series of bar magnets with magnetization periodically oriented as indicated by the arrows on the end of the bars. The magnet wavelength, λ, is assumed to be constant and the bars are assumed to be closely packed (i.e., $\epsilon = \lambda/4$). Magnets with vertical magnetization are referred to as primary magnets; those with horizontal magnetization are called secondary magnets.

2.3.2 Focusing in the y-Direction

It is often desirable for wigglers to have focusing properties to improve e-beam emittance acceptance. Planar wigglers are focusing in the y-direction and neutrally stable in the x-direction. This can be shown by considering the Lorentz equation for a relativistic electron

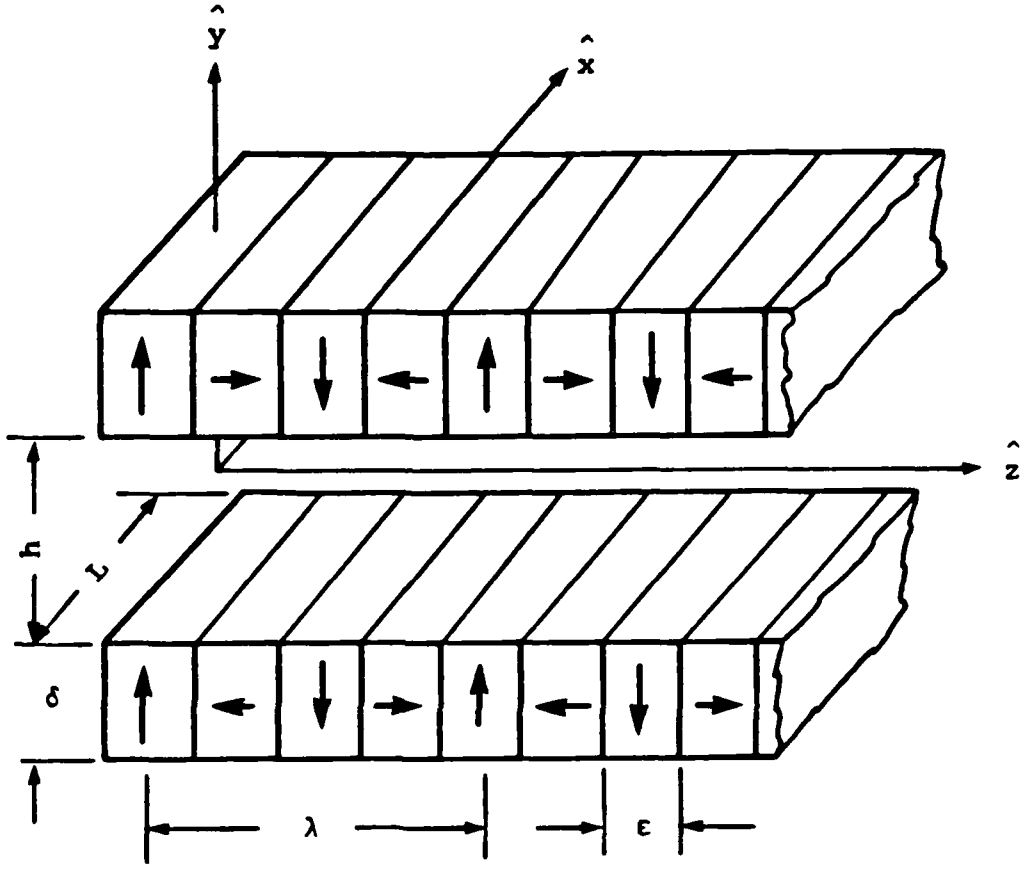

Figure 2-6. Schematic of Permanent Wiggler Magnet Configuration.

$$F = \frac{d}{dt}\left[\gamma m_o v\right] = \frac{q}{c}(v \times B) \qquad [2\text{-}1]$$

in a magnetic field produced by an idealized (infinite length in x and z directions, constant wavelength) wiggler.

$$B_x = 0 \qquad [2\text{-}2]$$

$$B_y = B_o \cosh ky \cos kz$$

$$B_z = -B_o \sinh ky \sin kz$$

The trajectory of an electron in the x-direction can be found by directly integrating Equation [2-1], provided that the electron is nearly centered in the wiggler (y≈0).

$$x(z) = \frac{-2^{1/2} a_w}{\gamma k}(\cos kz - 1) + \frac{v_o z}{c} + x_o \,, \qquad [2\text{-}3]$$

where $a_w = eB_o/2^{1/2} m_o c^2 k$. This trajectory is simply the basic "wiggle" induced by the magnet superimposed upon the ballistic trajectory determined by the initial displacement, x_o, and transverse velocity, v_o.

Using the wiggle velocity given by Equation [2-3], the equation of motion in the y-direction is

$$\frac{d^2y}{dz^2} = \frac{-2a_w^2 k}{\gamma^2} \sinh ky \sin^2 kz. \qquad [2\text{-}4]$$

Since, near the axis, sinhky ≈ky and $\sin^2 kz$ is always postive, this acceleration term has the form of a harmonic oscillator equation

$$\frac{d^2y}{dz^2} = -k_\beta^2 y. \qquad [2\text{-}5]$$

Taking the average value of the $\sin^2 kz$ function to be 1/2, the wave number of the oscillation is

$$k_\beta = \frac{a_w k}{\gamma} \quad . \qquad [2\text{-}6]$$

The oscillation results in focusing of the electron should it diverge vertically off-axis. The wavelength of the oscillation, called the betatron wavelength, is $\lambda_\beta = 2\pi/k_\beta$.

2.3.3 Focusing in the x-Direction

If a transverse gradient in the vertical field of the form

$$B_x = -B_o\, ay \qquad [2\text{-}7]$$

$$B_y = B_o\, (\text{coshky coskz} - ax)$$

$$B_z = -B_o\, \text{sinhky sinkz}$$

is somehow introduced in the wiggler, a similar betatron oscillation term is introduced in the equation of motion in the x-direction.

$$\frac{d^2x}{dz^2} = \frac{2^{1/2} a_w k}{\gamma} (\text{coskz} - ax) \qquad [2\text{-}8]$$

If the gradient is arranged so that the coefficient "a" is positive, a focusing term has been introduced. The wave number of the betatron oscillations will be

$$k_{\beta x} = \left[\frac{2^{1/2} a_w k a}{\gamma}\right]^{1/2} = \left[2^{1/2}\, k_\beta a\right]^{1/2} \qquad [2\text{-}9]$$

For motion in the y-direction, the wave number of the betatron oscillation now is modified to be

$$k_{\beta y} = \left[k_\beta{}^2 - 2^{1/2}\, k_\beta a\right]^{1/2} \qquad [2\text{-}10]$$

Evidently, the addition of focusing power in the x-direction removes it from the y-direction. The sum of the squares of the betatron wave numbers

in the x and y directions is constant.

$$k_{\beta y}^2 + k_{\beta x}^2 = k_\beta^2 \qquad [2\text{-}11]$$

By suitable choice of the field gradient parameter a, the focusing power in the x and y planes can be made equal.

2.3.4 Magnet Canting

Two-plane focusing can be provided in a planar wiggler either by addition of external quadrupoles or by angular rotation of the wiggler magnets. The former method allows a readily adjustable focal strength but requires precise alignment to insure that the wiggler and focusing elements are coaxial, thus avoiding addition of extraneous steering. The latter method ensures that the focusing properties are properly aligned and, in principle, could be used with hybrid ($SmCo_5$ plus steel) wigglers which do not allow linear superposition of external fields. A planar wiggler configuration with two-plane focusing provided by angular rotation of the secondary magnets was originally suggested by Neil.[2-6] Another way to produce a transverse gradient in B_y is by positioning the primary magnets with a slanting angle relative to the x axis as shown in Figure 2-7. This configuration differs from the design of Neil in that only those magnets with polarization perpendicular to the beamline are canted, and the canting is in a plane which allows closest packing of the magnets with no degradation of the on-axis magnetic field strength. Successive primary magnets are canted alternately with positive and negative angles. Primary magnets with downward directed magnetization are indicated by the dashed lines in Figure 2-7.

A computer program has been written to evaluate the magnetic fields produced in a wiggler with canted magnets. The magnetic field is calculated in three dimensions by superposition of the fields from individual magnets. This is allowable for $SmCo_5$ magnets since the material is linear. Fields due to canted magnet bars are calculated using suitable

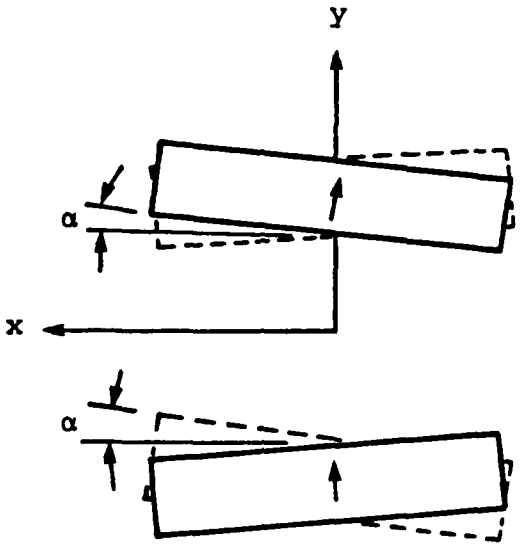

81 04985

Figure 2-7. End View of Canted Primary Magnets Showing the Cant Angle, α.

coordinate transformations. Using this calculational tool, the magnetic fields near the axis of a wiggler with canted primary magnets are found to fit the form

$$B_x = -B_o\,(ay + by\cos 2kz) \qquad [2\text{-}12]$$

$$B_y = B_o\,(\cosh ky \cos kz - ax - bx\cos 2kz)$$

$$B_z = -B_o\,(\sinh ky \sin kz - 2bkyx \sin 2kz).$$

The non-alternating transverse gradient in B_y which was needed to achieve x-plane focusing is indeed produced by this type of magnet canting. Off-axis second harmonic terms appear also. These terms introduce small additional oscillatory components to the electron trajectories but do not affect the focusing properties of the wiggler.

The dependence of the coefficient a on magnet cant angle is shown in Table 2-1 for a particular magnet geometry. The parameter a increases linearly with cant angle for small angles and then reaches a peak value at a cant angle of about 20 degrees. The on-axis magnetic field strength changes very little with increasing cant angle. Table 2-2 shows the dependence of the coefficient a on magnet gap for a fixed cant angle of 10 degrees. The product aB_o, where B_o is the peak field on-axis, is fairly constant with magnet gap size up to about $h/\lambda = 0.75$, where aB_o begins to drop dramatically.

An example wiggler design for a 10 μm FEL is described in Table 2-3. The magnet wavelength is 2.2 cm with a gap between magnets of 0.5λ. With $SmCo_5$ magnets, the peak field on-axis is 3.04 kG. For 20 MeV electrons, the betatron wavelength for focusing in the y-direction is about 2 m. When the magnets are canted about 5 degrees, the focusing in the x and y directions becomes nearly equal, with a betatron wavelength of 2.8 m. If the magnets are further canted to an angle of 10 degrees, the focusing in the y-direction vanishes and the betatron wavelength for focusing in the x-direction becomes about 2 m. Cant angles up to 25 degrees are allowable in this configuration before the magnets touch.

Table 2-1

Maximum Field On-Axis and Transverse Field Gradient as a Function of Primary Magnet Cant Angle for $h/\lambda = 0.5$, $L/\lambda = 2.5$, $\delta/\lambda = 3/8$, and $\epsilon/\lambda = 1/4$ Near the Center of a 10 Wavelength Wiggler Containing Primary and Secondary Magnets

α	B_o/B_r	$a\lambda(B_o/B_r)$
0°	0.338	0.0000
5°	0.340	0.00916
10°	0.345	0.01712
15°	0.353	0.0230
20°	0.364	0.0259
25°	0.375	0.0255

Table 2-2

Maximum Field On-Axis and Transverse Field Gradient as a Function of Magnet Gap for $\alpha = 10°$, $L/\lambda = 2.5$, $\delta/\lambda = 3/8$, and $\epsilon/\lambda = 1/4$ Near the Center of a 10 Wavelength Wiggler Containing Both Primary and Secondary Magnets

h/λ	B_o/B_r	$a\lambda(B_o/B_r)$
0.25	0.738	0.01436
0.5	0.345	0.01712
0.75	0.1601	0.01797
1.0	0.0743	0.00744

Table 2-3

PARAMETERS OF AN EXAMPLE 10μm WIGGLER DESIGN

Magnet Bar Dimensions		
Height	δ	0.825 cm
Width	ϵ	0.55 cm
Length	L	5 cm
Remnant Field	B_r	9000 G
Wiggler Parameters		
Length	L_w	2.3 m
Wavelength	λ	2.2 cm
Gap	h	1.11 cm
B_y On-Axis	B_o	3040 G
Wavenumber	k	2.86 cm^{-1}
E-Beam Parameters		
Electron Energy	E	20 MeV
Gamma	γ	40
Wiggler Focusing Properties		
Basic Betatron Wavelength	λ_β	199 cm
Betatron Wavelengths for 5° Cant	$\lambda_{\beta x}$ $\lambda_{\beta y}$	270 cm 296 cm
Betatron Wavelengths for 10° Cant	$\lambda_{\beta x}$ $\lambda_{\beta y}$	199 cm ∞

The cant angle which provides equal two-plane focusing is a function of the magnet bar length and other geometrical factors.

2.3.5 Experimental Verification

Provision of two-plane focusing by angular canting has been experimentally investigated using the first wiggler built by MSNW. An end view diagram of this wiggler is shown in Figure 2-8. All magnets are external to the vacuum chamber and each is mounted to a separate aluminum magnet holder. The wiggler taper is provided by varying the wiggler period, determined by the spacing of grooves cut in the positioning bars. A unique feature of this wiggler is the provision for angular canting of each magnet in the plane of the figure.

Following rotation of the primary magnets, equal two-plane focusing was observed at the theoretically predicted angular rotation, 2.7 degrees for this geometry. Figure 2-9 gives results from this experimental verification of distributed two-plane focusing in the MSNW wiggler. Using fluorescent screens within the wiggler, betatron oscillations were observed to occur in both planes when the e-beam was steered off-axis at the wiggler entrance. The periods of oscillation in each plane were equal within the measurement accuracy. The 2.7 degree cant angle was predicted theoretically to give approximately equal focusing in each plane along the full wiggler length on the average, although the focal strength is not equal at all positions within the wiggler due to the taper.

2.4 SMALL-SIGNAL GAIN

A small-signal gain diagnostic has been developed for use with the variable-taper wiggler. No gain measurements have been made thus far, but it is intended that this diagnostic will be used to verify that nonuniform tapers can enhance FEL gain and therefore accelerate oscillator start-up. The diagnostic developed here is for a 10 μm laser, but the method also

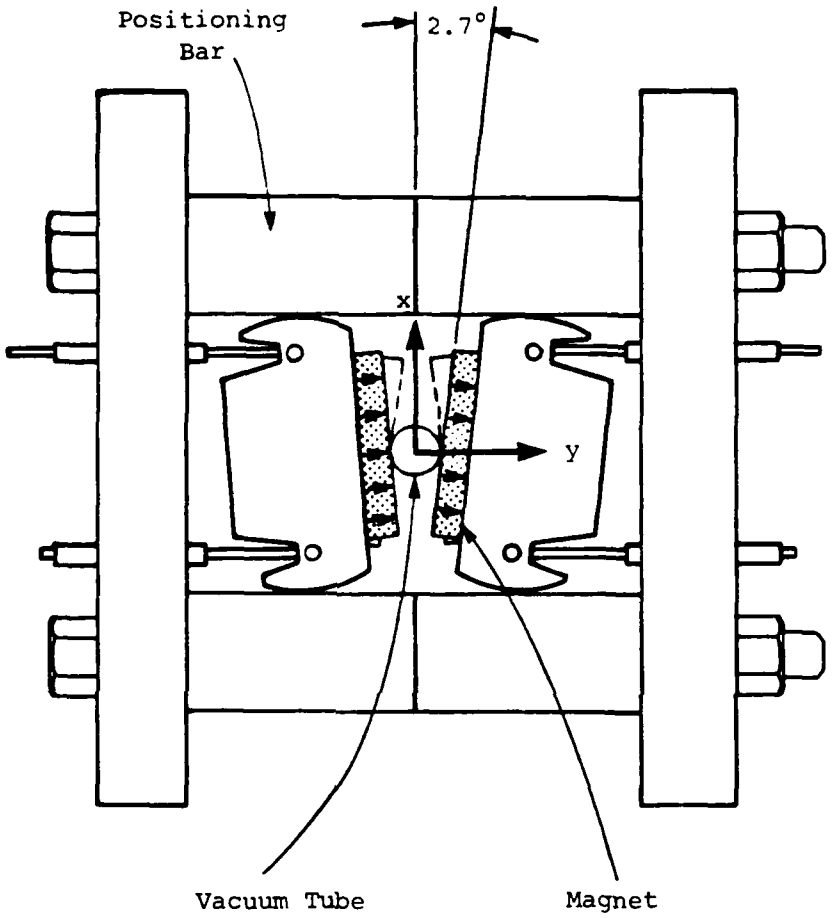

Figure 2-8. End View of First MSNW Wiggler Showing Canted Magnet Configuration

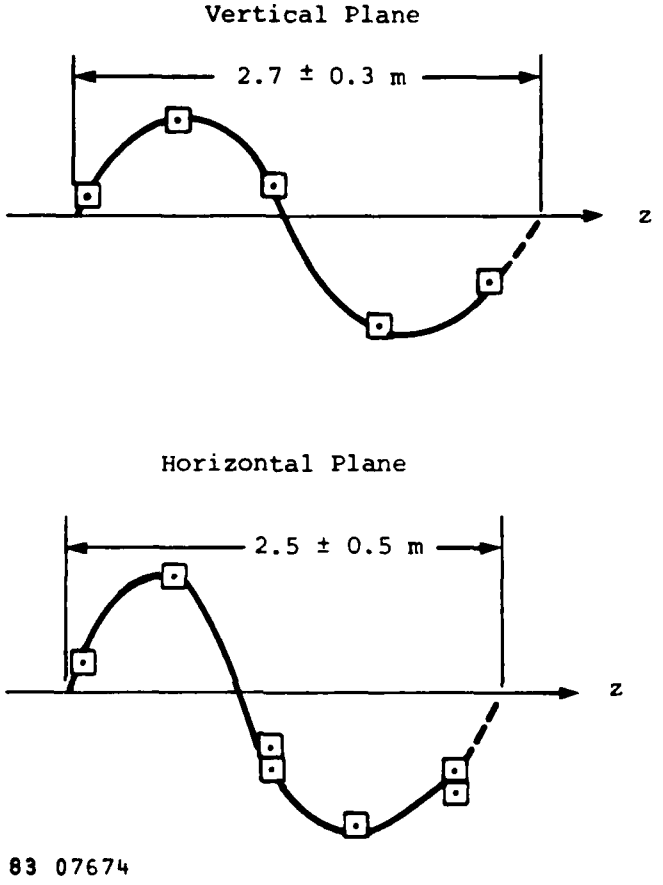

Figure 2-9. Betatron Trajectories Observed in the Canted Magnet Configuration of the MSNW Wiggler, Demonstrating Distributed Two-Plane Focusing.

applies to visible wavelengths. Gain measurements can also verify the electron beam quality and alignment required for a successful oscillator.

Small-signal gain can be measured by detecting intensity modulation of a CW optical probe beam which is subject to the FEL interaction.[2-7] A schematic diagram of the apparatus which measures this intensity modulation is shown in Figure 2-10. A square law detector detects an intensity modulated signal which has a fundamental component at the linac frequency. The power at the fundamental is a small fraction of the total power represented by the Fourier series. The intensity of this component is proportional to the strength of the FEL interaction. Calibration of the measurement requires knowledge of the electron micropulse temporal profile, which can be provided by a Cherenkov emitter and a streak camera. The optical pulse shape is assumed to follow that of the electron pulse. Also required is a measurement of the D.C. probe beam power level.

The measurement, as shown in Figure 2-10, can be accomplished with a 10.6 μm CW waveguide CO_2 laser as the probe and a HgCdTe photovoltaic detector to sense the gain induced modulation. The instantaneous electron beam current can be determined to within a proportionality factor using the emission from a thin Cherenkov emitter and a streak camera detector. The desired accuracy of the gain measurement is ± 10 percent and the desired resolution is ± 0.5 percent. The peak instantaneous gain expected is 5 to 10 percent and the resolution of gain must be below 0.5 percent to obtain the desired resolution.

The FEL amplifier will be probed with a laser whose intensity is well below gain saturation. The probe beam can be made as intense as the detector will permit in order to maximize the signal-to-noise ratio. The measurement will average the gain over a macropulse. If enhanced signal-to-noise is desired, electronic or digital averaging of the data over many macropulses can be employed.

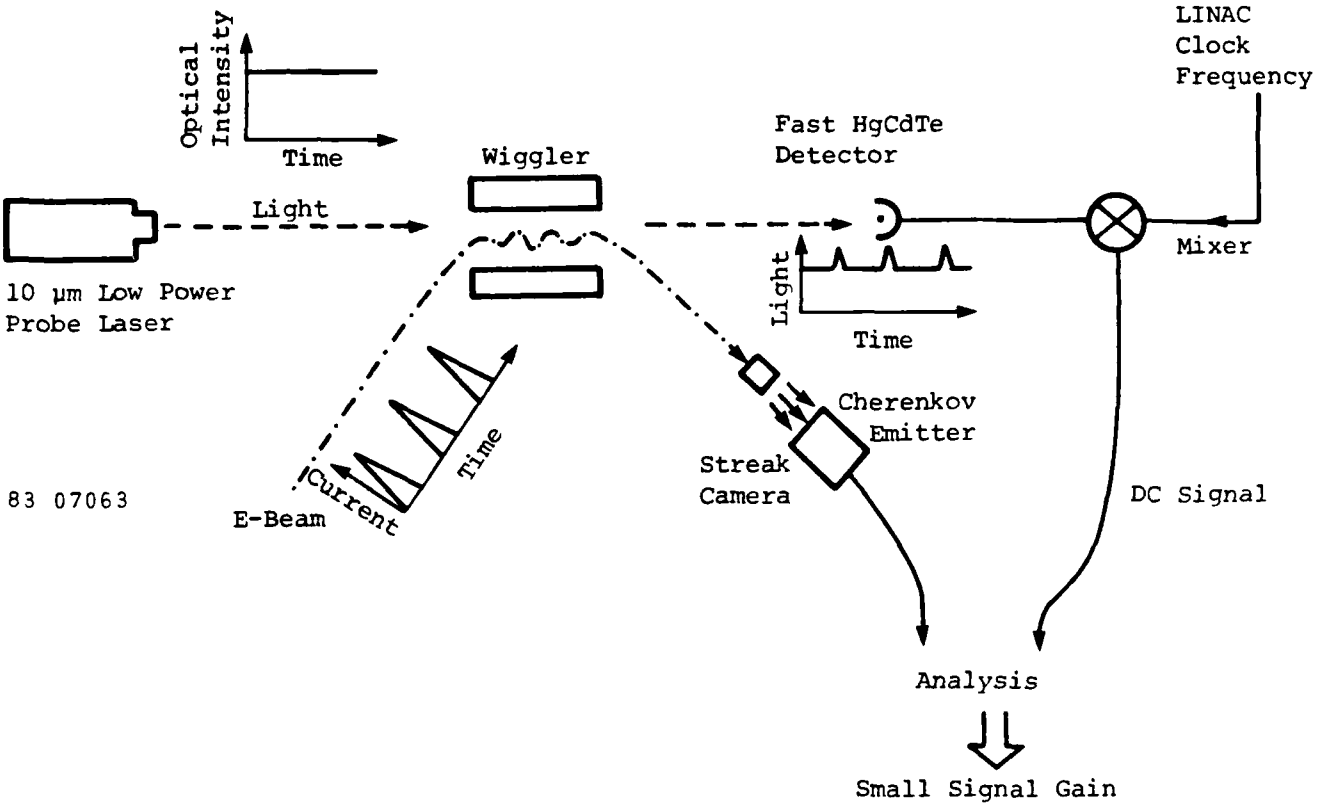

Figure 2-10. Small-Signal Gain Measurement System.

The small-signal gain is assumed to possess identical time dependence to that of the electron beam current, and the micropulse width is assumed constant during the macropulse. Consequently, the e-beam properties, such as emittance and energy, are implicitly assumed not to vary either between micropulses or throughout the duration of a single macropulse. In the small gain regime, the optical gain, G(t), is linearly proportional to the e-beam current P(t):

$$G(t) = g\ P(t)\ , \qquad [2\text{-}13]$$

where g is the proportionality constant. The proportionality constant between the e-beam current and the optical gain is determined by measuring the modulation in the intensity of a periodically amplified probe beam and normalizing this value to the intensity of the incident probe beam. The output of the HgCdTe detector at the linac frequency is measured using heterodyne mixing techniques. This reduces the effective detector bandwidth by integration over many micropulses.

One may write the intensity modulated output I(t) of the FEL amplifier as a Fourier series in harmonics of the linac frequency $1/\tau_o$. The first expansion coefficient (i.e., that at the linac frequency) is given by,

$$A_1 = \frac{2}{\tau_o} \int_{-\tau_o/2}^{\tau_o/2} G(t) I_o \cos\left[\frac{2\pi\tau}{\tau_o}\right] d\tau\ . \qquad [2\text{-}14]$$

Since the gain G(t) is simply the fractional change in signal intensity I_o,

$$I(t) = I_o(1 + G(t))\ , \qquad [2\text{-}15]$$

we see that the coefficient for the first term in a Fourier series for G(t) is A_1/I_o. Then the proportionality constant g in Equation [2-13] can be set by finding the ratio of the first term in the G(t) series to the first term in the P(t) series.

$$G(t) = \frac{A_1 P(t)}{I_o}\left[\int_{-\tau_o/2}^{\tau_o/2} P(t)\cos\left[\frac{2\pi\tau}{\tau_o}\right] d\tau\right]^{-1} . \qquad [2\text{-}16]$$

Thus, the measurement of the e-beam profile, P(t), the probe beam intensity, I_o, and the amplitude, A_1, of the Fourier component of the optical modulation of the linac frequency are sufficient for determining G(t), the gain.

Because the desired resolution in fractional gain is small (0.002) and the e-beam duty cycle is low (0.06 at 2.8 GHz), the desired minimum detectable signal power at 2.8 GHz will be a factor of 10^4 below the steady background of the probe beam. The signal is linear in the product of the gain and the duty cycle (τ_μ/τ_o). However, because of the limited detector bandwidth (the frequency roll-off begins at 150 MHz), the detector response for the first Fourier coefficient will be best for frequencies less than 150 MHz. Due to this trade-off, the present experiment is designed for a linac frequency of 20 MHz.

Analysis shows that heterodyne mixing of the detector and linac (the local oscillator) signals combined with integration of the mixer output over the macropulse (to narrow the noise bandwidth) will provide the necessary measurement sensitivity. To provide additional sensitivity, a grating spectrometer will be employed in front of the HgCdTe detector to essentially eliminate the spontaneous emission background while passing the desired coherent signal.

REFERENCES

2-1. D.A.G. Deacon, L.R. Elias, J.M.J. Madey, G.J. Ramian, H.A. Schwettman, and T.I. Smith, Phys. Rev. Lett. 38, 892 (1977).

2-2. N.M. Kroll, P.L. Morton, and N.M. Rosenbluth, "Variable Parameter Free-Electron Laser," in Free-Electron Generators of Coherent Radiation, edited by S.F. Jacobs (Addison-Wesley, Reading, Mass., 1980) pp. 113-145.

2-3. J.M. Slater, J. Adamski, D.C. Quimby, T.L. Churchill, L.Y. Nelson, and R.E. Center, IEEE J. Quantum Electron. QE-19, 374 (1983).

2-4. G. Mavrogenes, M.B. James, R.F. Koontz, and R.H. Miller, Proc. of 11th International Conference on High-Energy Accelerators, CERN, Geneva, Switzerland, July 7-11, 1980, pp. 481-485.

2-5. J.E. Clondenin, G.A. Loew, R.H. Miller, J.L. Pellegrini and J.B. Truher, IEEE Trans. on Nucl. Sci. NS-28, 2452 (1981).

2-6. V.K. Neil, "Emittance and Transport of Electrons in a Free Electron Laser," SRI Report JSR-79-10 (December 1979).

2-7. R.H. Kingston, Detection of Optical and Infrared Radiation, Springer-Verlag, Berlin (1978).

Section 3

ADJUSTABLE TAPER WIGGLER

A new variable-taper wiggler has been designed and constructed for use in an investigation of the performance of tapers with favorable oscillator start-up properties. This new flexible wiggler will be used early in the next program in conjunction with the 10 μm small-signal gain and saturated extraction diagnostics to parameterize the FEL interaction with respect to photon wavelength and intensity. This will verify taper concepts for enhanced small-signal gain, large energy extraction, and minimal frequency chirp needed for operation of a short wavelength self-starting oscillator. The wiggler has been extensively characterized with respect to electron beam transport properties. The start-up enhancement analysis is presented in Section 3.1 and the wiggler hardware is described in Section 3.2. An additional task under this contract has been development of a preliminary wiggler design for a visible oscillator experiment. This work is described in Section 3.3.

3.1 START-UP CONSIDERATIONS

A key consideration in tapered-wiggler design is optimization of the taper to enhance oscillator start-up capability. The long length and low gain inherent in the tapered-wiggler FEL limits the device to slow starts at best. Linearly tapered wigglers with extraction efficiencies of interest tend to have a small-signal gain which is lower than the saturated gain by factors of 3 or more. In addition, start-up from spontaneous emission typically requires substantial frequency chirp. More favorable small-signal characteristics have been shown to be achieved by the use of prebunching optical klystron techniques.[3-1] Such techniques may avoid start-up time delays associated with low gain and chirp, and allow an optical cavity with output coupling that is optimum for saturated operation. However, these enhancements come at the expense of reduced allowable energy spread and emittance. Since initial visible oscillator

experiments will be operating near the limits of allowable energy spread and emittance for a linear taper, it may not be possible to achieve both large small-signal gain enhancement and elimination of chirp using prebunching techniques. However, MSNW studies have shown that modest but significant improvement in start-up characteristics can be achieved with taper modification as simple as inclusion of a short constant section in the wiggler taper, without significantly compromising emittance and energy spread acceptance.

A relevant result for the visible oscillator design of Section 3.3 is shown in Figure 3-1. The solid lines in the figure show the performance of a 5 m linearly tapered wiggler optimized for peak gain at 5 percent extraction. The gain is calculated based on a single narrow line that is allowed to chirp to the frequency of peak gain. Assuming the cavity losses can be kept at a low level, such a system will at best start up very slowly, since the peak small-signal gain does not exceed 5 percent. Once started, such a system would reach power levels far exceeding the design conditions, which would be undesirable due to possible optical damage considerations. By comparison, a wiggler with the same overall length and resonant energy change, but including an 80 cm long constant section in the taper prescription, has a small-signal gain of about 20 percent per pass. For 10 percent round trip cavity losses, such a system should saturate at an instantaneous power level of 6 GW, yielding approximately 5 percent extraction.

The use of such techniques for small-signal gain enhancement generally results in a narrowing of the small-signal linewidth, thus reducing the energy spread acceptance. As shown in Figure 3-2, the factor of 4 gain enhancement is achieved at the expense of only a 40 percent reduction in the linewidth. This appears to be a very useful tradeoff, particularly at visible wavelengths, since the emittance acceptance is generally limited by overlap rather than effective energy spread. Also shown in Figure 3-2 is the wavelength of peak gain as a function of photon

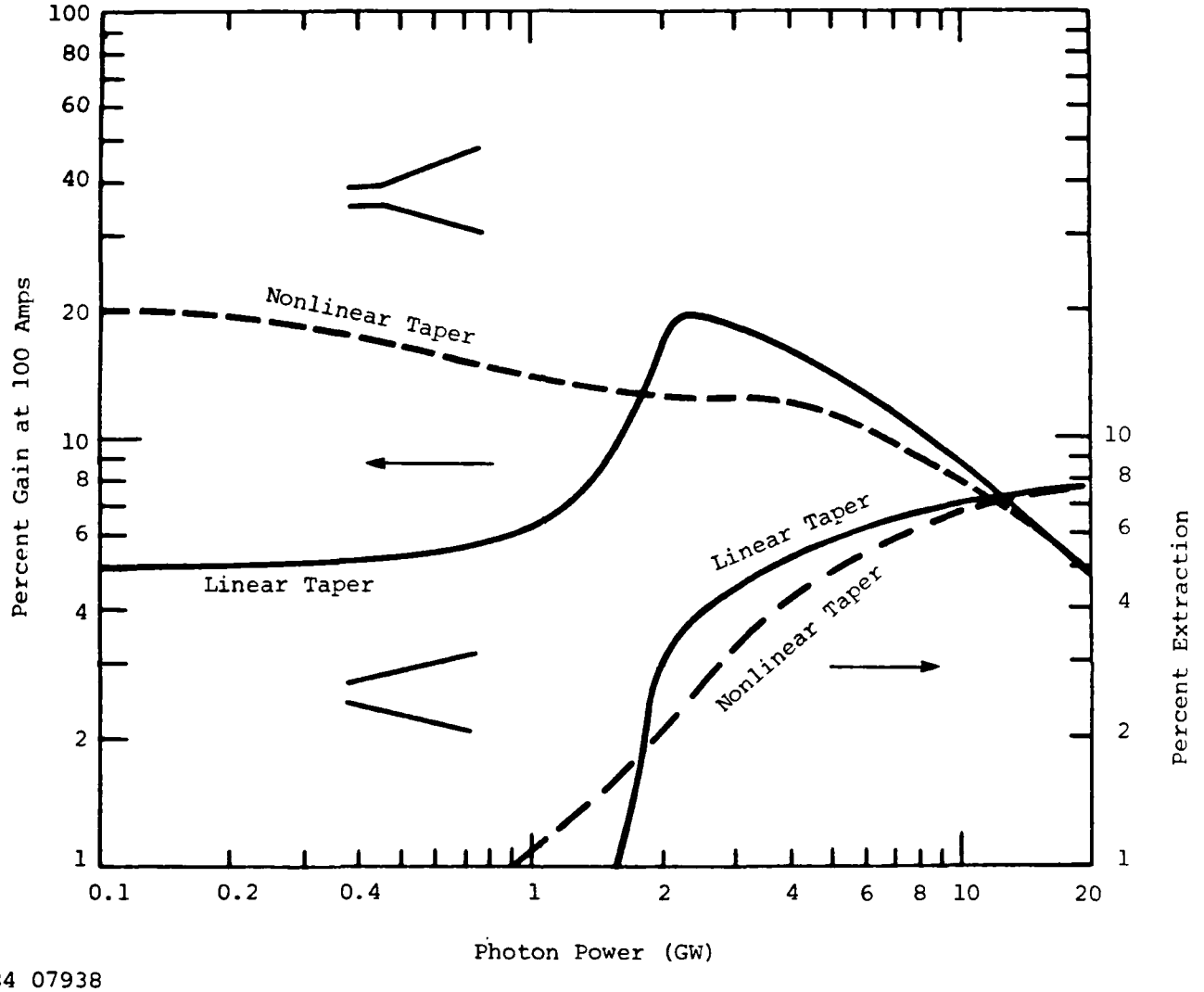

84 07938

Figure 3-1. Nonlinear Taper Enhances Small-Signal Gain. $\Delta\gamma_r/\gamma_r$ = 12.5 percent, L_w = 5 m, ϵ_N = 0.01 cm-rad, 1 percent energy spread, λ_s = 0.5 μm.

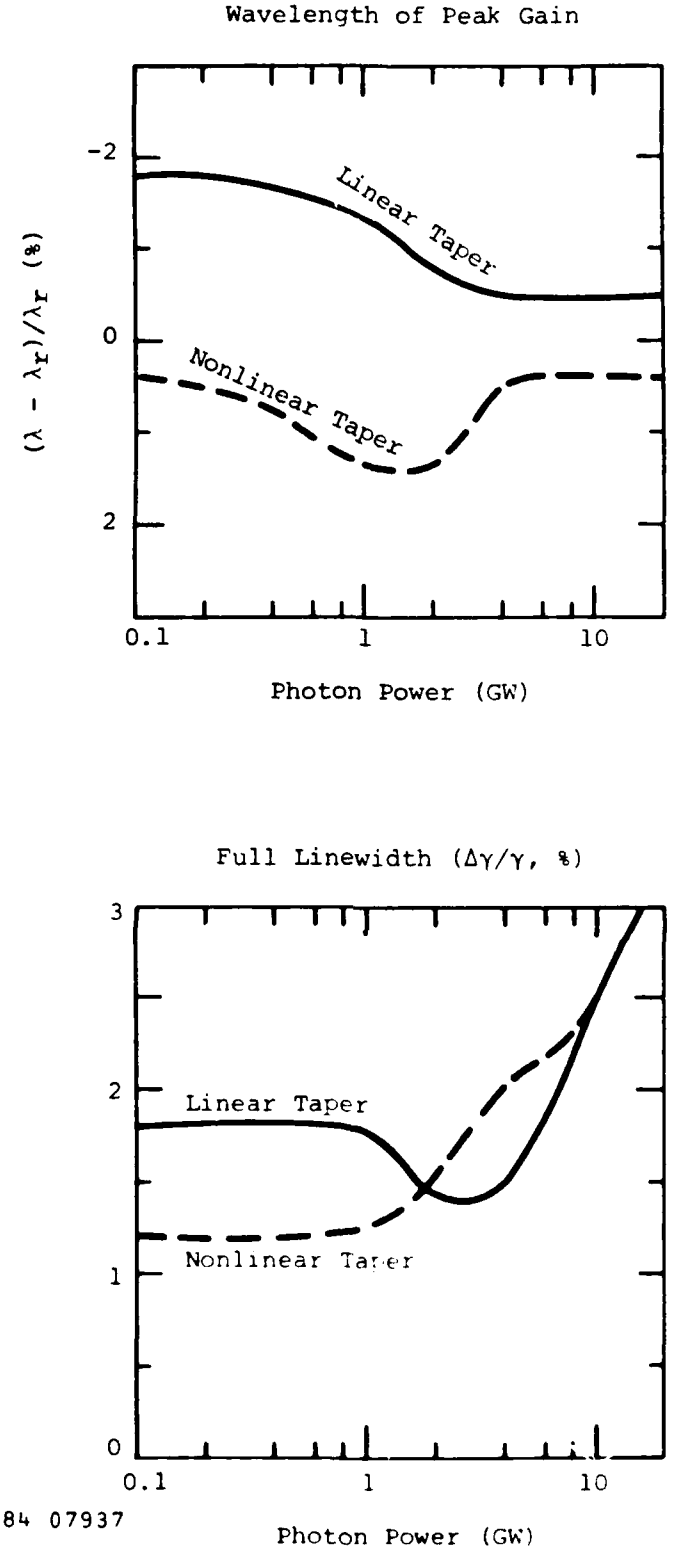

Figure 3-2. Nonlinear Tapering Affects Chirp Requirements and Linewidth, $\Delta\gamma_r/\gamma_r$ = 12.5 percent, L_w = 5 m, ε_N = 0.01 cm-rad, 1 percent energy spread, λ_s = 0.5 μm.

power for the two designs. Both taper prescriptions require a modest frequency chirp of less than 1.5 percent during start-up.

3.2 VARIABLE-TAPER WIGGLER HARDWARE DEVELOPMENT

This section describes the variable-taper wiggler built for testing improved tapers at 10 μm. A photograph of one side of the wiggler is shown in Figure 3-3. The taper adjustment is provided by means of variable magnet gap. This provides for rapid taper adjustment, which is essential due to expected magnet activation. The wiggler is composed of 25 cm long hinged segments, 9 to a side. The hinged subsections may be moved tranversely to vary the magnet gap and produce complex tapers. Each segment contains 32 magnets, which form 8 wiggler periods. Each samarium-cobalt magnet is mounted to an individual holder, each of which is held in the segments by retaining rods. As shown schematically in Figure 3-4, variable taper is provided by spring loaded antibacklash adjusting screws. Dial indicators at the position of each screw permit positioning resolution of 0.001 in. for each segment. The wiggler is designed to mount on the existing 0.5 in. OD vacuum system, which has access for e-beam position and profile diagnostics at three places along the wiggler length, as well as at the entrance and exit. Other features which may be seen in Figure 3-3 include a rotatable end-magnet and field error compensation coils built into each wiggler segment.

The system design parameters are listed in Table 3-1. The design is optimized for maximum FEL interaction strength using a gain-extraction optimization analysis similar to that described in Section 4.1.1. In the optimization we have used the actual e-beam energy-current relationships for the BAC Linac and have allowed for the longitudinal dependence of the magnet gap and field strength, an important consideration for tapered-gap wigglers.

Initial FEL experiments have shown that undesirable steering of the e-beam can result from nonuniform magnetization of the $SmCo_5$.

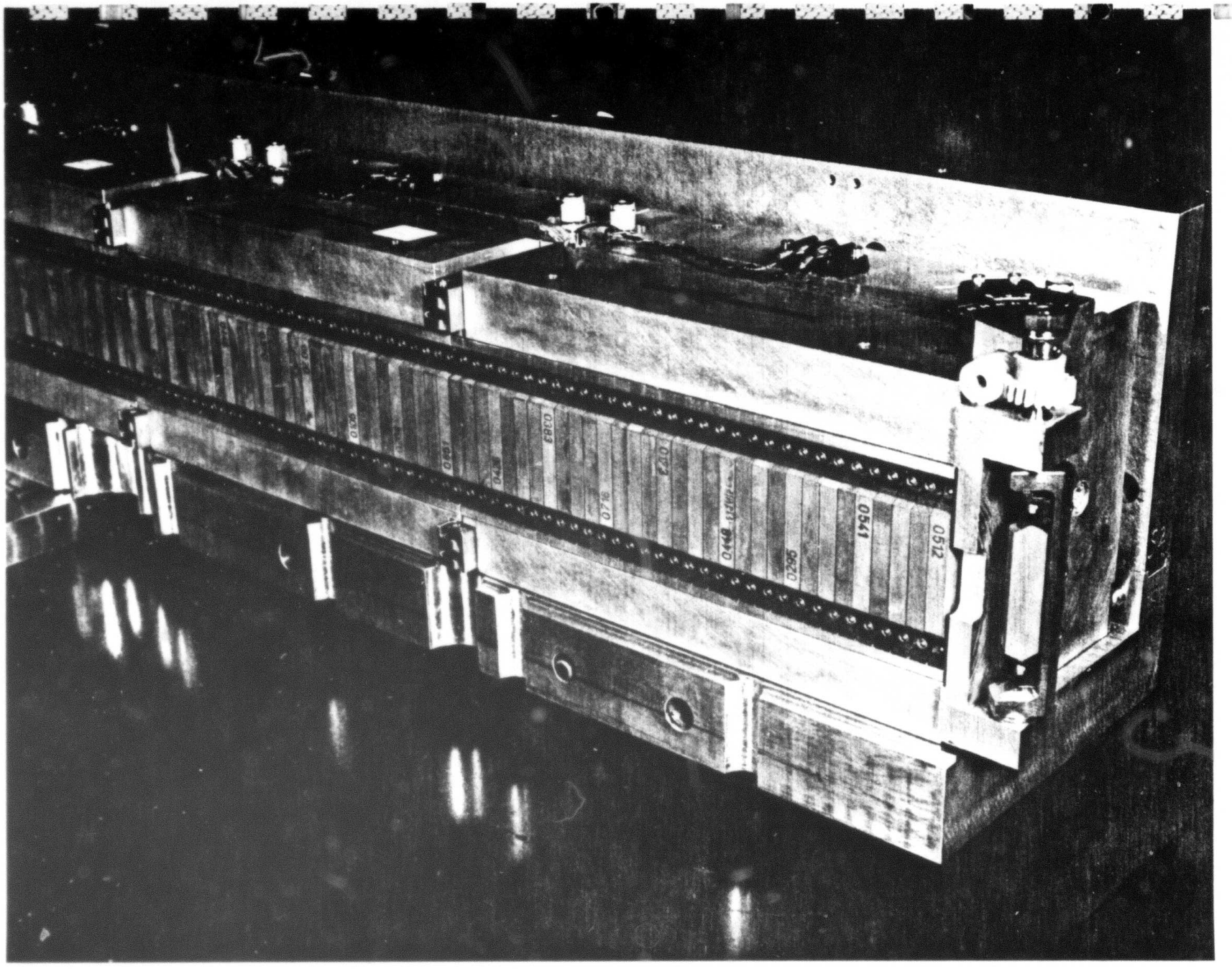

Figure 3-3. Photograph of Variable-Taper Wiggler.

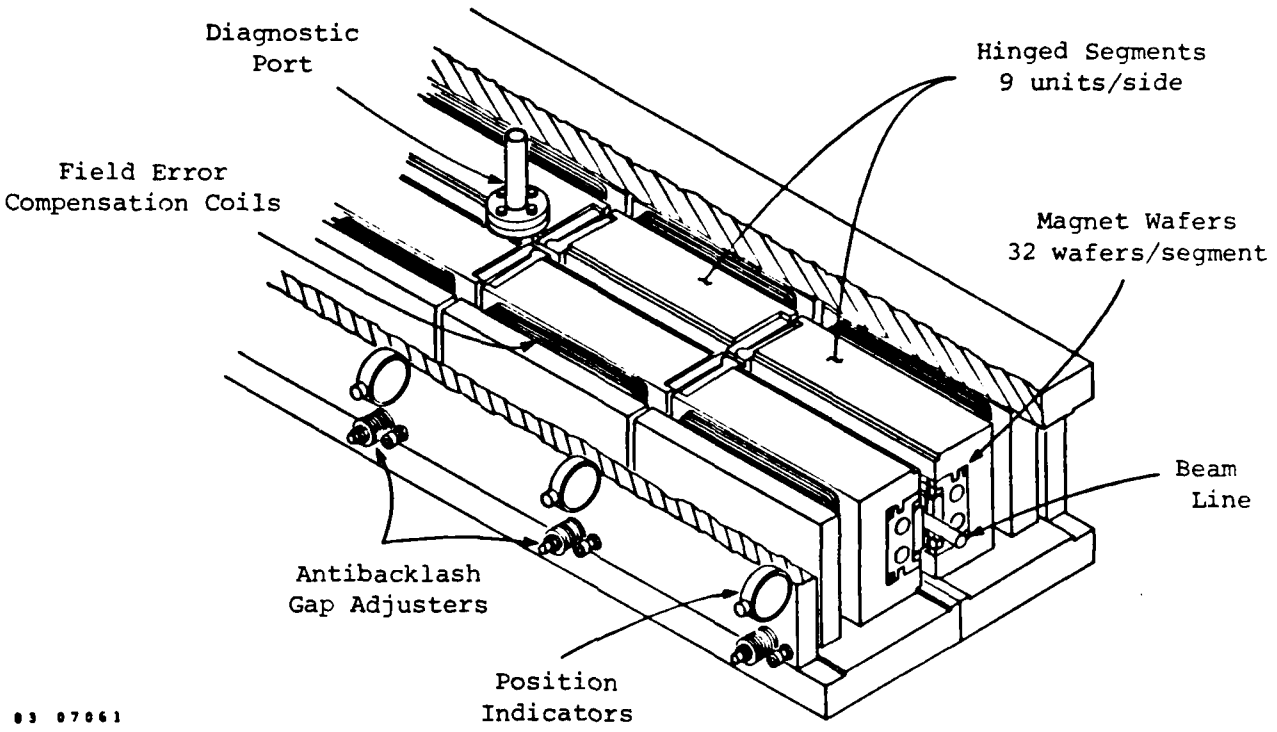

Figure 3-4. Sketch of Adjustable-Gap Segmented Wiggler for Testing of Non-Linear Tapers.

Table 3-1

PARAMETERS OF 10.6 μm ADJUSTABLE-GAP WIGGLER

Resonant Energy	25 MeV
Length	2.3 m
Taper ($\Delta\gamma_r/\gamma_r$)	Adjustable, 10% max.
Wiggler Wavelength	3.1 cm
Peak Magnetic Field	4.1 kG
a_w (rms)	0.83
Full Gap at Entrance	1.27 cm
Full Gap at Exit	1.58 cm at max. taper
Rayleigh Range	0.65 m
Clearance Factor (full gap/optical beam diameter)	2.1
Betatron Period (single-plane focus)	1.9 m
Normalized Emittance Acceptance Based on Overlap[a]	0.027 cm-rad
Normalized Emittance Acceptance Based on Effective Energy Spread[a]	0.12 cm-rad
Energy Spread Acceptance[a]	2.0%

[a] For maximum taper (10%), this value gives 50% gain loss at fixed extraction.

Understanding these effects is of paramount importance to optimal performance, and these problems have been pursued vigorously at MSNW.

The e-beam steering difficulty results from the unexpectedly large variations found in $SmCo_5$ bulk properties. Hall probe measurements made using the test block shown in Figure 3-5 show that the magnets have significant bar to bar variation in the average level of magnetization and in the orientation of the magnetization vector with respect to the magnet faces. Some example results are shown in Figure 3-6. The strength and angle parameters are measured at the point of closest approach by the electron. The level of magnetization is found to vary by several percent and the angle of magnetization typically varies by several degrees. The resulting departure of the wiggler field from the ideal value causes two separate problems. First, some trapped particles are lost from the ponderomotive potential well because of phase and amplitude noise in the B-field. This field deviation occurs on a length scale short compared to the distance the electron travels while making one orbit in the potential well, so that the noise tends to have only a small effect on the trapping. The second, much more important problem is electron beam steering caused by the field errors. They will result in trajectory errors which exceed the size of the photon beam even if the deviations occur randomly from magnet to magnet.

Two methods of compensation are used to reduce steering to an acceptable level. First, using the Hall probe data, a magnet matching algorithm has been developed to reduce the effect of variations on a local level. The primary emphasis of this sorting algorithm is reduction of steering errors while phase and amplitude noise is compensated to a lesser degree. The shaded histograms in Figure 3-6 show the magnets selected for use in the wiggler based on this sorting algorithm. The second level of compensation involves use of external trim coils based on properties of the fully assembled wiggler. The field errors within the 9 pairs of completed wiggler subsections were measured using floating wire techniques. Results are shown in Figure 3-7(a). Wiggle-plane steering errors of several mrad

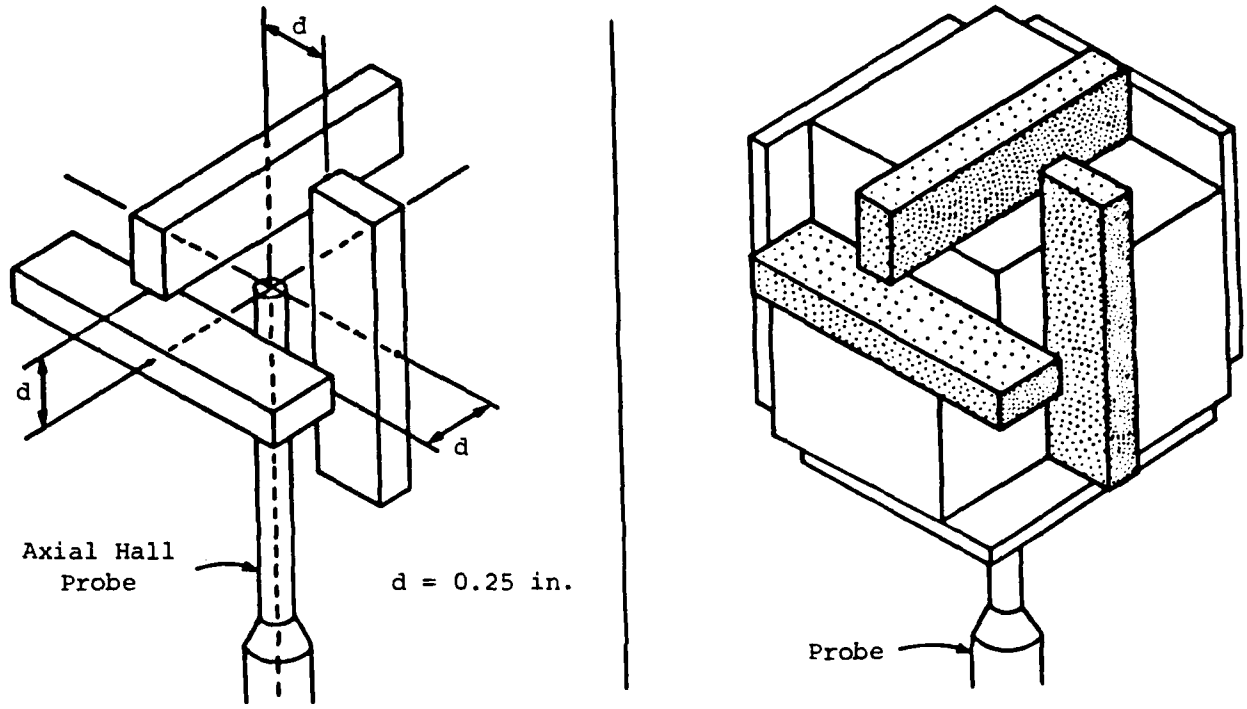

Figure 3-5. Test Block for up to 10 Hall Probe Measurements per Magnet to Identify Amplitude and Alignment Errors

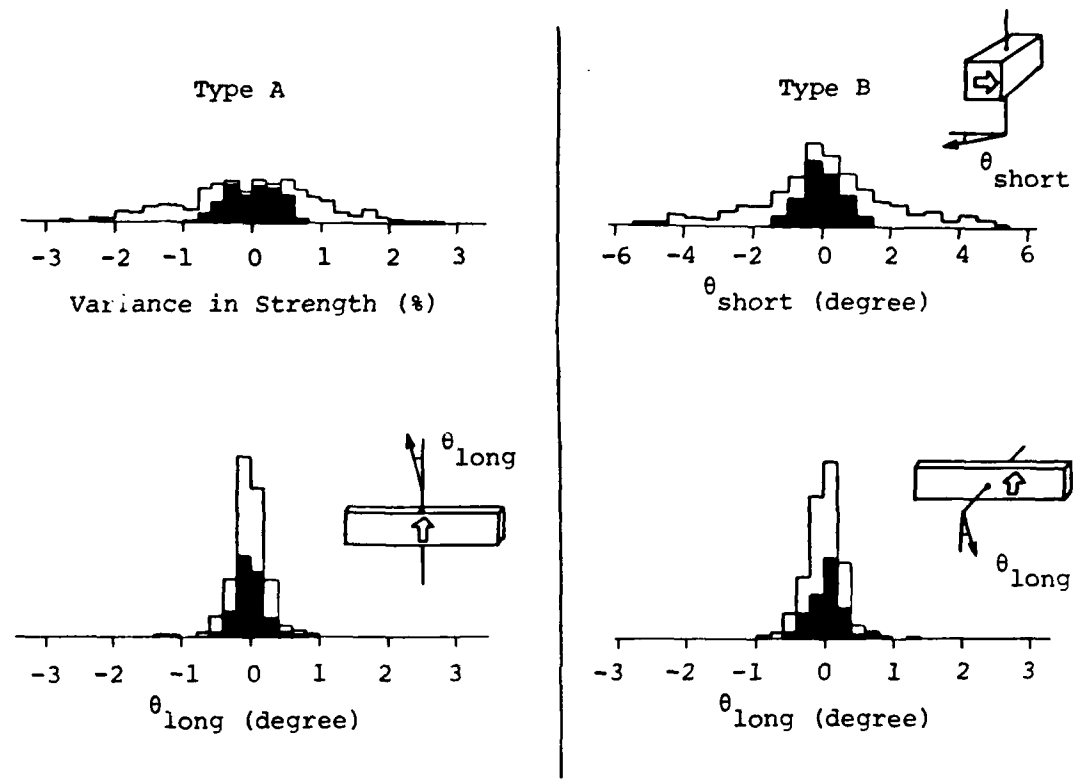

84 08075

Figure 3-6. Individual Magnet Characteristics Based on Hall Probe Measurements. The unshaded histograms indicate the properties of the entire lot of magnets while the shaded histograms show the magnets selected for use in the wiggler.

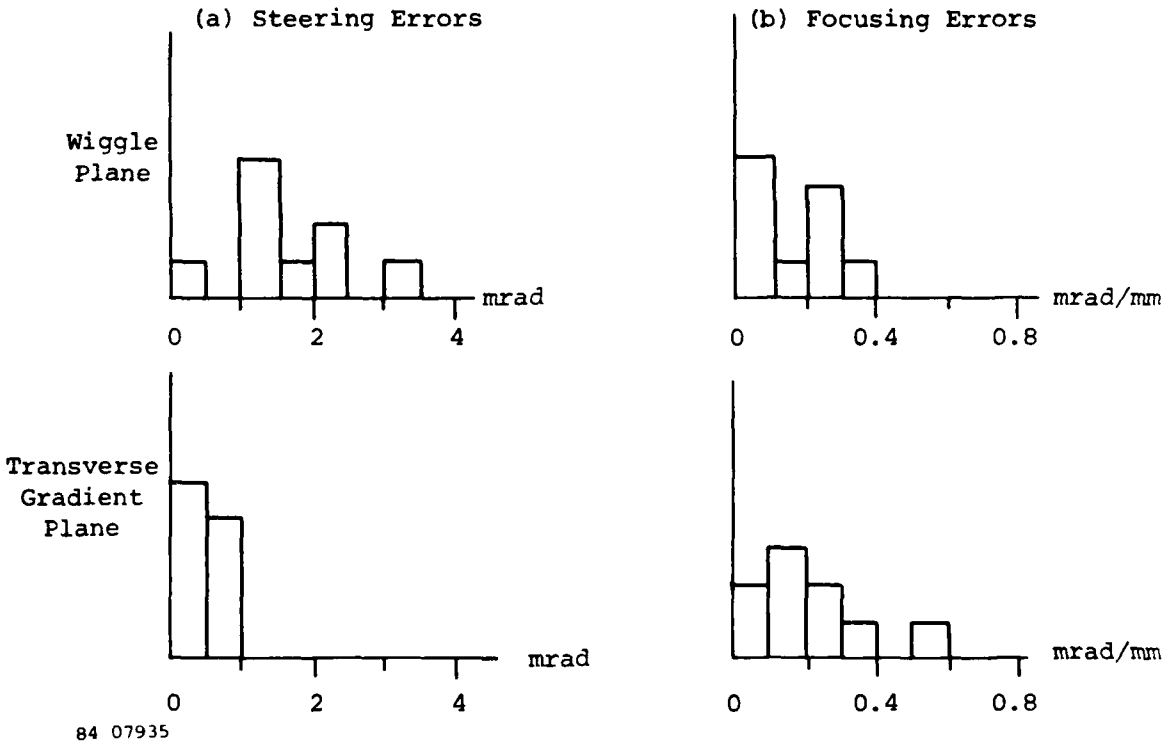

Figure 3-7. Measured Field Errors in 25 cm Wiggler Subsections.

are present within several of the magnet subsections. While the ponderomotive potential noise remains unimportant, the steering errors are significant and require correction. Fortunately, such errors are readily correctable using the trim coils provided for that purpose. The measured errors, however, indicate that the sorting algorithm did not achieve the desired precision.

The discrepancy between the expected and actual field errors of the assembled wiggler is due in part to poor correlation between the point B-field measurements and B-field line integrals along the full path of the electron beam. Detailed Hall probe measurements were completed for a few selected magnet bars to determine the magnetic field distribution along the entire electron path. It was found that the steering characteristics of these bars, as determined from the line integral of B along the electron path, did not correlate well with steering characteristics which might be deduced from measurements at the single point of closest approach. An additional source of discrepancy may be due to demagnetization at the time of wiggler assembly. The demagnetizing H field for magnets in the presence of the entire wiggler array is shown in Figure 3-8. These contours of constant H are calculated under the assumption of unity permeability (cgs units) and constant magnetization. The areas of $\mu_o H/M \approx -1$ will suffer some permanent demagnetization. This loss of magnetization is the reason for the slight rolloff in the B-H curve as $\mu_o H/M$ nears -1. Field errors will result if individual magnets demagnetize to differing degrees. No definitive measurements were made which would indicate to what extent demagnetization affects this wiggler.

High precision floating wire diagnostic techniques were developed under this contract for providing definitive characterization of the magnetic field distribution in each plane of the assembled wiggler. This field error diagnostic is shown schematically in Figure 3-9. The steering properties of a pair of wiggler subsections can be measured by observing the transverse deflection of the small current carrying wire. Optical micrometers are used to observe the wire deflection in both transverse

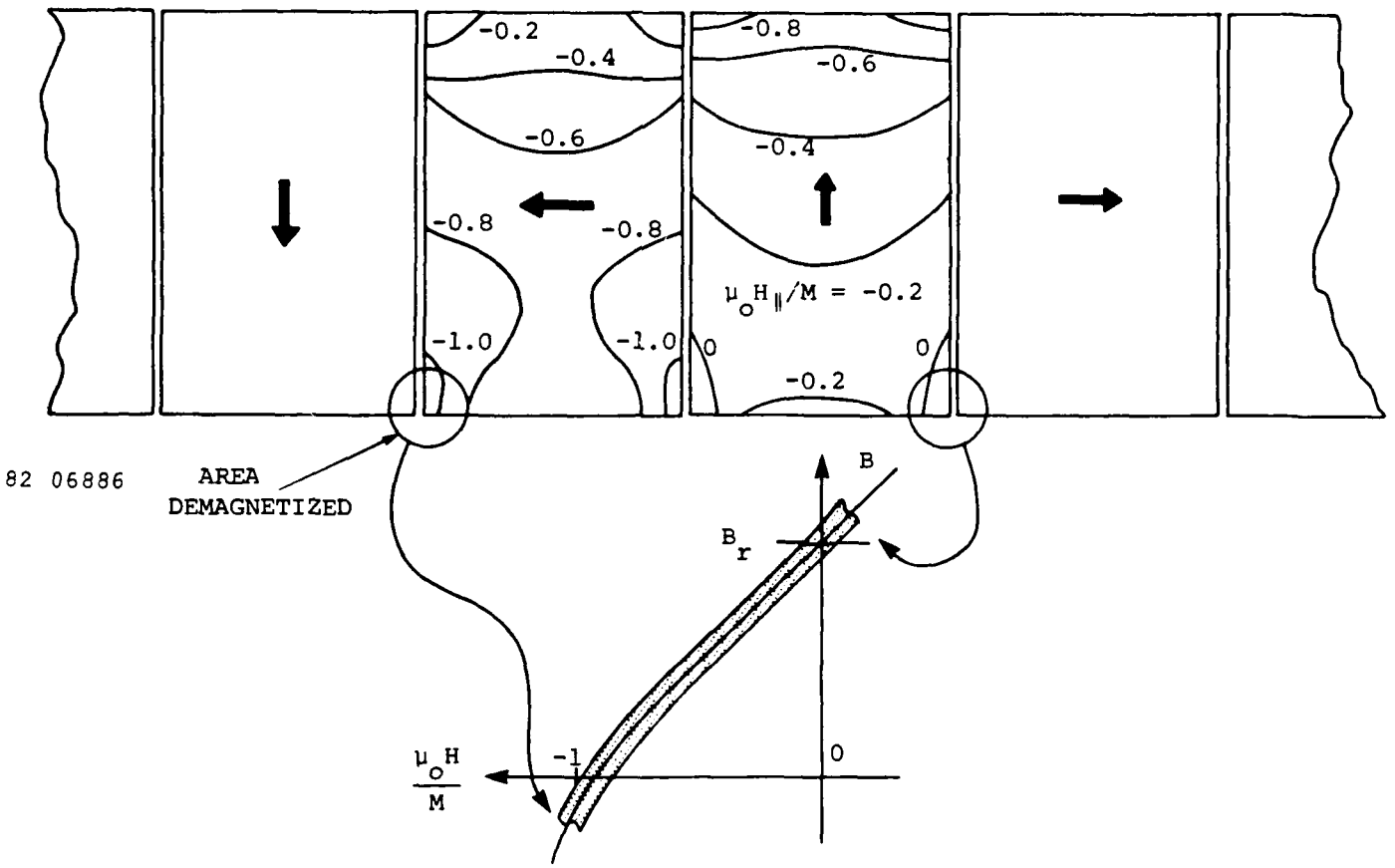

Figure 3-8. Demagnetizing Field for Magnets in Assembled Wiggler, the Contour Lines are of $\mu_o H/M$, where M ($=B_r$) is the Level of Magnetization. Only the H-field component in the direction of $\bar{M}$ is considered. The areas of $\mu_o H/M \approx -1$ will suffer some demagnetization as shown by the gentle roll off in the B-H curve as $\mu_o H/M$ approaches -1.

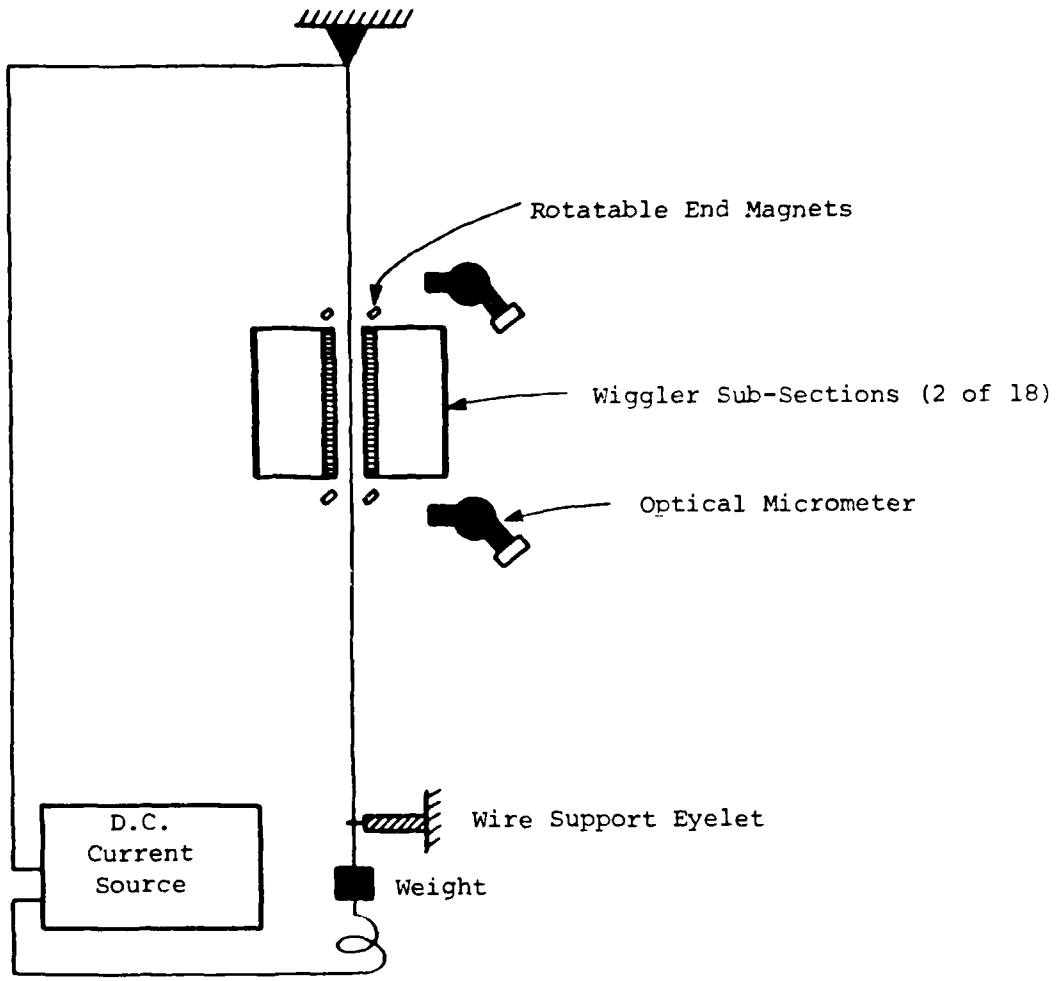

Figure 3-9. Floating Wire Diagnostic of Assembled Wiggler Subsections.

planes. Matched rotatable end magnets are used to compensate for the earth's field and to provide proper entrance conditions at each end of the wiggler. This is the measurement technique that was used for the steering measurements of Figure 3-7(a). By moving the nominal position of the wire slightly off-axis, the gradients in the steering errors may also be measured. Steering gradients are due to quadrupole components in the field. The floating wire technique was used to examine the e-beam steering gradients in each pair of subsections of the new adjustable-gap wiggler. This constitutes the first measurement of quadrupole field errors in any wiggler. Results are shown in Figure 3-7(b). Steering gradients of several tenths of a mrad/mm are present in both planes. These field errors cause extraneous focusing and, in principle, are correctable by introduction of external adjustable focusing. External focusing is not provided in this wiggler, however. Error fields of order higher than quadrupole fields would be even less easily correctable.

Results of a simulation of the effect of the measured quadrupole components is shown in Figure 3-10. Electron trajectories are computed in the wiggle plane phase space of the adjustable-taper wiggler including the effect of the measured steering gradients but assuming that gross steering errors are perfectly corrected. The heavy dots represent the ideal electron trajectories, which keep all electrons within the ideal phase space ellipse, thus maximizing overlap with the optical beam. The small dots represent trajectories calculated including the steering gradients. Some electrons fall outside the ideal envelope and the emittance phase space area grows slightly. Similar results are found in the other plane as well. This loss of overlap can be partially compensated by injecting the electrons into the wiggler with slightly different entrance conditions. The impact of the steering gradients on the FEL interaction strength can be evaluated by calculating the electron energy extraction including the effect of the modified electron trajectories. In this case, the degradation of interaction strength is found to be negligible. Field error gradients of this magnitude should not be troublesome at visible wavelengths either. However, magnets of equivalent uniformity to these may

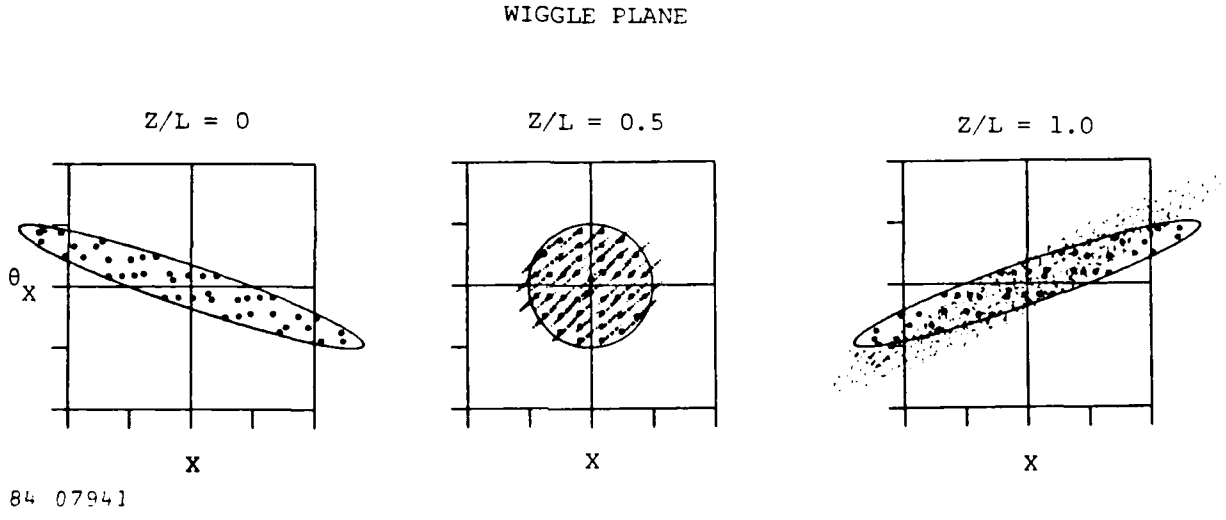

Figure 3-10. Steering Gradients Result in Extraneous Focusing. Effect on extraction is negligible at 10 μm.

cause larger gradients at the reduced magnet gaps which will be used for visible experiments.

3.3 WIGGLER DESIGN FOR VISIBLE OSCILLATOR

A preliminary point design has been developed for a wiggler suitable for visible oscillator experiments. Parameters of this design are given in Table 3-2. The design is based on the need to maintain gain at small-signal and saturated photon fluxes, as well as to provide adequate emittance and energy spread acceptance. The design was optimized for the Boeing linac using gain-optimization analysis described in Section 4.2.3, which includes the effects of emittance and energy spread on the interaction strength. An artist's concept of the wiggler is shown in Figure 3-11. Two-plane focusing is included to provide the required emittance acceptance. An easily varied taper is provided for testing oscillator performance with various degrees of taper and to allow use of advanced taper schemes for start-up improvement. The design is of the hybrid type,[3-2] incorporating $SmCo_5$ and steel.

Possible wiggler types include permanent magnet, hybrid, superconducting, and pulsed electric. In recent years, permanent magnet designs have been much preferred for their reliability and simplicity.[3-3] In addition, permanent magnet designs have inherent advantages at the small wiggler periods of interest. At small dimensions, superconducting and normal conducting coils would have to exceed fundamental current density limits to produce field strength of permanent magnets. Hybrid configurations incorporating $SmCo_5$ and steel have advantages over pure $SmCo_5$ geometries in achievable field strength for small gap to period length ratios. As shown in Figure 3-12, taken from Reference 3-3, the optimum gap to period ratio for a 0.5 micron wiggler is in a range where the hybrid design looks very attractive. For the magnet gaps of interest, the hybrid design can produce a field strength approximately 50 percent higher than that of a pure $SmCo_5$ design, or, alternatively, the hybrid design can produce the same field at approximately 50 percent larger gap.

Table 3-2

PRELIMINARY POINT DESIGN FOR 0.5 μm
OSCILLATOR EXPERIMENT

E-Beam Energy	120 MeV
Peak Current	100 A
Wiggler Length	5 m
Taper ($\Delta\gamma_r/\gamma_r$)	Adjustable, 12% max.
Wiggler Wavelength	2.18 cm
Peak Magnetic Field	8.7 kG
a_w	1.25
Full Gap at Entrance	0.55 cm
Full Gap at Exit	0.67 cm at max. taper
Rayleigh Range	2.2 m
Clearance Factor (full gap/optical beam diameter)	3.1
Betatron Period (two-plane focus)	5.8 m
Normalized Emittance Acceptance Based on Overlap[a]	0.014 cm-rad
Normalized Emittance Acceptance Based on Effective Energy Spread[a]	0.048 cm-rad
Energy Spread Acceptance[a]	1.5%
Small-Signal Gain[b]	20%
Single-Pass Gain at 5% Extraction[b]	10%
Instantaneous Photon Power at 5% Extraction[b]	6 GW

---

[a] Assumes equal two-plane focusing provided by wiggler, and maximum taper (12%). This value gives 50 percent gain loss at fixed extraction.

[b] Assumes nonlinear taper, ϵ_N = 0.01 cm-rad, Energy Spread = 1 percent.

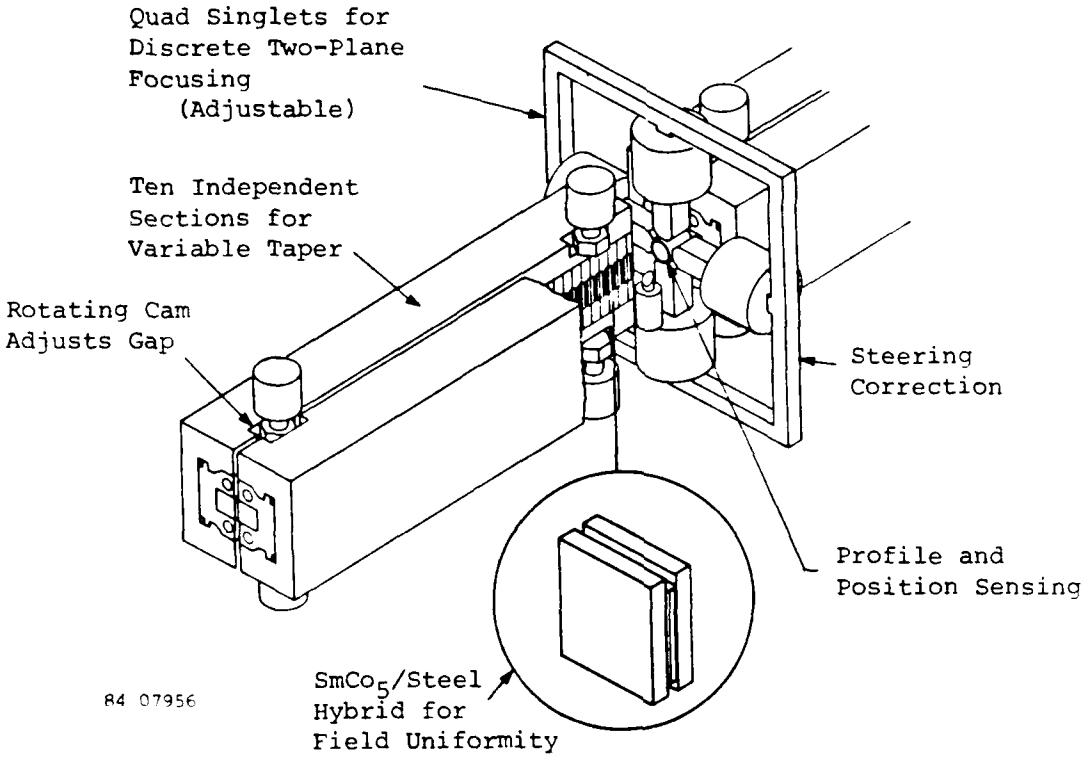

Figure 3-11. Sketch of Hybrid Wiggler Concept for Visible Oscillator.

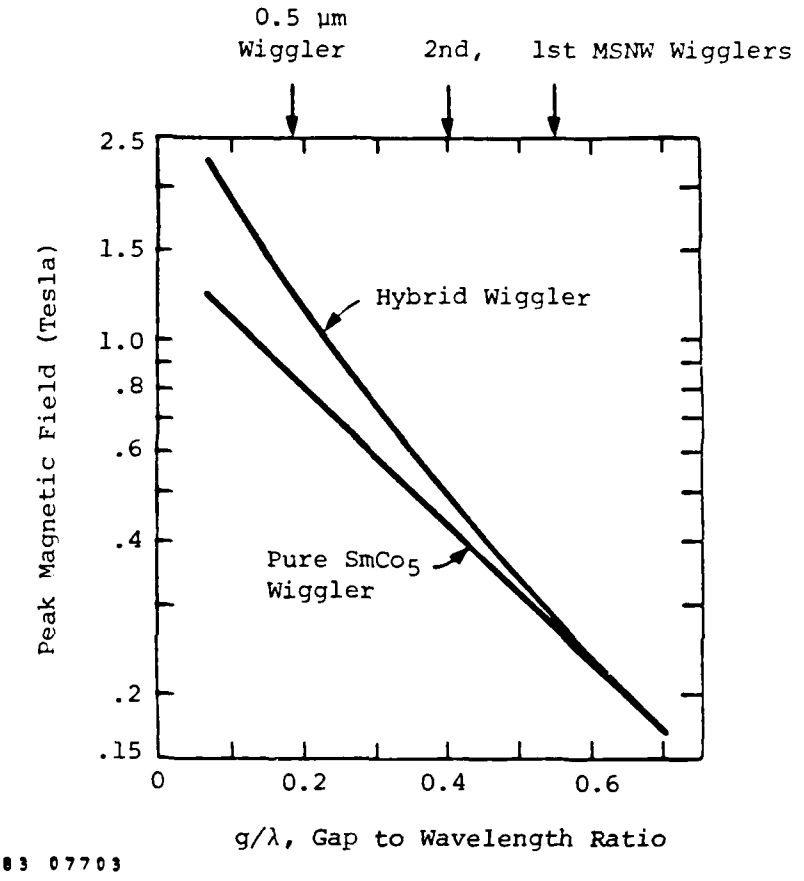

Figure 3-12. Peak Midplane Fields in Hybrid and Rare Earth Cobalt Wigglers (from Reference 3-3).

A far more overwhelming advantage of the hybrid is that the field distribution is only weakly dependent upon the magnetic properties of the $SmCo_5$. Achievement of good field uniformity in the hybrid is dependent upon holding mechanical tolerances rather than on obtaining very high quality permanent magnet material. The hybrid design gives up several desirable properties, however. Due to the inclusion of nonlinear magnetic material, it is no longer possible to linearly superimpose external fields for steering corrections or adjustable two-plane focusing strength. Steering can, in principle, be provided by breaking the wiggler into subsections and providing electromagnet steering coils in the gaps between sections. In addition, design analysis of the hybrid is made more difficult by the requirement of a numerical code to calculate field distributions including the effect of the nonlinear saturable material. Code predictions can be verified by field distribution measurements in small hybrid prototypes.

The preliminary choice of a hybrid design results primarily from the desirable field uniformity possible with this design. Since visible experiments will be operated at near the maximum allowable emittance, the wiggler field will have to be tuned to ensure that the e-beam trajectory is aligned with the photon beam to near the theoretical precision allowed by the emittance. The hybrid design appears to be a promising way to reduce both gross steering errors and higher order field error components. While the measured steering gradients in the pure $SmCo_5$ 10 μm adjustable wiggler do not seriously degrade the FEL interaction in present experiments, it is not known how the smaller magnet gaps needed for 0.5 μm wigglers will affect the steering gradients. Field distribution measurements should be made at reduced gap in small wiggler prototypes prior to finalizing a 0.5 micron wiggler design.

The wiggler for the system design described in Table 3-2 is very similar to wigglers used in present experiments aside from the reduced magnet gap required to maximize the interaction strength at visible wavelengths. The gap shown in Table 3-2 is based on a hybrid magnet

configuration; a pure $SmCo_5$ wiggler would require about a 30 percent smaller gap to achieve the same parameters. Because of the reduced dimensions, some mechanical tolerances become very tight in order to maintain good field uniformity. The magnet pole faces must be positioned to within about 20 microns of their ideal location. A considerable portion of the program for development of such a wiggler will be devoted to avoidance of tolerance stackup by use of precision machining techniques and by achievement of extremely fine accuracy in mechanical measurements.

REFERENCES

3-1. M.Z. Caponi and C.C. Shih, "Gain and Efficiency Enhancement by a Multicomponent Wiggler Free-Electron Laser," Phys. Rev. A, 26, 2285 (1982).

3-2. E. Hoyer, T. Chan, J.W.G. Chin, K. Halbach, K.J. Kim, H. Winick, and J. Yang, "The Beam Line VI REC-Steel Hybrid Wiggler for SSRL," Lawrence Berkeley Laboratory Report LBL-15115 (March 1983).

3-3. K. Halbach, "Permanent Magnet Undulators," Proceedings of Bendor Free-Electron Laser Conference, J. de Physique, 44, p. C1-211 (1983).

Section 4

ELECTRON-BEAM QUALITY REQUIREMENTS FOR TAPERED-WIGGLER FREE-ELECTRON LASERS

A key technology issue in applying the tapered-wiggler concept at short photon wavelengths concerns the capability of linear accelerators to produce electron beams with the small emittance and energy spread required by the FEL. The limited e-beam power available with small emittance and energy spread, together with the high optical power required for energy extraction, limits the tapered-wiggler single-pass gain. The motivation of this section is to gain a proper understanding of the optimization and scaling of the tapered-wiggler FEL gain including limitations due to emittance and energy spread, to aid in development of a high efficiency, high-power FEL at visible wavelengths. Emittance requirements for untapered wigglers driven by linear accelerators have previously been developed by Smith and Madey[4-1] and Dattoli, et al.[4-2] In addition, Madey has discussed the emittance requirements for storage-ring driven FELs.[4-3]

The general approach to optimization of the FEL interaction strength described in Section 4.1 is used to develop the scaling laws for emittance and energy spread requirements for optimized planar wigglers. The scaling laws are then anchored by numerical simulation of the degradation of FEL interaction strength due to these effects. Results of the gain optimization analysis are presented in Section 4.2. The e-beam requirements are found to be quite stringent at visible wavelengths, but the emittance requirement can be substantially relaxed if the wiggler focuses in both planes. In addition, possible tradeoffs are examined which relax the e-beam emittance and energy spread requirements still further, but at lower gain per unit e-beam current. Implications are addressed in Section 4.3.

4.1 GAIN OPTIMIZATION

A general approach to the problem of optimization of the FEL interaction is developed in this section, leading to specific requirements for the wiggler and e-beam properties. The gain-extraction product is a useful figure of merit for the tapered-wiggler FEL interaction strength since gain can be traded for extraction (and vice versa) by changing the wiggler taper.

4.1.1 Gain-Extraction Product

The gain-extraction product, ξ, has been shown[4-4] to be given by (cgs units)

$$\xi = \frac{128\pi^2 e}{mc^3} (\delta \sin\psi)^2 \gamma I \chi^2 , \qquad [4-1]$$

where

$$\chi = \frac{1}{\alpha} \frac{h}{\lambda_w} \frac{a_w}{\left[1 + a_w^2\right]} \frac{\ln\left[q + \left[1 + q^2\right]^{1/2}\right]}{(1 + q^2)^{1/2}} , \qquad [4-2]$$

δ is the fraction of electrons trapped in the ponderomotive well, $\sin\psi$ is the average sine of the phase angle for trapped electrons, γ is the electron energy in units of the rest mass mc^2, I is the electron current, α is the ratio of magnet half-gap h to the 1/e photon beam amplitude radius w_e at the wiggler entrance and exit, $a_w = eB_o\lambda_w/2^{3/2}\pi mc^2$, B_o is the peak B-field, λ_w is the wiggler wavelength, $q = L_w/2Z_R$, L_w is the wiggler length, and Z_R is the Rayleigh range of the photon beam. Equation [4-1] does not include degradation of the gain-extraction product due to energy spread and emittance; these effects will be introduced later. Equation [4-1] is derived under the assumptions of small fractional change in the resonant energy,

$$\gamma_r^2 = \frac{\lambda_w}{2\lambda_s} \left[1 + a_w^2\right] , \qquad [4-3]$$

and low gain. The electron dynamics are idealized by assuming that trapped electrons behave as the synchronous-phase particle[4-5] does, so that, in essence the optimization is for a single electron traveling along the wiggler axis.

The assumed geometry is shown in Figure 4-1. A diffraction-limited photon beam is focused in the center of a planar wiggler. A Halbach[4-6] magnet configuration is used. The permanent magnets have polarization vectors oriented as indicated by the arrows in Figure 4-1. In order to properly reflect the physical limitations of developing large magnetic fields in this geometry, we write a_w in terms of the basic magnet parameters h, λ_w, and the remanent magnetization, B_r. For the magnet bar height $g = 3\lambda_w/8$ and no gaps between neighboring magnets, the calculated field may be expressed as[4-6]

$$a_w = 1.07 \times 10^{-4} B_r \lambda_w e^{-2\pi h/\lambda_w} . \qquad [4-4]$$

Using a typical peak value of $\delta\sin\Psi$ of 0.26 (based on numerical simulation results), a conservative clearance factor α of 2, and B_r = 9000 G typical of $SmCo_5$ magnets, the gain-extraction product is now a function of L_w, λ_w, h, λ_s, Z_R, and I. Optimization of Equation [4-1] depends on which parameters are fixed and which are varied to produce the maximum. The case of λ_s, L_w, and I fixed is considered here. These choices allow the wiggler length to be held to a practical value and assume that the peak current available is limited. It is to be noted that when optical component damage is an issue, Z_R may be a more useful independent parameter than L_w, since Z_R partly determines the beam size on the resonator mirrors. Fixing λ_s, L_w, and I apparently leaves a three-dimensional surface to be examined, but h and Z_R are not independent of one another (due to the fixed clearance factor α) and the resulting two-dimensional space is easily analyzed to find the system parameters yielding the maximum gain-extraction product.

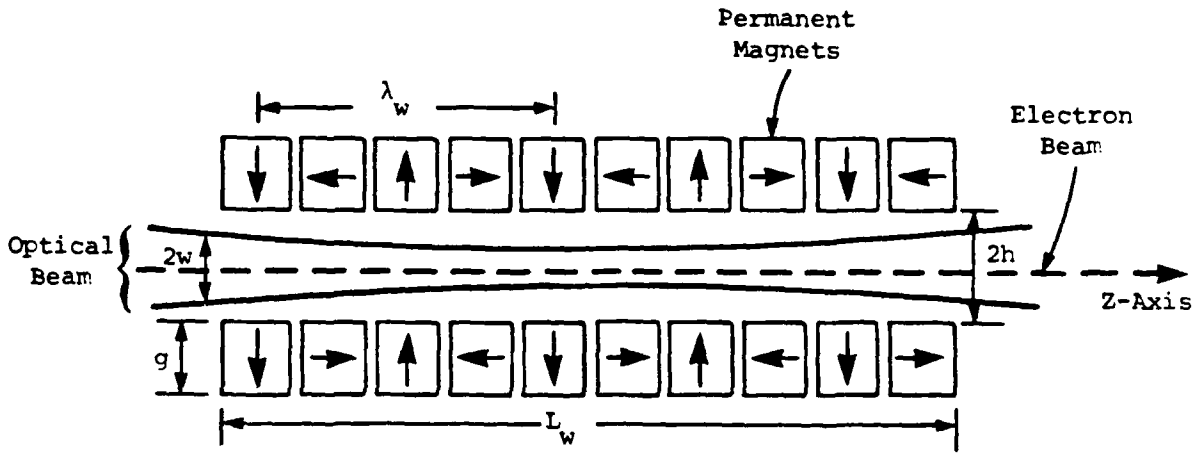

82 06271

Figure 4-1. FEL Geometry for Optimization Analysis.

The e-beam energy spread and emittance requirements can also be determined as a function of the system parameters. The allowable energy spread is determined by the requirement that it cannot exceed the ponderomotive bucket full height. Similarly, the allowable emittance is set by the combined requirements that the effective energy spread due to emittance be less than the bucket height and that the electron and photon beams overlap spatially.

4.1.2 Energy Spread Requirements

For a tapered-wiggler, the energy spread must be less than the ponderomotive bucket height full width, given by[4-5]

$$H = \left[\frac{\Delta\gamma}{\gamma}\right]_{\text{Bucket}} = 2\left[\frac{2\lambda_s e_s a_w F[\psi_r]}{\pi\left[1+a_w^2\right]}\right]^{1/2}, \qquad [4\text{-}5]$$

where $e_s = eE_o/2^{1/2}m_oc^2$ is the normalized rms E-field, $F(\psi_r) = \cos\psi_r - (\pi/2 - \psi_r)\sin\psi_r$, and parameter ψ_r is the phase angle in the ponderomotive potential well for the electron whose energy loss rate exactly matches that of the wiggler resonant energy. A phase angle of about 40 degrees maximizes the product of trapping fraction and bucket deceleration rate for the case of a monoenergetic, zero emittance beam. At photon flux levels too low to result in trapping, the allowable energy spread corresponds to the homogeneous small-signal linewidth. Using the linewidth defined by Brau[4-7] for the linearly tapered wiggler gives an allowable energy spread of

$$\frac{\Delta\gamma}{\gamma} = \frac{1}{2}\frac{\Delta\lambda_s}{\lambda_s} = \left[\frac{\lambda_w}{\pi L_w}\frac{\Delta\gamma_r}{\gamma_r}\right]^{1/2}, \qquad [4\text{-}6]$$

where $\Delta\gamma_r$ is the resonant energy change of the wiggler taper. It is of interest to compare the energy spread requirements at small-signal and saturated flux levels. Since saturation (the onset of trapping) occurs for an E-field value of roughly

$$e_s = \frac{\gamma_r^2}{a_w L_w} \frac{\Delta\gamma_r}{\gamma_r} , \qquad [4-7]$$

the bucket full width at saturation is, for $\psi_r \approx 40°$,

$$\left[\frac{\Delta\gamma}{\gamma}\right]_{\text{Bucket}} \approx \left[\frac{\lambda_w}{\pi L_w} \frac{\Delta\gamma_r}{\gamma_r}\right]^{1/2} , \qquad [4-8]$$

which is equal to the equivalent energy-width due to the small-signal linewidth. Thus, the energy spread requirements for a linearly tapered wiggler at small-signal and saturated conditions are identical. At flux levels well above the onset of saturation, the energy spread requirements relax as the bucket size grows.

4.1.3 Emittance Requirements

The allowable emittance in the focusing plane of a planar wiggler is often set by the requirement that the effective energy spread due to emittance be less than the bucket height. For such cases, in which spatial overlap is not the limiting factor, determination of the allowable emittance is based on the principle that electrons with slightly different trajectories interact in the same way as electrons with identical trajectories but slightly different energies. The trajectory difference is of course related to the emittance, with the consequence that the allowable emittance can be directly related to the allowable energy spread.

The effective energy spread due to emittance may be determined by examining the variation in transverse momentum and B-field experienced by an electron which executes the betatron orbit[4-8] of maximum amplitude. The effective energy spread full width is found to be

$$\left[\frac{\Delta\gamma}{\gamma}\right]_{\text{Equiv}} = \begin{cases} \dfrac{k_w^2 a_w^2 \epsilon_N}{2\pi\gamma k_\beta \left[1 + a_w^2\right]} & k_\beta < \dfrac{a_w k_w}{\gamma} \\ \dfrac{\gamma k_\beta \epsilon_N}{2\pi\left[1 + a_w^2\right]} & k_\beta > \dfrac{a_w k_w}{\gamma} \end{cases} , \qquad [4\text{-}9]$$

where $k_w = 2\pi/\lambda_w$ is the wave number of the wiggler, k_β is the wave number for betatron oscillations resulting from the distributed focusing along the wiggler, and the normalized emittance ϵ_N is defined as $\gamma\pi r\theta$ where r is the radius and θ is the half-angle at any beam focus. The two terms in Equation [4-9] are due to detuning from the resonance condition by the B-field gradient and by the trajectory angle associated with the betatron orbit, respectively. The minimum energy spread occurs for a focusing strength $k_\beta = a_w k_w/\gamma$ which is precisely the natural value for a planar wiggler. In that case the detuning from the resonant condition for each electron is independent of axial position. Electron trapping will be relatively inefficient when the effective energy spread given by Equation [4-9] exceeds the bucket full width. For other focusing strengths, the energy spread given in Equation [4-9] is actually a peak value achieved only at certain points in the betatron orbit. In this case detrapping will occur if the energy spread exceeds the bucket height and the synchrotron wavelength is much shorter than the betatron wavelength. The latter condition is marginally satisfied for the systems of interest. The requirement that the effective energy spread be less than the well depth will hereafter be called the "bucket constraint."

In some cases, the allowable emittance may be limited by the need to maintain spatial overlap in the focusing plane. This occurs when the allowable e-beam radius based on the bucket constraint exceeds the photon beam waist size. The e-beam radius given by the distributed focusing in the wiggler is

$$r_{eb} = \left[\frac{\epsilon_N}{\gamma\pi k_\beta}\right]^{1/2} . \qquad [4\text{-}10]$$

This result is valid when the electrons are optimally focused at the wiggler entrance, in which case the e-beam radius is length independent within the wiggler. As shown later, a reasonable condition for minimal gain degradation at fixed extraction is the requirement that the e-beam radius be less than the 1/e photon intensity radius, that is, $r_{eb} \leq w/2^{1/2}$, where w is the 1/e photon amplitude radius. This requirement leads to an allowable emittance of

$$\epsilon_N \leq \frac{\gamma \lambda_s Z_R k_\beta}{2} \quad . \qquad [4\text{-}11]$$

The requirement to maintain spatial overlap between the electron and photon beams shall be called the "overlap constraint."

In the free-expanding plane, spatial overlap is generally the limiting constraint. Proper overlap may be provided by matching the photon and e-beam envelope shapes, leading to the requirement

$$\epsilon_N \leq \frac{\gamma \lambda_s}{2} \quad . \qquad [4\text{-}12]$$

Comparison with Equation [4-11] shows that the emittance requirement for overlap is more severe in the free-expanding plane for those systems which have $Z_R k_\beta$ greater than unity. This constraint may be relaxed if two-plane e-beam focusing is provided as described in Section 2.3.

4.1.4 Confirmation of Emittance and Energy Spread Requirements

Equations [4-5], [4-9], [4-11], and [4-12] define energy spread and emittance requirements. The actual degradation in FEL interaction strength for energy spread and emittance values which approaches these limits is computed in this section. Electrons which are detuned to near the edge of the bucket or experience lower E-fields due to off-axis trajectories experience a somewhat weaker interaction.

These effects may be quantified by numerical integration of the equations for electron energy loss and electron phase in the ponderomotive potential of the FEL interaction.

$$\frac{d\gamma}{dz} = \frac{-e_s a_w \sin(\psi-\phi)}{\gamma} \qquad [4\text{-}13]$$

$$\frac{d\psi}{dz} = k_w - \frac{k_s}{2\gamma^2}\left[1 + a_w^2 + \gamma^2\left[\theta_x^2 + \theta_y^2\right]\right] .$$

The effects of emittance are included in a two-step process. First the transverse angles θ_x and θ_y of the electron orbits, the optical E-fields, and the wiggler B-fields experienced by each electron are computed as a function of axial position, including the off-axis motion but ignoring the small effect of the FEL interaction on the trajectory. Then the energy loss is determined in a one-dimensional integration of the coupled Equations [4-13] using the previously computed angles and E and B-fields for each electron. The emittance phase space is assumed to be uniformly filled. The electron and optical beams are assumed to be optimally focused and coaligned and the optical beam is assumed to be diffraction-limited, in which case, in the low-gain approximation, the E-field amplitude and phase varies spatially according to[4-9]

$$e_s(r,z) = e_s^o \left[\frac{w_o}{w[z]}\right] e^{-(r/w[z])^2} \qquad [4\text{-}14]$$

$$\phi(r,z) = \tan^{-1}\left[z/Z_R\right] - \left[\frac{r}{w[z]}\right]^2 \left[z/Z_R\right] ,$$

where e_s^o is the normalized on-axis E-field at the waist, $w(z) = w_o\,(1 + [z/Z_R]^2)^{1/2}$, w_o is the 1/e photon amplitude radius at the waist, and z is measured from the waist location. The spatial B-field variation is included by assuming constant k_w with a_w tapered for constant resonant phase

$$a_w(y,z) = a_w^0\, \zeta\, \cosh k_w y , \qquad [4\text{-}15]$$

where

$$\zeta(z) = 1 - \frac{\Delta a_w}{a_w^o} \frac{\ln\left[\dfrac{-q + (1+q^2)^{1/2}}{z/Z_R + \left[1 + \left[z/Z_R\right]^2\right]^{1/2}}\right]}{\ln\left[\dfrac{-q + (1+q^2)^{1/2}}{q + (1+q^2)^{1/2}}\right]}, \qquad [4\text{-}16]$$

a_w^o is the a_w value at the entrance, and Δa_w is the change in a_w along the wiggler length.

Numerical calculations have been completed for the 0.5 μm parameters of Section 3.3 at saturated optical intensity. The wiggler design assumes two-plane e-beam focusing as described in Section 2.3. Results of the numerical electron tracking calculations are given in Figure 4-2. Here the extraction is fixed and the effect of emittance is to require an overall higher photon power to achieve a given level of extraction. Since overlap is the more severe emittance constraint (see Section 3.3), the higher photon flux compensates for the relatively low E-fields experienced by most electrons due to their off-axis trajectories. About 50 percent gain degradation is found at the overlap constraint of $r_{eb} = w_o/2^{1/2}$ defined previously. A similar gain degradation factor is obtained for an energy spread which just matches the full bucket height. These results show that the previously defined energy spread and emittance requirements correspond to defining the acceptance as the value which degrades the FEL interaction strength by one-half.

4.2 RESULTS AND DISCUSSION

The optimization analysis developed in the previous section is now used to define the parameters for systems optimized for peak gain at fixed extraction. Energy spread and emittance acceptance values are identified for these systems. Then tradeoffs which lower the gain but enhance acceptance are examined.

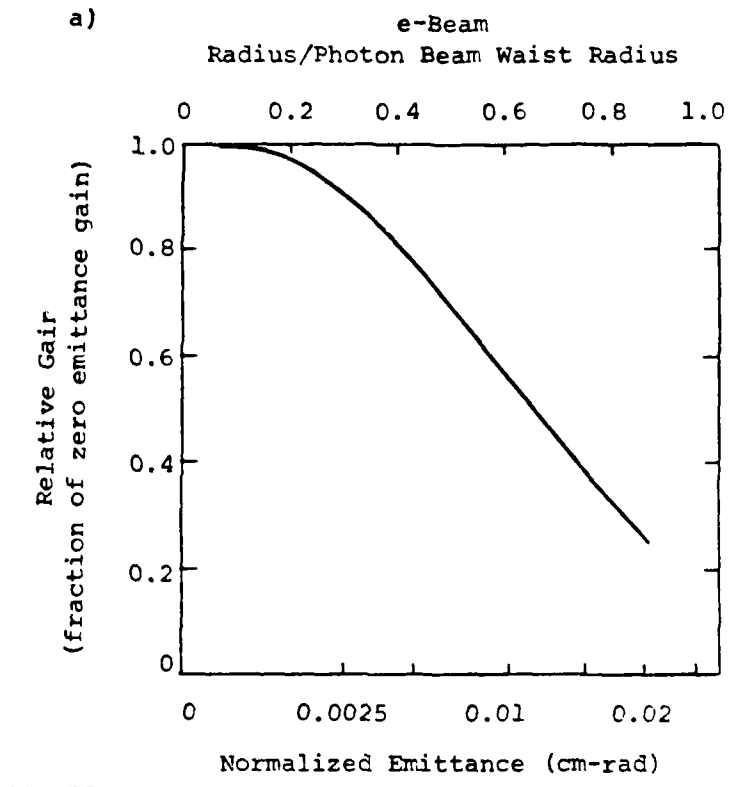

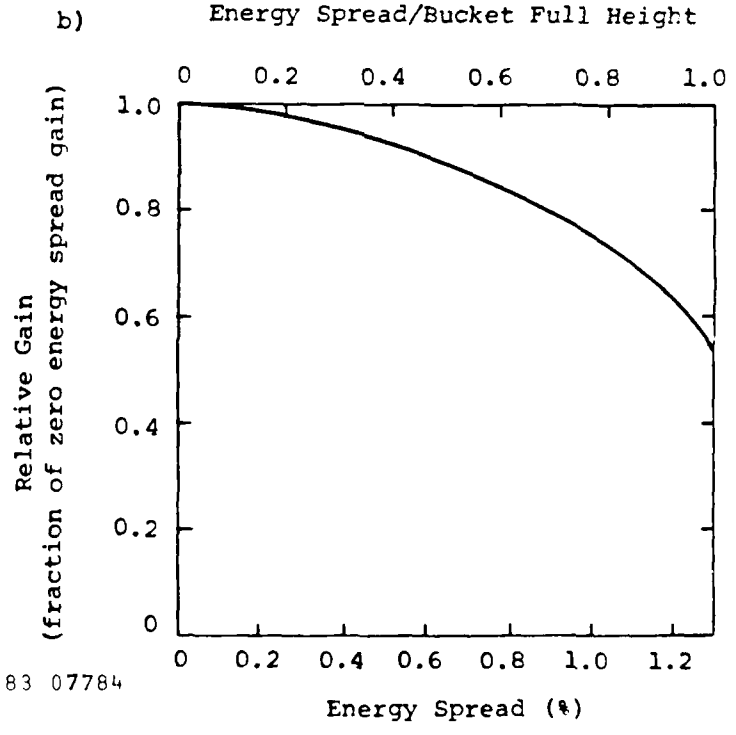

Figure 4-2. Gain Degradation at Fixed Extraction Due to a) Finite Emittance and b) Energy Spread. Assumed Conditions Given in Section 3.3.

4.2.1 Gain-Optimized Systems

The calculated maximum possible gain and corresponding e-beam energy are given in Figure 4-3. The values are calculated assuming zero energy spread and emittance. The gain values are in units of percent optical power increase per ampere of e-beam current. They apply to 5 percent extraction, but can be trivially scaled to other extraction values since the gain-extraction product is constant. Comparison with the numerical tracking code described previously shows that these gains are generally accurate to within 30 percent. The curves clearly indicate that higher gains may be obtained with longer wigglers. This results primarily from the term $ha_w/\lambda_w(1 + a_w^2)$ in Equation [4-2], which increases in value as the bore size h increases. The gain is not a strong function of the photon wavelength. This is due to our assumption of constant current, which means that the weaker interaction at shorter wavelengths is partially offset by the larger e-beam power at higher γ values. The associated optical powers, P_s, for 5 percent extraction are given in Figure 4-4. These powers can be scaled to extraction values, η, other than 5 percent by noting that η^2/P_s is constant.

Optimum values of the dependent parameters for the 1 micron photon wavelength case are shown in Figure 4-5. Parameters L_w/Z_R and a_w remain roughly constant while the ratio h/λ_w varies significantly with wiggler length. It is interesting to note that the optimum a_w value is less than unity for the conditions examined and for this particular choice of the independent parameters. An optimum a_w value of 1.0 is frequently reported in the FEL literature, and the latter value does result from this optimization when λ_w is taken to be independent (i.e., fixed). Certainly one can pick λ_w to be a system constraint if so desired, but equivalent wiggler performance will then require slightly longer wigglers than for the case where L_w is constrained and λ_w is optimized.

Calculated values of the energy spread requirements for gain-optimized systems are shown in Figure 4-6. These curves apply to the 5

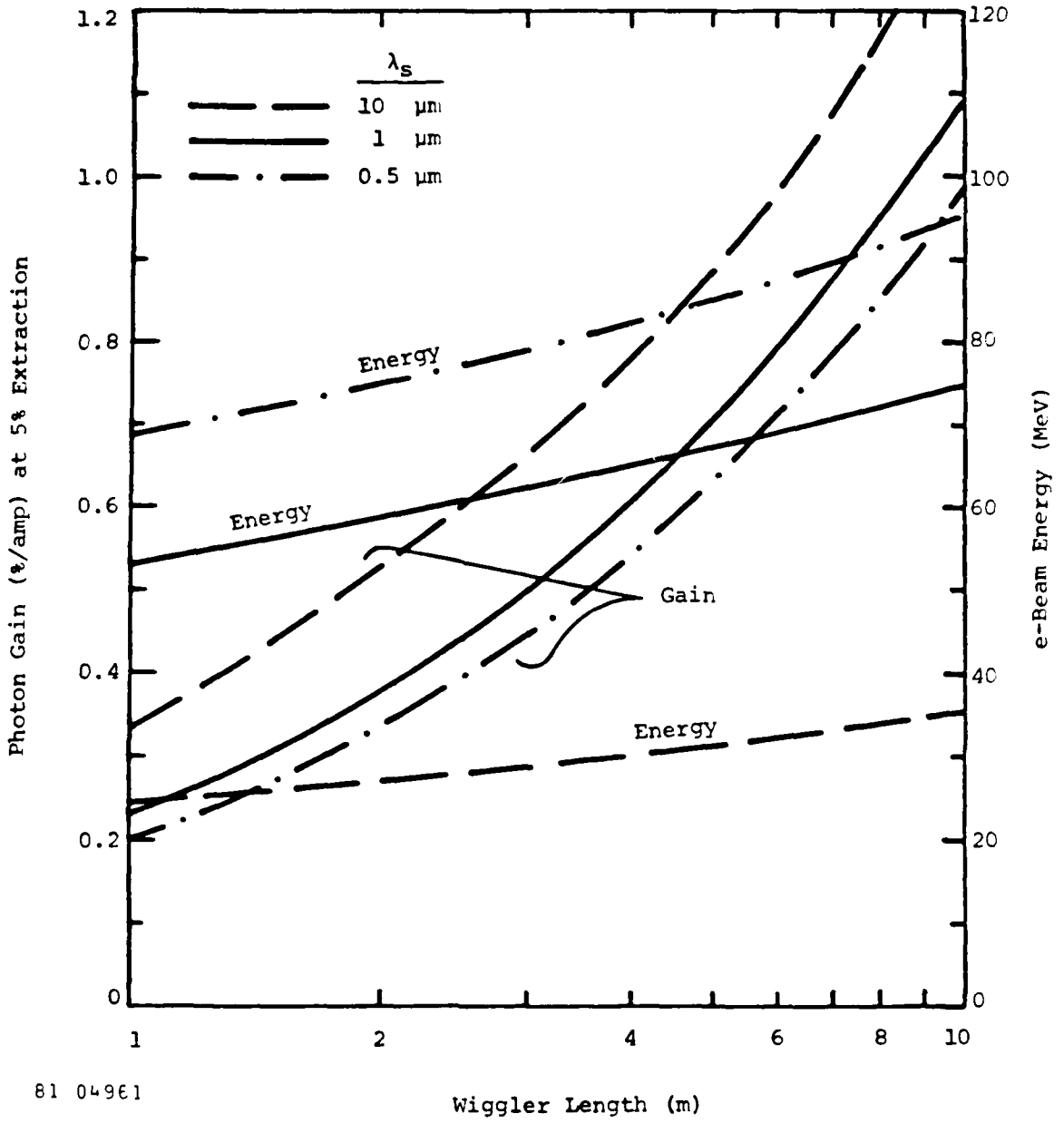

Figure 4-3. Maximum Single-Pass Gain and Optimum e-beam Energy.

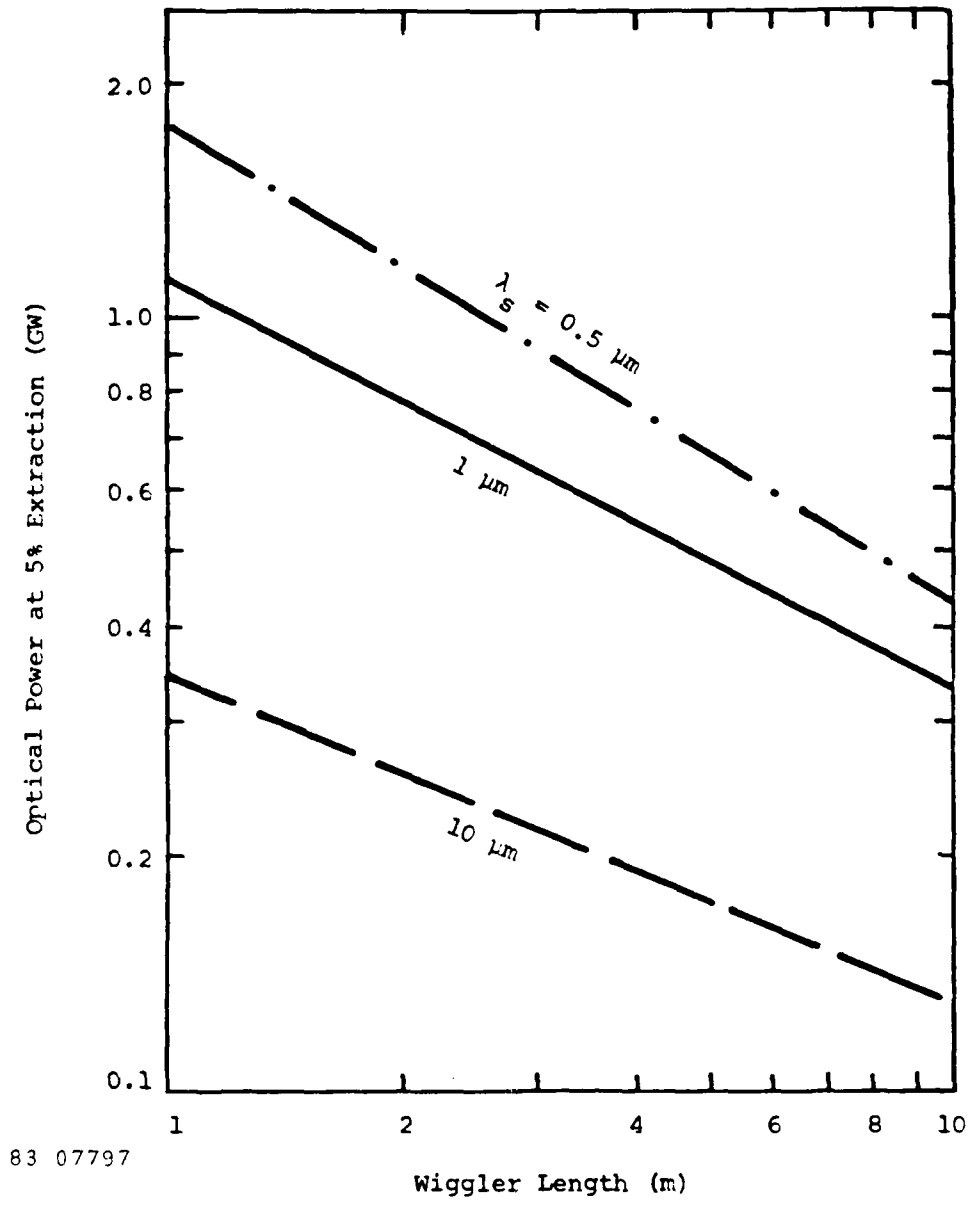

Figure 4-4. Optical Power Under Peak Gain Conditions.

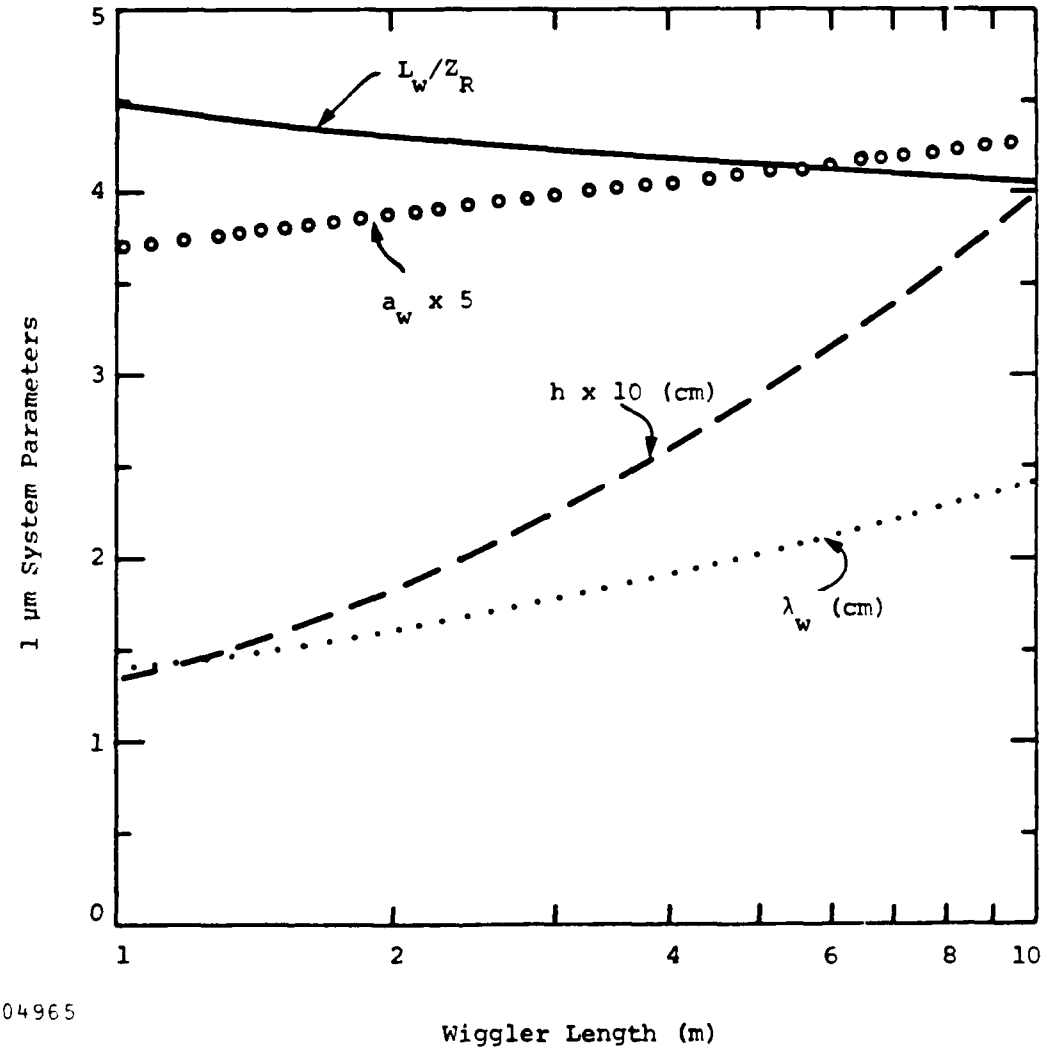

Figure 4-5. Optimum Wiggler Parameters for Maximum Gain at λ_s = 1 μm.

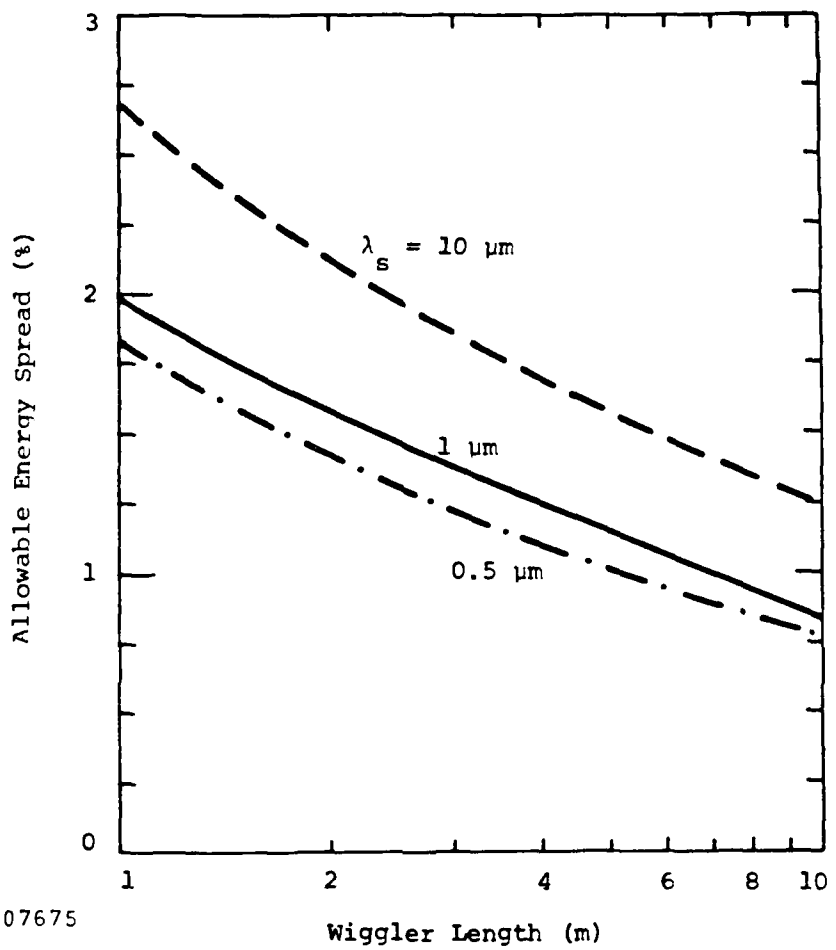

Figure 4-6. Energy Spread Requirement at Optimum Gain Conditions and 5 Percent Extraction Based on Equating Maximum Energy Spread to Bucket Height.

percent extraction case, but may be scaled to other values by noting that the bucket height varies proportional to $\eta^{1/2}$. The bucket depth dependence on photon wavelength is weak because the $\lambda_s e_s$ product in Equation [4-5] does not vary substantially. These bucket widths have been calculated for the field at the entrance or exit of the wiggler. From the L_w/Z_R values of Figure 4-5, the bucket at the wiggler center is typically 50 percent larger.

The emittance values which just fill the bucket and which just meet the overlap requirement are shown in Figure 4-7. Clearly the emittance requirement for overlap is the more severe constraint and becomes particularly serious at shorter photon wavelengths. This constraint may be relaxed somewhat if e-beam focusing is provided in the nominally free-expanding plane.

4.2.2 Two-Plane e-Beam Focusing

The allowable emittance for gain optimized systems with equal two-plane focusing is shown in Figure 4-8. As with single-plane focusing, the allowed emittance is generally limited by spatial overlap constraints. For short wiggler lengths, the overlap obtained with two-plane focusing and an axially independent beam size is worse than the overlap which can be achieved with no wiggler focus and a slightly converging input beam. In this case the emittance requirement shown is identical to that in Figure 4-7 for single-plane focusing. For λ_s = 10 μm, the allowed emittance is limited by the bucket constraint for wiggler lengths greater than 8 meters. For the longer wiggler lengths, the emittance acceptance is considerably enhanced relative to the single-plane focusing case. Since the actual improvement in useful current scales as ϵ^2, two-plane focusing represents a significant advantage.

The overlap problem may be further affected by additional external focusing along the wiggler length. Such additional focusing may be useful whenever the natural focus of the wiggler produces an effective energy

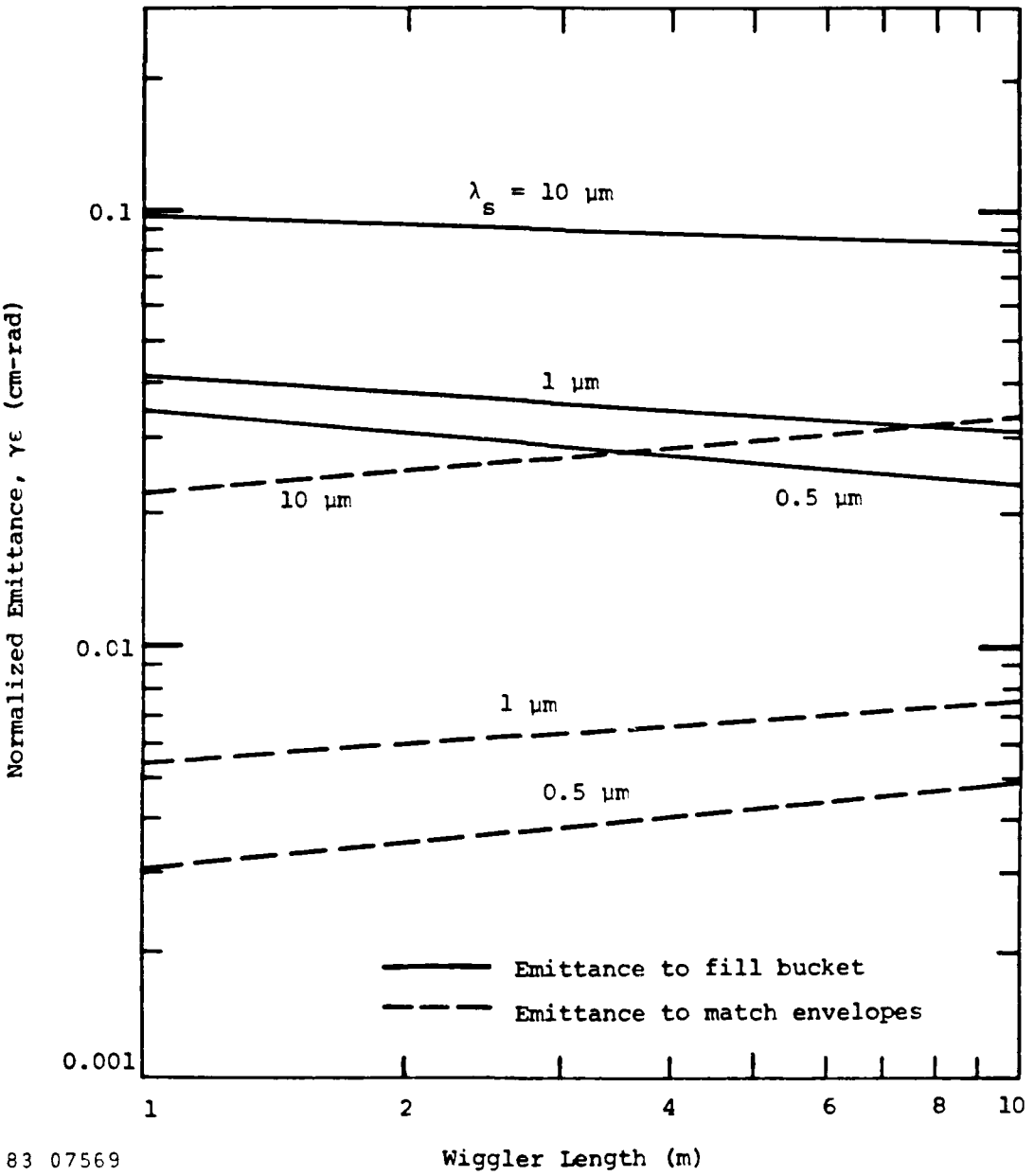

Figure 4-7. Normalized Emittance to Fill Bucket in Focusing Plane and for Spatial Overlap in Free-Expanding Plane.

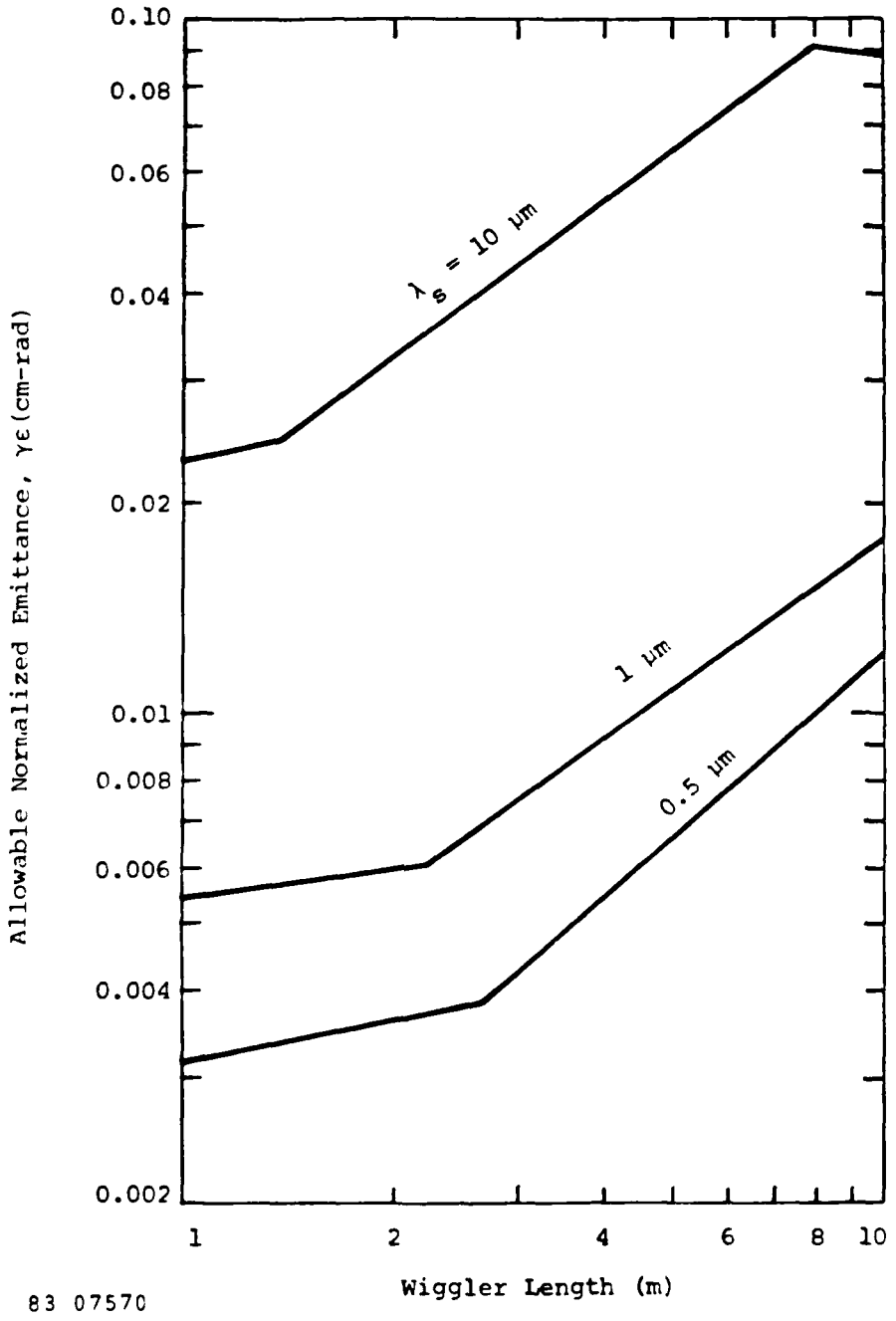

Figure 4-8. Emittance Acceptance of Gain-Optimized Systems with Equal Two-Plane Focusing Provided by Wiggler. Bucket Constraint Based on 5 Percent Extraction.

spread that does not exceed the bucket depth. In Figure 4–9, the emittance requirements based on the bucket (Equation [4–9]) and overlap (Equation [4–11]) constraints are shown as a function of focusing strength by the dashed and solid lines, respectively. This example case has λ_s = 0.5 μm, 5 percent extraction, and L_w = 5 m. Since the emittance acceptance of the wiggler is the minimum of the two constraints, the optimum operating point is expected to be at their intersection. Strong external focusing appears to provide a promising means of emittance acceptance enhancement.

4.2.3 Optimization for High Emittance

In the previous section systems were optimized for highest gain under the assumption of zero emittance, and the emittance acceptance was then computed. For nonzero emittance values, the wiggler parameters specified do not provide the highest possible gain. An optimization for larger emittance values is now considered for systems with equal two-plane focusing provided by the wiggler. For simplicity the analysis is tailored to cases where the equivalent energy spread due to emittance is unimportant, as is the case for the following 0.5 μm calculations.

The function to be optimized is equivalent to that considered previously (Equation [4–1]), except that new factors are added to reflect the degradation of gain at fixed extraction with increasing emittance and energy spread. For a given fractional energy spread $\Delta E = \Delta\gamma/\gamma$ and emittance ϵ_N, these factors depend on the other system parameters and are given by

$$f_{\Delta E} = \begin{cases} 1 - \frac{1}{2}\left[\frac{\Delta E}{H}\right]^2 & \frac{\Delta E}{H} < \left[\frac{2}{3}\right]^{1/2} \\ \left[\frac{2}{3}\right]^{3/2}\left[\frac{\Delta E}{H}\right]^{-1} & \frac{\Delta E}{H} > \left[\frac{2}{3}\right]^{1/2} \end{cases} \qquad [4\text{–}17]$$

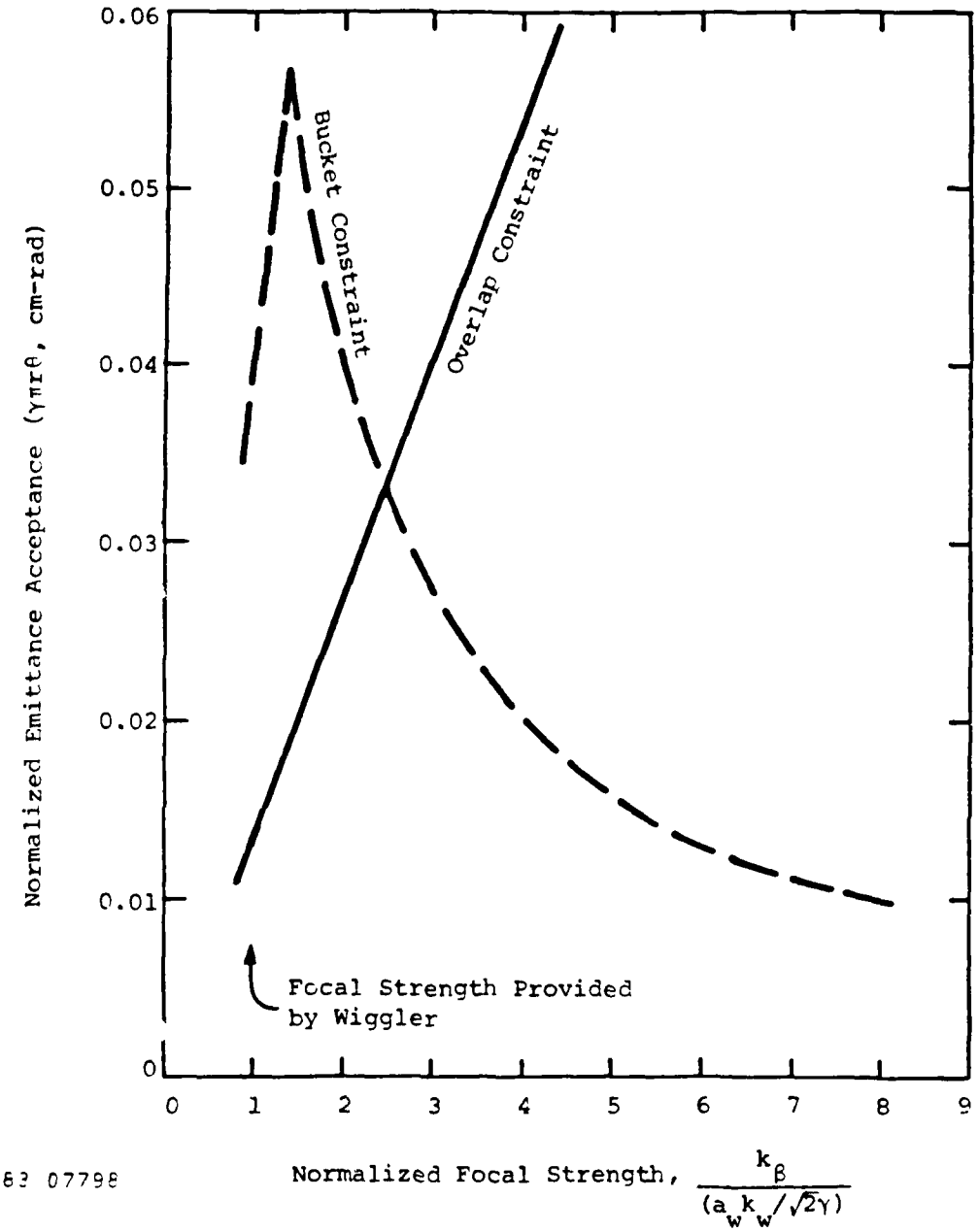

Figure 4-9. Emittance Acceptance for Various Levels of Equal Two-Plane Focusing. Bucket and Overlap Constraints as Defined in Section 4.1.3. Assumed Wiggler Parameters Given in Section 3.3.

$$f_\epsilon = \begin{cases} 1 - \frac{1}{2}\left[\frac{\epsilon_N}{\epsilon_o}\right] & \frac{\epsilon_N}{\epsilon_o} < \frac{4}{3} \\ \frac{16}{27}\left[\frac{\epsilon_N}{\epsilon_o}\right]^{-2} & \frac{\epsilon_N}{\epsilon_o} > \frac{4}{3} \end{cases} \qquad [4\text{-}18]$$

where H is the bucket height defined by Equation [4-5] and ϵ_o is the normalized emittance acceptance based on the overlap constraint given in Equation [4-11]. The functional dependences for lower energy spread and emittance values ($\Delta E/H < (2/3)^{1/2}$, $\epsilon_N/\epsilon_o < 4/3$) are fits to the numerical results shown in Figure 4-2. For large energy spread ($\Delta E/H > (2/3)^{1/2}$), the fraction of electrons in the bucket is proportional to $1/\Delta E$, and the proportionality constant is chosen to connect smoothly to the curve in Figure 4-2(b). This scaling properly refers to cases where energy spread in excess of $(2/3)^{1/2}$ H is filtered out upstream of the wiggler. For large emittance ($\epsilon_N/\epsilon_o > 4/3$) the fraction of electrons within the optical beam is proportional to ϵ_N^{-2}, and the proportionality constant is chosen to connect smoothly to the curve in Figure 4-2(a).

The new function to be optimized is then

$$\xi = \frac{128\pi^2 e}{mc^2}\,(\delta \sin\Psi)^2\,\gamma I \chi^2 f_{\Delta E} f_\epsilon \,. \qquad [4\text{-}19]$$

As before, this is an expression for the gain at fixed extraction. The two additional parameters ΔE and ϵ_N are taken to be fixed, while, as before, λ_w, h, and Z_R are varied to find the optimum. The results of this analysis for $\lambda_s = 0.5$ μm are shown in Figure 4-10. For wiggler lengths over 4 meters, the system parameters adjust to accept normalized emittance values of up to 0.01 cm-rad with no more than 50 percent gain loss. Energy spreads of up to 1 percent result in no more than 50 percent gain loss for wiggler lengths of under 7 meters. Intermediate wiggler lengths of 4 to 7 meters are least sensitive to the combined effects of emittance and energy spread.

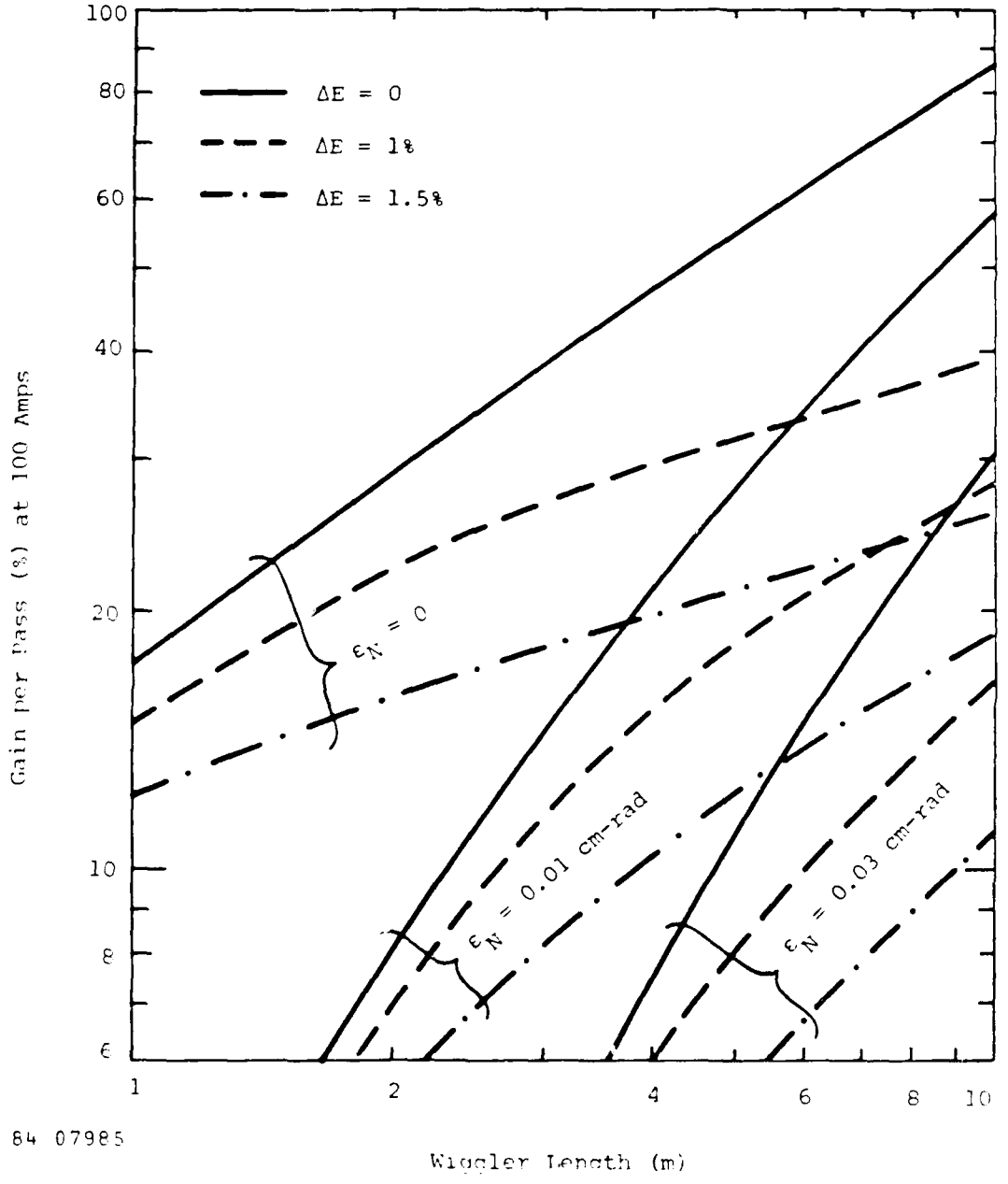

Figure 4-10. Maximum Gain at λ_S = 0.5 μm and 5 Percent Extraction for Various Assumed Levels of Emittance and Energy Spread.

Figure 4-11 shows how system parameters change to accept larger emittance. To provide proper overlap as the emittance is increased, the photon beam size must be increased beyond the optimal zero-emittance size. In addition, the e-beam energy is increased because the equivalent energy spread decreases with γ. The photon beam size increase causes gain loss in two ways. First the total photon power increases proportionally to the beam area so that less energy is extracted per unit photon energy invested. Second, the wiggler bore size must also increase, thereby reducing the B-field amplitude and the interaction strength. We note that the magnet gap actually decreases at first as the photon radius increases. This is because the gap is a fixed multiple of the photon beam size at the wiggler ends, and as L_w/Z_R moves from the optimum value of about 4 to smaller values, the end size decreases to a minimum value when the wiggler is confocal ($L_w = 2Z_R$). Not surprisingly, the curves show roughly that the emittance acceptance can be improved fourfold by doubling the photon beam radius at the expense of a factor of 2 gain loss. This benefit to cost ratio becomes less favorable for further increases in the photon beam radius and magnet gap.

It is of interest to compare the falloff in gain with emittance for various wiggler designs. The approximate falloff with increasing emittance is given directly by Equation [4-18]. Figure 4-12 compares a set of these rolloff curves for various 5 meter wiggler designs operating at 0.5 μm and 5 percent extraction. These wigglers differ in gap and magnetic field wavelength so as to provide different emittance acceptance values. It is evident in the figure that over the range shown the gain at zero emittance is falling in rough proportion to the square root of the increase in emittance acceptance, assuming the acceptance is defined as the point at which the gain falls by one-half.

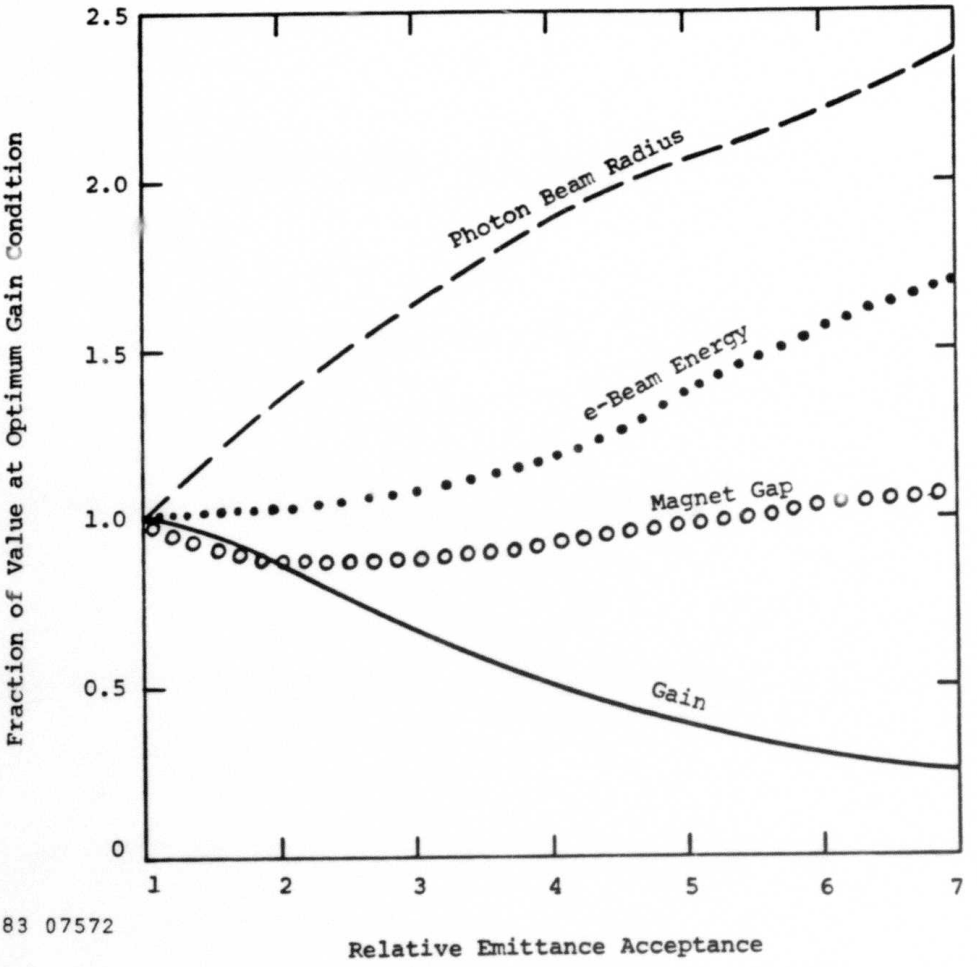

Figure 4-11. Variation of System Parameters to Accept Larger Emittance While Maintaining as High a Gain as Possible. L_w = 5 m, λ_s = 0.5 μm, 5 Percent Extraction, ΔE = 0.

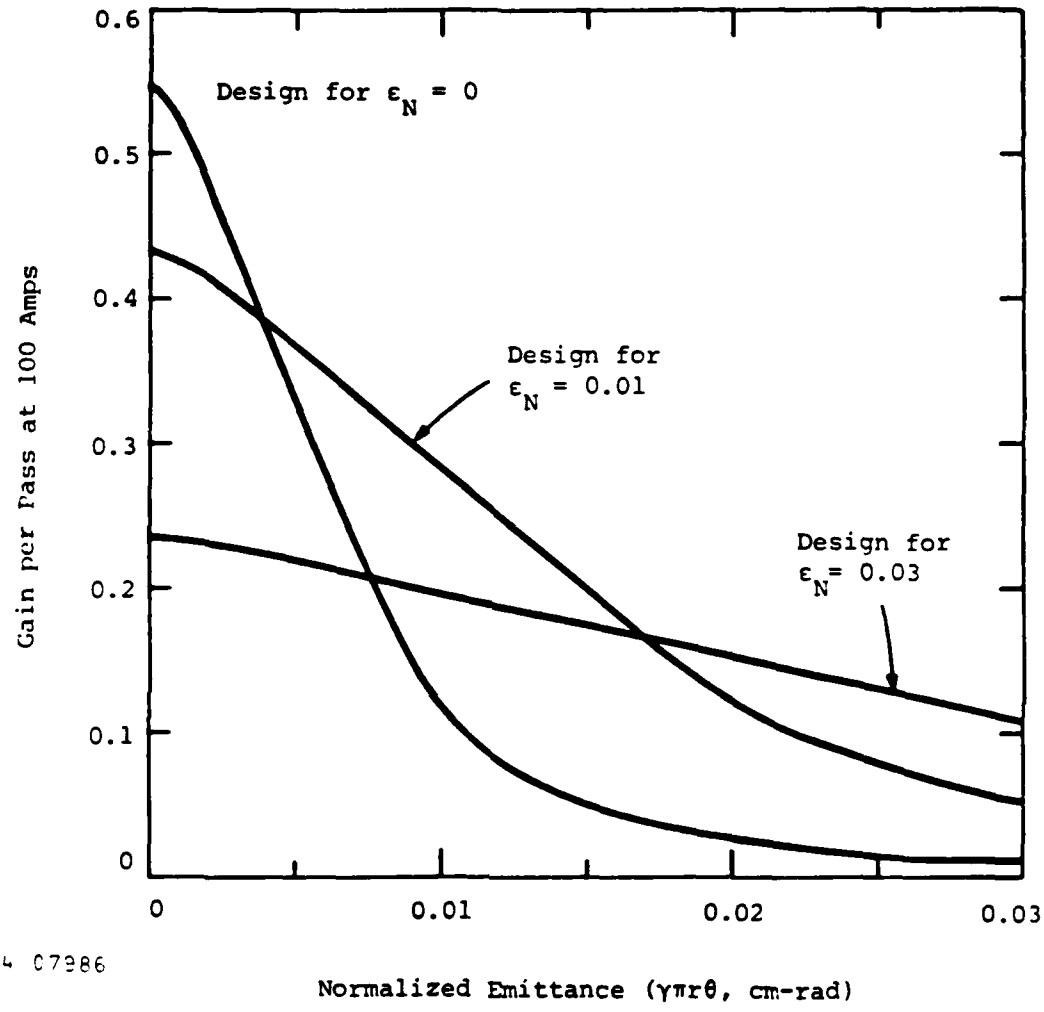

Figure 4-12. Gain Versus Emittance for Systems Optimized for Various Levels of Emittance. L_w = 5m, λ_s = 0.5 μm, 5 Percent Extraction, ΔE = 0.

4.3 IMPLICATIONS

New subharmonic bunching linac injectors recently developed at the Boeing Aerospace Company (BAC)[4-10] and at the Stanford Linear Collider (SLC)[4-11] have each demonstrated simultaneous achievement of high peak current (>100A) and low normalized emittance (<0.02 cm-rad). These achievements can be compared to the well-known Lawson-Penner relation[4-1 to 4-3,4-12]

$$\langle I \rangle \text{ [kA]} = \epsilon_N^2 \text{ [cm-rad]} , \qquad [4-20]$$

which is observed to approximately represent the relationship between the time-averaged current ‹I› and the normalized emittance of a wide range of accelerators working at average currents from milliamperes to kiloamperes. RF accelerators generally produce some degree of bunching while the electrons are at relatively low energy, so the peak and average current values differ. The microscopic duty cycle of the high peak current injectors mentioned previously is made especially small (<0.01) through the use of subharmonic bunching, yielding high peak currents with comparatively low emittance.

The implications of this accelerator technology development on FEL performance is summarized in Figure 4-13. Here the single-pass gain at 5 percent extraction is plotted as a function of peak current and normalized emittance for the preliminary point design of a visible oscillator given in Section 3.3. That design was optimized for the BAC accelerator, and as shown in the figure, about 20 percent single-pass gain is possible at 5 percent extraction. Included for comparison are the SLC accelerator and the Stanford superconducting linac,[4-13] which was used for the first FEL experiment.[4-14] All three accelerators are characterized by roughly the same current densities in emittance phase space, (I_p/ϵ_n^2), although the peak currents differ by two orders of magnitude. State-of-the-art high peak current RF linacs appear to satisfy the e-beam requirements for a high extraction oscillator at visible wavelengths.

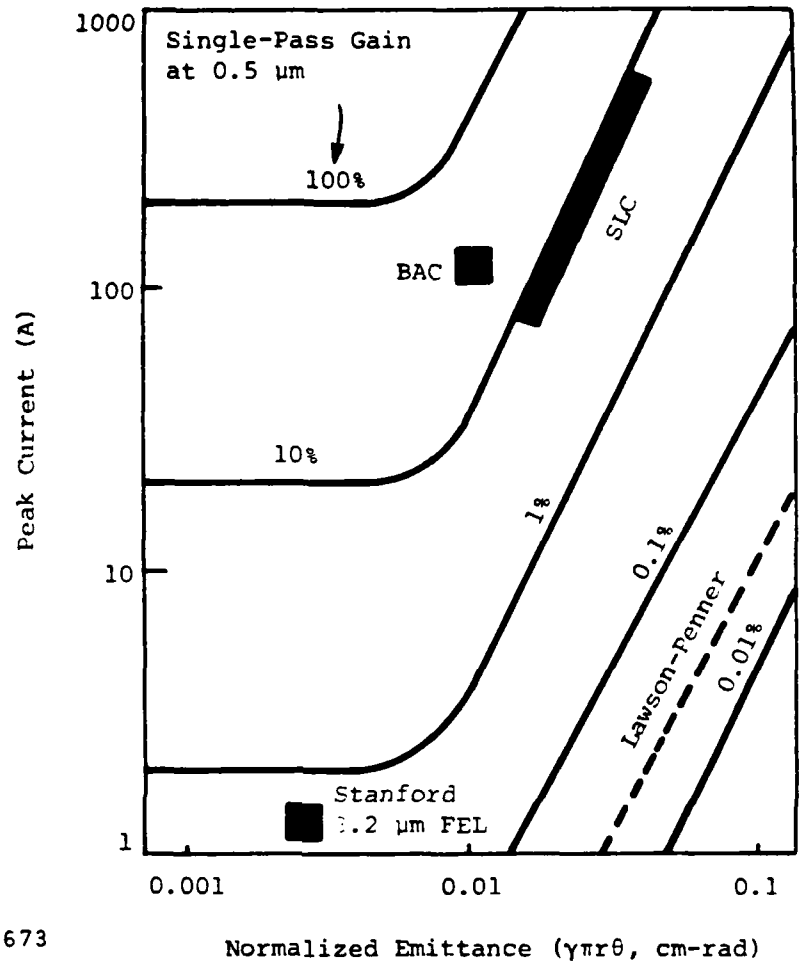

Figure 4-13. **Recent Improvements in Emittance and Peak Current Achieved by Linear Accelerators Improve the Prospects for Visible Oscillation with High Efficiency. Gain Values at 0.5 μm Assume L_w = 5 m and 5 Percent Extraction.**

REFERENCES

4-1. T.I. Smith and J.M.J. Madey, "Realizable Free-Electron Lasers," Appl. Phys. B. 27, 195 (1982).

4-2. G. Dattoli, T. Letardi, J.M.J. Madey, and A. Renieri, "Lawson-Penner Limit and Single Passage Free Electron Lasers Performances," submitted for publication in IEEE J. Quantum Electron.

4-3. J.M.J. Madey, "Application of Transverse Gradient Wigglers in High Efficiency Storage Ring FELs," in the Proceedings of the Bendor Free-Electron Laser Conference, J. de Physique 44, C1-169 (1983).

4-4. J.M. Slater, "Tapered-Wiggler Free-Electron Laser Optimization," IEEE J. Quantum Electron. QE-17, 1476 (1981).

4-5. N.M. Kroll, P.L. Morton, and M.N. Rosenbluth, "Variable Parameter Free-Electron Laser," Physics of Quantum Electronics, Vol. 7, p. 89 (1980).

4-6. K. Halbach, "Permanent Magnet Undulators," in the Proceedings of the Bendor Free-Electron Laser Conference, J. de Physique 44, C1-211 (1983).

4-7. C.A. Brau, "Small-Signal Gain of Free-Electron Lasers with Nonuniform Wigglers," IEEE J. Quantum Electron. QE-16, 335 (1980).

4-8. J.P. Blewett and R. Chasman, "Orbits and Fields in the Helical Wiggler," J. Appl. Phys. 48, 2692 (1977).

4-9. A.E. Siegman, An Introduction to Lasers and Masers, McGraw-Hill, New York 1971.

4-10. J.L. Adamski, W.J. Gallagher, R.C. Kennedy, D.R. Shoffstall, E.L. Tyson, and A.D. Yeremian, "Accelerator Technology for a High Power Short Wavelength FEL," in Free-Electron Generators of Coherent Radiation, C.A. Brau, S.F. Jacobs, and M.O. Scully, eds., Proc. SPIE, 453, p. 59 (1984).

4-11. M.B. James, J.E. Clendenin, S.D. Ecklund, R.H. Miller, J.C. Sheppard, C.K. Sinclair, and J. Sodja, "Update on the High Current Injector for the Stanford Linear Collider," SLAC-PUB-3085, presented at the Particle Accelerator Conference, March 21-23, 1983, Santa Fe, New Mexico.

4-12. V.K. Neil, "Emittance and Transport of Electrons in a Free Electron Laser," SRI Report JSR-79-10 (December 1979).

4-13. T.I. Smith, "The Stanford Superconducting Linear Accelerator," Physics of Quantum Electronics, Vol. 8, p. 77 (1982).

4-14. D.A.G. Deacon, L.R. Elias, J.M.J. Madey, G.J. Ramian, H.A. Schwettman, and T.I. Smith, "First Operation of a Free-Electron Laser," Phys. Rev. Lett. 38, 892 (1977).

Section 5

FEL INTERACTION THEORY

It is important to understand the self-consistent electron-photon behavior in tapered-wiggler FEL oscillators. Work carried out earlier[5-1] under joint DARPA and AFOSR sponsorship provided some of the first insight into the transverse mode structure of tapered-wiggler oscillators. During the present contract, this analysis was extended to the near-concentric cavity geometries of interest for high average power FELs, and the analysis was also extended to three dimensions. The 3-D formulation allows evaluation of cavity alignment tolerance including diffractive beam steering at apertures, as well as extension to non-axisymmetric geometries such as ring cavities employing diffractive output scrapers. Emphasis has also been placed on understanding the longitudinal photon mode structure, in order to study the potentially serious Raman sideband instability.[5-2] The instability is predicted to result in a loss of electron trapping efficiency in tapered-wigglers. This study has provided the first simulation of the time-dependent sideband evolution for parameters of a visible long-pulse tapered-wiggler FEL. The model can be used to identify conditions under which the instability is troublesome and to evaluate sideband suppression techniques. These analyses will be highly relevant for interpretation of experimental results as they become available and for guidance of future oscillator design work. All work reported in Section 5 was supported in part by the Air Force Office of Scientific Research.

5.1 TRANSVERSE MODE STRUCTURE

The FEL requires good intracavity transverse optical mode quality to provide a uniform, high photon intensity within the wiggler and thereby maximize the interaction with the electrons. A nearly diffraction limited output beam is also desirable. To this end a physical optics code has been developed to study mode evolution in injected linear cavities. The code

numerically solves Maxwell's equations for cylindrically symmetric geometries. It allows one to follow development of the mode structure of the tapered-wiggler oscillator, starting with an initial injected wave at saturation intensity. This injected wave develops over many round trips of the optical cavity according to the influence of the FEL interaction, diffraction, and interaction with other elements of the optical cavity. The e-beam radius is typically less than that of the photon beam and the size mismatch drives higher order modes in addition to TEM_{00}. Of additional interest is the effect of apertures on the mode structure, especially those associated with the wiggler. E-field truncation at the ends of the wiggler causes mode dependent cavity losses which of course are higher for higher order modes. The truncation also causes mode mixing, which transfers power from low to high order modes. Such clipping is of interest since the minimum wiggler bore consistent with acceptable distortion due to clipping yields the largest FEL interaction.

Evolving phase and amplitude profiles of the optical beam are calculated by direct integration of Maxwell's equations with the electrons providing the driving term. A convenient tool for understanding this evolution is the projection of the optical wave into normal modes of the optical cavity. That is, the fraction of total optical power in any particular cavity mode can be observed as a function of the round trip number. One sees, for example, that a pure TEM_{00} wave injected into the optical cavity at the start of the calculation evolves an appreciable fraction of TEM_{10} mode over the course of several round trips. This mode mixing is caused primarily by the nonuniform gain medium, and to a lesser extent, by the presence of the wiggler entrance and exit apertures.

The mode evolution during the first 35 round trips after TEM_{00} mode injection is shown in Figure 5-1 for three different cavity lengths, each with 10 percent output coupling. Higher order mode content is especially evident in confocal cavities (those with mirror separation equal to the radius of curvature), and concentric cavities (those with mirror separation equal to twice the radius of curvature). These cavities can support

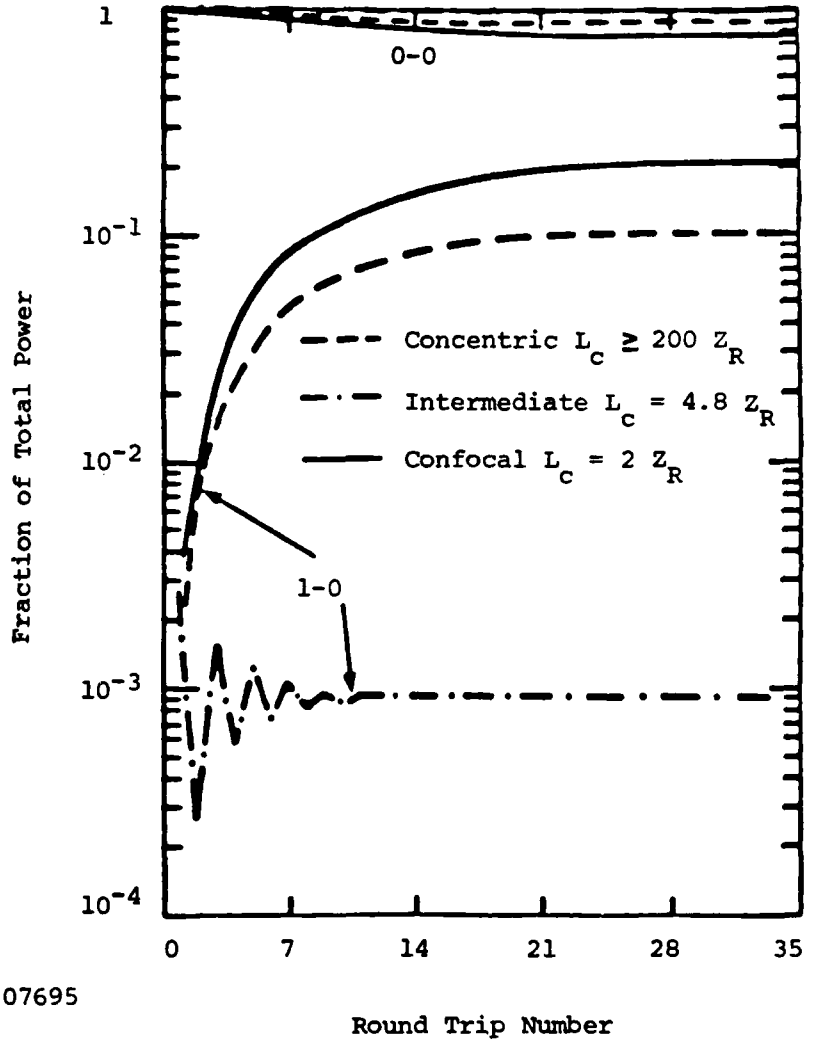

Figure 5-1. Mode Evolution for Various Cavity Lengths and 10 Percent Gain Per Pass.

unusual mode structure because the relative phase slippage between cavity modes over one round trip is an integral multiple of 2π, allowing constructive interference between higher order modes produced on each round trip. As the cavity length is changed away from the confocal or concentric condition without changing the degree of mode selectivity due to aperturing, the fraction of TEM_{00} mode decreases dramatically.

Significant higher order mode content may be found in high gain systems even at intermediate cavity lengths. Systems with high steady-state gain have large output coupling and therefore have a short ri· ·m time. Significant higher order mode content is seen in these syste because higher order modes are damped more quickly than they evolv( ) destructively interfering phases. Plotted in Figure 5-2 is the bou ·i that separates cases in which the TEM_{00} and TEM_{10} modes slip by more than π during the ringdown time, from those which slip by less than π. In the former case, the steady state TEM_{10} content is smaller due to more destructive interference.

Figure 5-3 compares the steady state on-axis intracavity photon intensity with that of the initially injected TEM_{00} mode in the near-concentric cavity. High average power FELs with linear cavities require near-concentric cavities due to mirror loading. The rapid variations in intensity are due to diffractive effects from aperturing at the wiggler ends. The aperture radius is 1.8 w, where w is the 1/e point in E-field for a TEM_{00} wave at the aperture. The TEM_{10} mode content results in the striking asymmetry between the forward and backward moving waves in the wiggler. Such an asymmetry can be supported in the FEL since the gain mechanism is active in one direction only. The presence of the asymmetry leads to enhanced losses in the cavity. For the case shown in Figure 5-3, the round trip power loss at the wiggler apertures is 3.6 percent, which compares to 0.6 percent for a pure TEM_{00} mode. The actual loss is about one-third of the output coupling, representing relatively inefficient energy extraction. The diffractive losses can be reduced by use of an asymmetric cavity such as a ring. In a ring cavity the optical beam needs

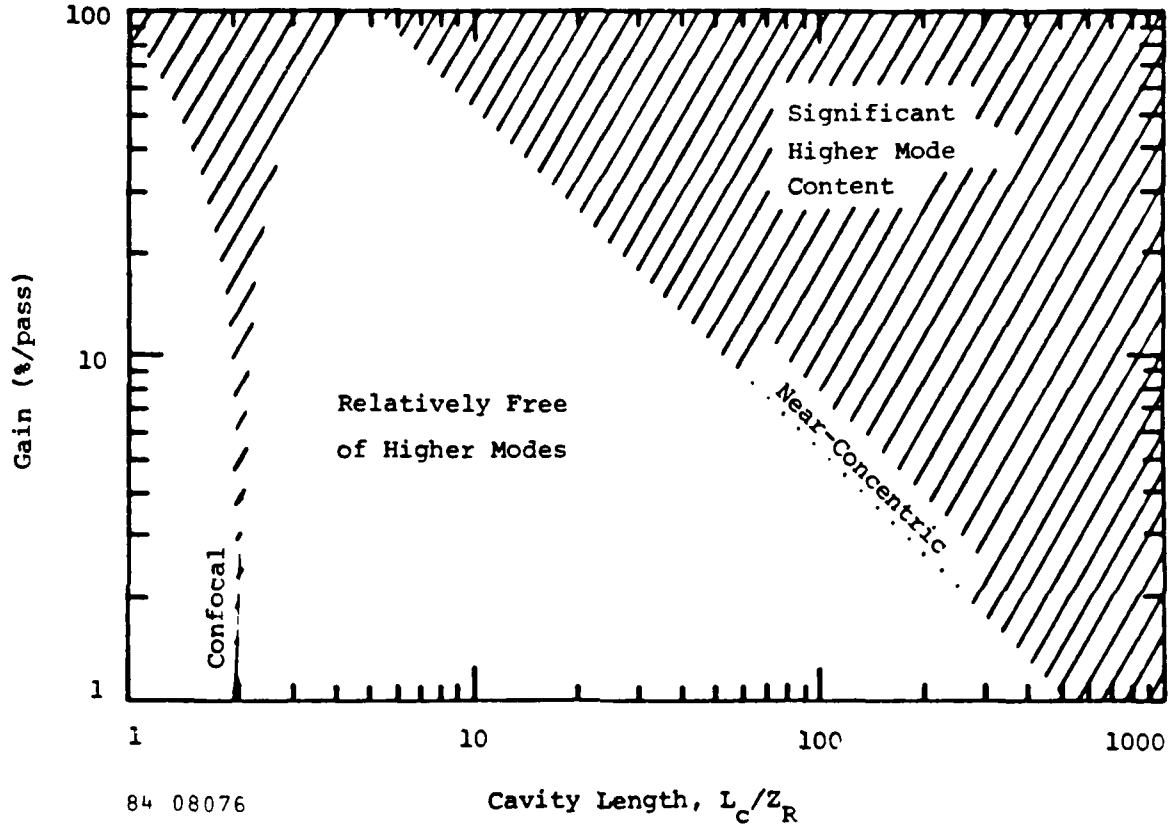

Figure 5-2. Mode Content Depends on Cavity Length and Gain.

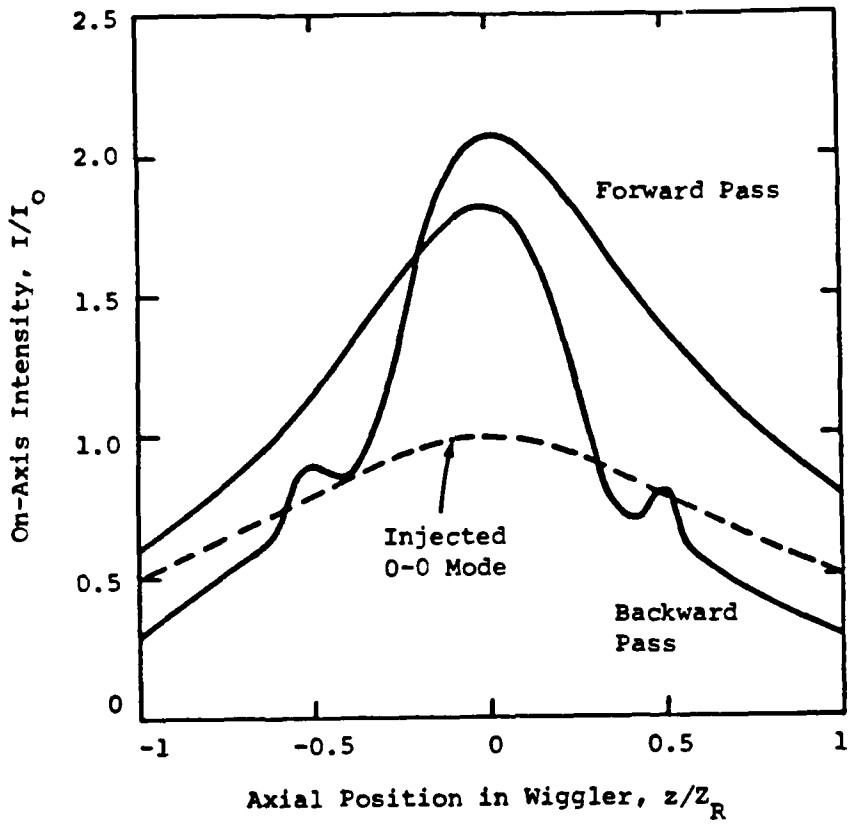

83 07694

Figure 5-3. One-Way Gain Medium Results in Asymmetric Intensity Distribution Within Wiggler of Near-Concentric Cavity with 10 Percent Gain.

to pass through the wiggler aperture only once per round trip and, hence, the wiggler bore need not be sized artificially large to accommodate the beam with minimal loss on both passes.

The quality of the output beam is excellent for each of the cases studied, being of nearly diffraction limited quality. This result is somewhat surprising in view of the TEM_{10} mode content which complicates the intracavity structure, but in reality the higher mode content is an indication of mode mismatch within the cavity, rather than wave front aberration. For the example shown in Figure 5-3, the focused output beam has a Strehl ratio of about 98 percent.

A three-dimensional version of this wave front propagation analysis has been developed and can be used for mode analysis similar to that shown previously, but additional important effects such as misalignment can be included. In addition, the 3-D code provides for analysis of complex cavities such as ring cavities employing glancing incidence mirrors and other non-axisymmetric elements intended for use at high average power. In this program, the 3-D code has been used to analyze mirror alignment tolerances in linear cavities. Initial results of mirror alignment tolerances analysis including diffraction are given in Section 6.2.3. Tolerance to cavity misalignment is generally studied with geometrical optics codes, but long, near-concentric FEL cavities are dominated by diffraction and one finds that the alignment tolerances do not follow conventional rules based on ray tracing.

5.2 SIDEBAND INSTABILITY

The sideband instability was first pointed out and discussed as a potential problem in tapered-wiggler FELs by Kroll and Rosenbluth.[5-2] The sideband instability is characterized by development of longitudinal amplitude and phase modulation in the optical pulse due to the generation of new frequency components or "sidebands" in the laser spectrum. The instability is predicted to become evident only at optical powers high

enough to trap electrons in the ponderomotive potential well of the FEL interaction, because synchrotron oscillations of trapped electrons lead to axial modulation of the gain. In tapered-wigglers, the modulated field can lead to detrapping of electrons from the potential well and, hence, loss of extraction. If detrapping is severe, it may be necessary to add cavity wavelength selectivity to suppress the sideband growth.

The mathematical basis for the sideband instability has been summarized by Goldstein and Colson.[5-3] The electron motion in the ponderomotive well, for small deviations from the resonant phase and an unmodulated E-field, may be described by a harmonic oscillator equation. This implies that such electrons might be expected to couple to light whose wavelength λ_s' is slightly shifted from the original resonant wavelength λ_s:

$$\lambda_s' = \lambda_s \left[1 \pm \frac{\lambda_w}{L_{sy}}\right] , \qquad [5-1]$$

where λ_w is the wiggler wavelength, L_{sy} is the spatial period of the harmonic behavior for an electron near the bottom of the bucket

$$L_{sy} = \lambda_w \left[\frac{\pi \left[1 + a_w^2\right]}{2 \lambda_s a_w e_s \cos \psi_r}\right]^{1/2} , \qquad [5-2]$$

ψ_r is the synchronous phase angle for trapped electrons

$$\psi_r = \sin^{-1} \left[\frac{e_s^*}{e_s}\right] , \qquad [5-3]$$

and the optical electric field E_s and wiggler magnetic field B_o are measured by (cgs units)

$$e_s = \frac{eE_s}{2^{1/2}\, m_o c^2} , \qquad [5\text{-}4]$$

and

$$a_w = \frac{eB_o \lambda_w}{2^{3/2}\, \pi m_o c^2} , \qquad [5\text{-}5]$$

respectively. The quantity e_s^* is the minimum E-field for electron trapping

$$e_s^* = \frac{\gamma_r^2}{a_w L_w} \left[\frac{\Delta\gamma_r}{\gamma_r}\right] \qquad [5\text{-}6]$$

for a wiggler of resonant energy γ_r, fractional energy taper $\Delta\gamma_r/\gamma_r$, and length L_w. In actuality, many electrons undergo large amplitude oscillations, which means that their motion is described by a more complex nonlinear pendulum equation. Such electrons couple to a continuum of light waves of different frequencies close to that given by Equation [5-1]. Kroll's analysis[5-2] predicts a spectrum of unstable waves with the largest growth rates for waves satisfying Equation [5-1] with the positive sign. Thus one expects gain for lower frequency sidebands (longer wavelengths) and absorption for higher frequencies. The spatial modulation period, λ_m, associated with generation of a sideband with wavelength λ_s' is given by

$$\lambda_m = \lambda_s \left[\frac{L_{sy}}{\lambda_w}\right] . \qquad [5\text{-}7]$$

This is to be compared with the slippage distance

$$s = \lambda_s \left[\frac{L_w}{\lambda_w}\right] . \qquad [5\text{-}8]$$

Several different numerical models have been developed[5-4] to treat the time-dependent evolution of the electron and optical pulses in a self-consistent manner. Most simulations of sideband evolution have observed

initial onset of modulation with a period approximately equal to the slippage distance, which corresponds to a synchrotron period comparable to the wiggler length. Evidently sideband growth does not become unstable until the optical power grows to the point where the synchrotron period becomes comparable to or shorter than the wiggler length. The fractional frequency shift of the sideband is then of order 1/N, where N is the number of wiggler periods.

While the original authors[5-2] discussed the instability in the context of long, highly tapered wigglers in which long electron pulses undergo many synchrotron oscillations in passing through the wiggler, most numerical simulation studies have considered short, mildly tapered wigglers in which there is only about one synchrotron period within the wiggler length. Simulations of longer, more highly-tapered wigglers[5-5] have assumed short electron pulses in which the electron pulse length is comparable to or shorter than the distance by which an electron slips back along the optical pulse in one transit through the wiggler. In this work, we consider the evolution of a long optical pulse in a long, highly-tapered wiggler, in which there are three or more synchrotron oscillations in a single pass. Such wigglers can be expected to be subject to somewhat more severe detrapping should sidebands appear, since there is more opportunity for the instability to drive sloshing in the potential well. This is the first study of time-dependent sideband evolution for parameters appropriate for a high-efficiency FEL oscillator operating at visible wavelengths.

Figure 5-4 presents results of an early study to evaluate the possible extraction degradation in long, highly-tapered wigglers, should sidebands appear. This calculation is not self-consistent in that it does not predict the magnitude or wavelength offset of the sidebands. It is simply assumed that a single, well-separated sideband is present at a very modest power level, 4 percent of the power at the carrier frequency. The E-field of the Raman sideband is then 20 percent of the carrier E-field. Figure 5-4 shows the electron energy extraction as a function of the wavelength offset of the sideband, calculated for a single pass through

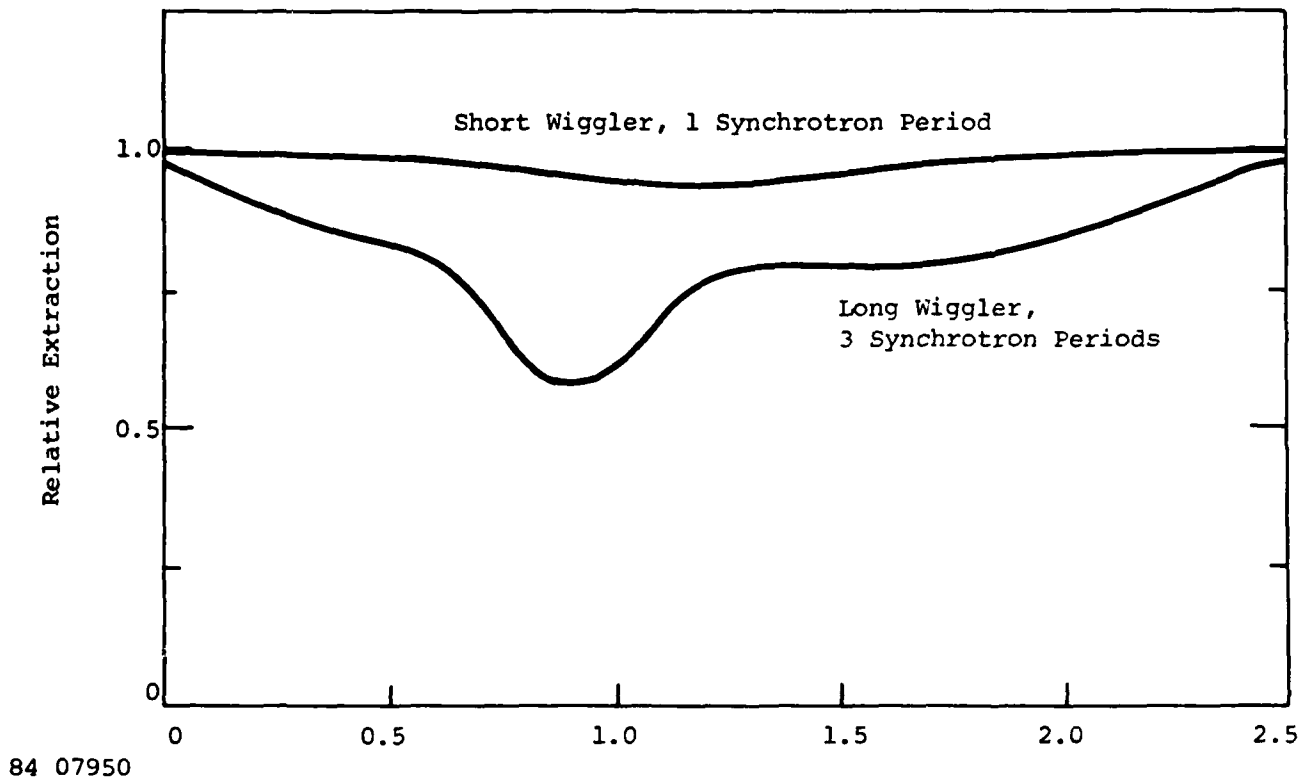

Figure 5-4. Electron Energy Extraction as a Function of Sideband Wavelength for 4 Percent of the Optical Power in a Single, Well Separated Sideband. $\Psi_r = 36°$

each of two wigglers of different length. For the longer wiggler, a very distinct resonance is found, which occurs for a sideband wavelength offset of approximately

$$\frac{\delta\lambda_s}{\lambda_s} = \frac{\lambda_w}{L_{sy}} \quad . \qquad [5\text{-}9]$$

This offset is at a frequency which causes the modulation due to the sideband to be in phase with the synchrotron oscillations of trapped electrons and is in agreement with the predicted sideband offset given in Equation [5-1]. E-field phase modulation due to the sideband results in side-to-side motion of the ponderomotive well. In the longer wiggler, the shaking of the well induces large amplitude sloshing of trapped electrons, causing detrapping and the loss of extraction shown. The conditions assumed for the longer wiggler in this calculation correspond to the preliminary point design of Section 3.3 for a 0.5 μm wiggler.

These calculations give an indication of the possible serious impact of the sideband instability for conditions of a visible-wavelength tapered-wiggler FEL. With as little as 4 percent of the total optical power in the sideband, the extraction could be lowered from the design value of 5 percent to a value of only 3 percent. But these calculations are not self-consistent in that they do not predict the actual frequency offset nor the sideband intensity which will actually occur. (And multiple sidebands may actually be produced.) A truly self-consistent model of the sideband instability must include the effect of the electron dynamics on the optical E-field evolution. Such a model has been developed in this program.

Most previous models of self-consistent sideband evolution[5-4] were designed to model short micropulse experiments in untapered wigglers, such as the initial Stanford FEL oscillator. (The electron pulselength is comparable to the slippage distance in the Stanford experiments.) The codes used may be applied to the long micropulse experiments of interest to DOD goals in which the pulselength is 20 or more slippage distances,[5-6]

but the computer time requirements are very large. We have chosen to examine modulation of long micropulses by use of periodic boundary conditions[5-7] to treat a short section of much longer electron and optical pulses, thus greatly reducing computer time requirements. The modulation of the optical pulse is studied directly in the space-time domain. The choice of the spatial grid size and the width of the window between the periodic boundaries defines the discrete optical frequencies which are handled in the model. Typically the window width is chosen to be several slippage distances long, since the slip length is the longest characteristic distance in the problem.

Results of a calculation of the self-consistent evolution of the optical spectrum in a visible oscillator are shown in Figure 5-5. In this simulation the electron beam is assumed to be of ideal quality, that is, energy spread and emittance are neglected. The power levels shown on the figure refer to the instantaneous power of the optical pulse within the cavity. The simulation is initiated at a power level of approximately 1 watt which is representative of the spontaneous emission power level. To roughly approximate the initial incoherent properties of the E-field, the simulation is seeded with all possible frequencies randomly phased with each other. Use of various representations of the initial spectrum result in somewhat different details in the spectral evolution but do not change the qualitative results. After a number of passes through the oscillator, the laser picks a narrow line from the initial seed. The frequency and shape of the line is consistent with the small-signal gain curve, as shown in the figure. As the power level approaches saturation, the line chirps slightly by growth of the higher wavelength wing of the line. Upon reaching a power level of about 0.7 GW, sufficient to trap electrons, sidebands begin to form. The sideband offset of about 1 percent is consistent with the number of synchrotron periods ("2) at this power level. The sidebands continue to evolve to higher wavelength and the spectrum becomes rather broadband. The laser reaches a quasi-steady state in which it vacillates around an average power of about 1.5 GW. The power oscillations correspond to growth and decay of various spectral features.

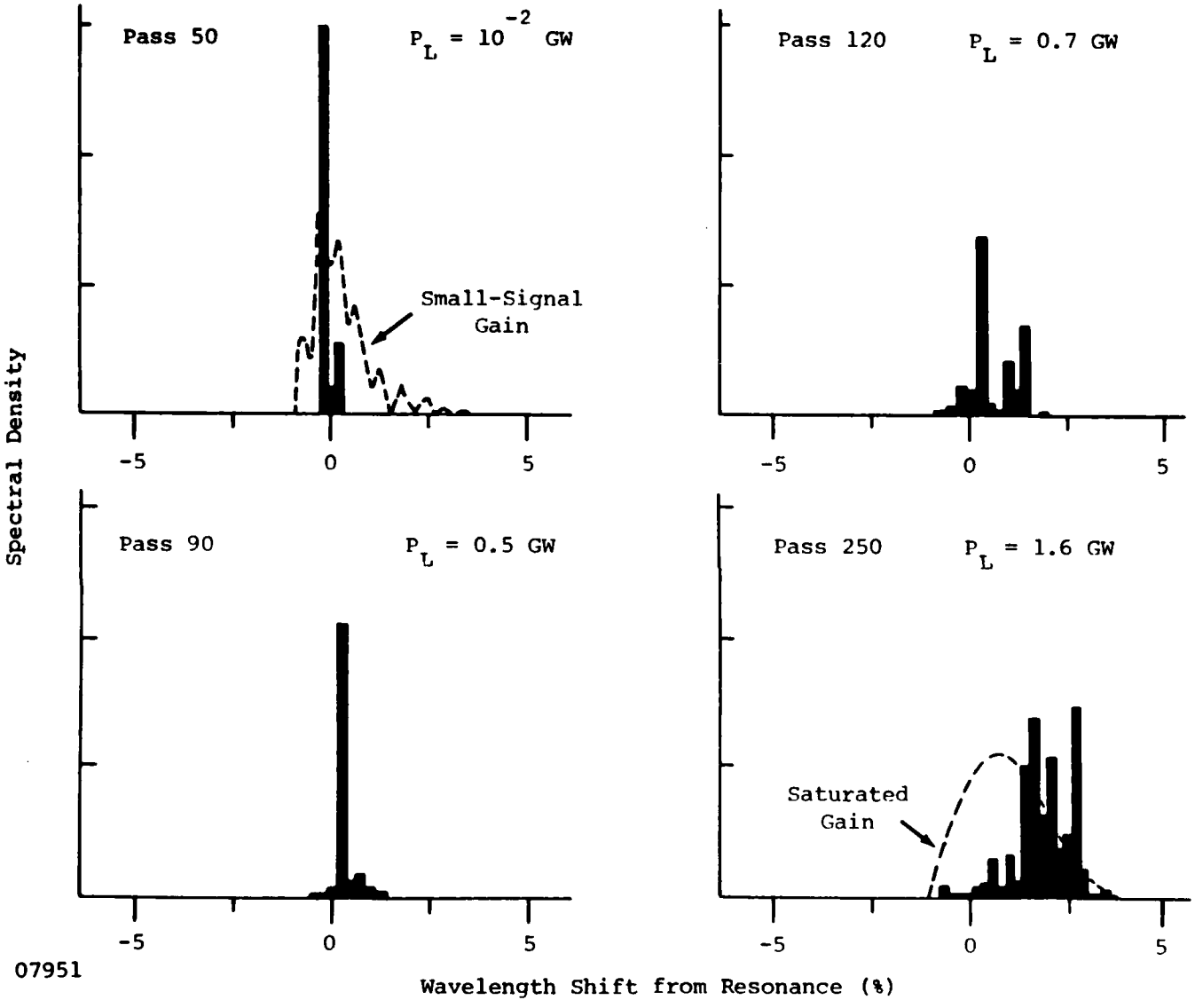

Figure 5-5. Time-Dependent Evolution of Optical Spectrum for Long, Highly Tapered Wiggler. Simulation parameters given in Section 3.3, 15 percent outcoupling.

The extraction efficiency in quasi-steady state averages about 2 percent, considerably lower than the ideal value of about 6 percent which would be obtained if the laser were operating with a narrow line at the frequency of peak gain. As may be seen by comparison with the saturated gain curve shown in the figure, the operating wavelength is not only broadband but at a longer than optimum wavelength.

Figure 5-6 shows how the single pass gain is degraded due to the presence of sidebands. The solid line in the figure is the idealized gain which would be realized for a single narrow line which is allowed to chirp as the optical power grows to saturation. When the self-consistent sideband evolution is included, it is found that the laser saturates at a lower power, and the deleterious effect of the sidebands turns on precisely at the power level which is sufficient to trap the electrons.

The degradation on extraction efficiency due to the sidebands is shown in Figure 5-7. There are a range of output couplings for which the laser will evolve to power levels sufficient for trapping. The ideal extraction efficiency at saturation for operation with a single narrow line which is allowed to chirp is indicated by the solid line. When the effect of the sidebands is included, the extraction is reduced to approximately 40 percent of the expected value.

The model of sideband evolution allows study of sideband suppression techniques. One obvious way to suppress sideband growth is to introduce a dispersive element into the optical cavity. Figure 5-8 shows the result of repeating the calculation shown in Figure 5-5 with a 3 percent full width optical filter in the cavity. This filter function is representative of the reflectivity profile obtainable using multilayer dielectric mirror coatings. The optical spectrum at round trip number 250 is very narrow compared to the case with no frequency selectivity. Furthermore, the spectrum chirps to approximately the wavelength of peak saturated gain, rather than overshooting to longer wavelengths. Consequently, the laser saturates at a much higher power level and the extraction efficiency, as

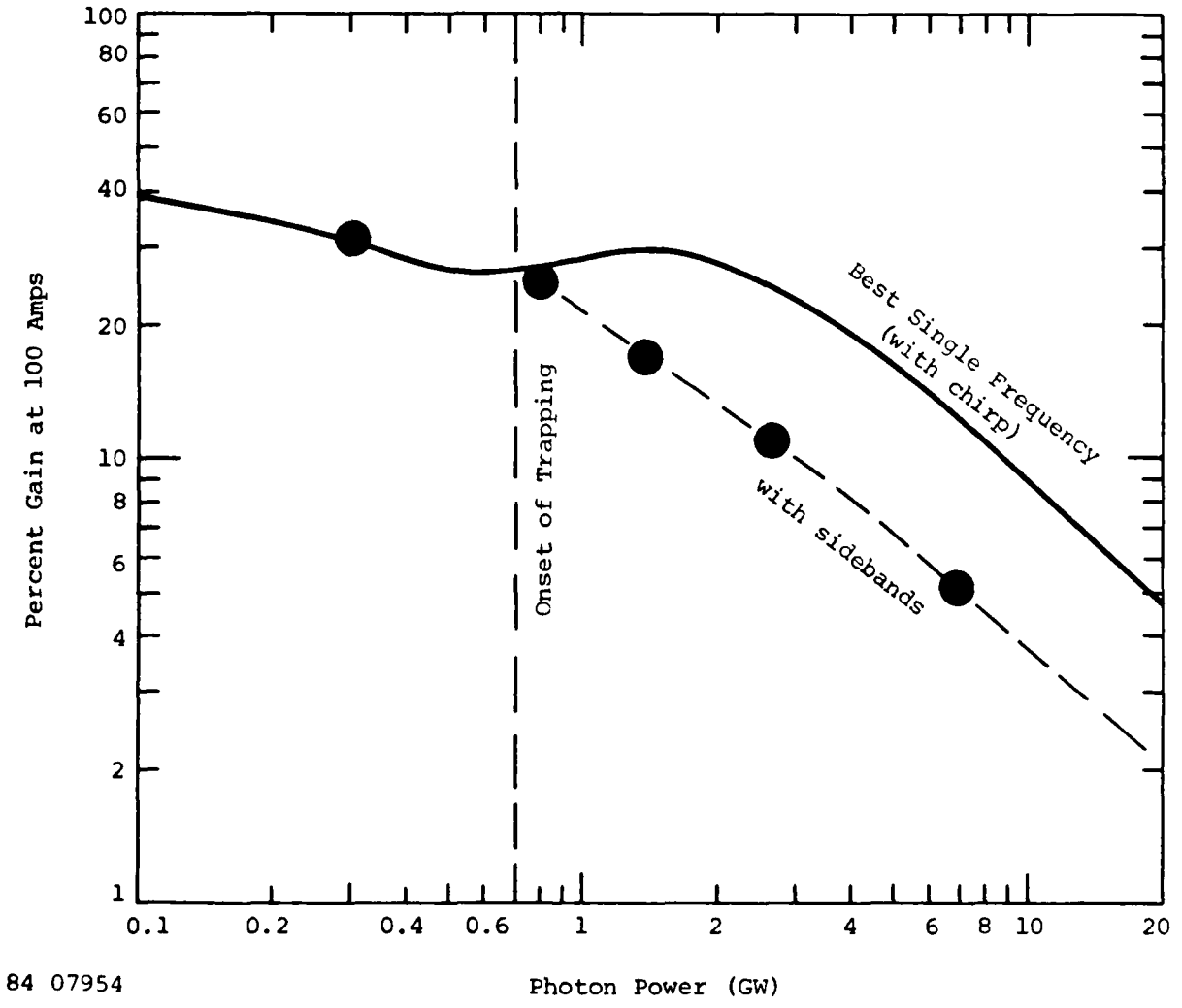

Figure 5-6. Gain Degradation Due to Sidebands.

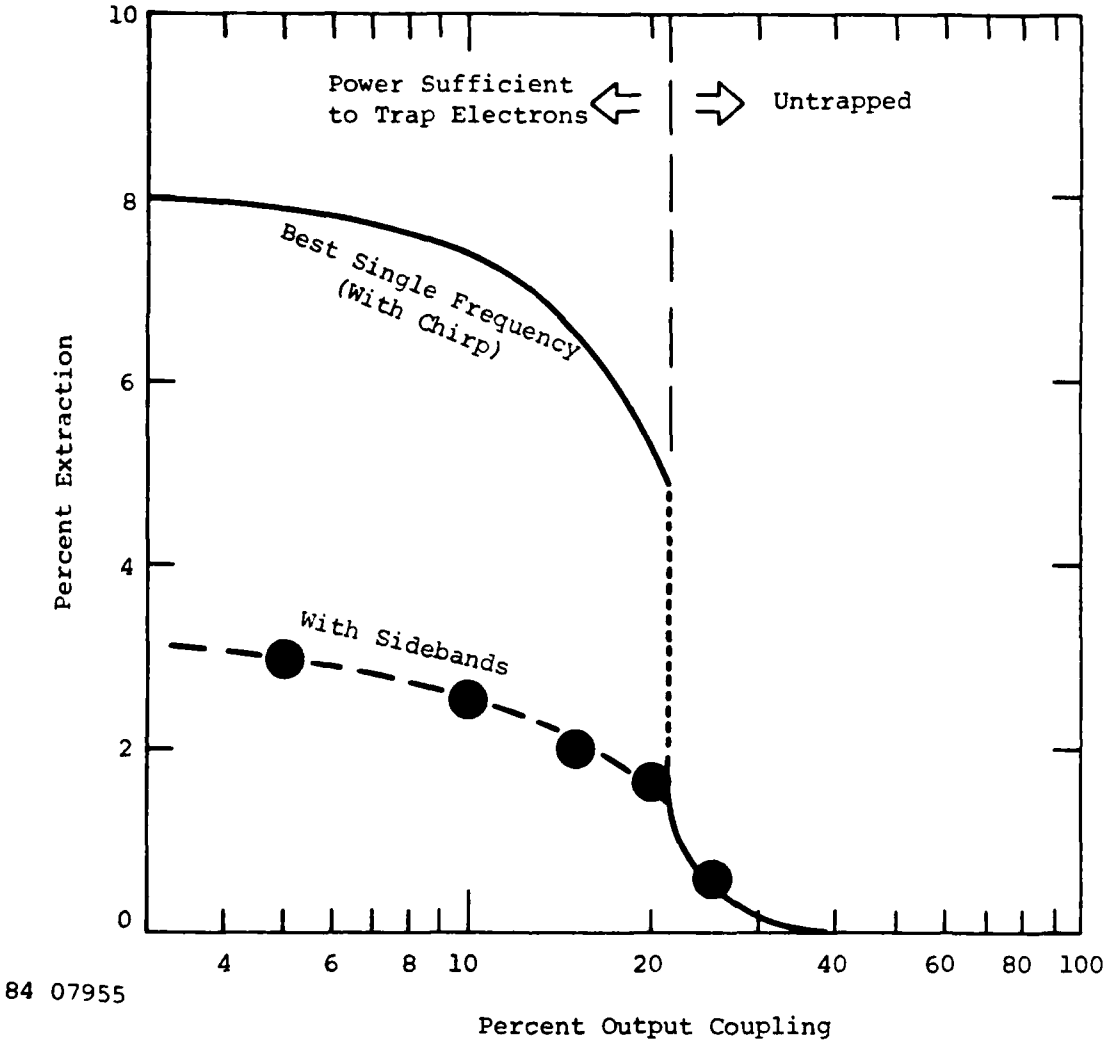

Figure 5-7. Extraction Degradation Due to Sidebands.

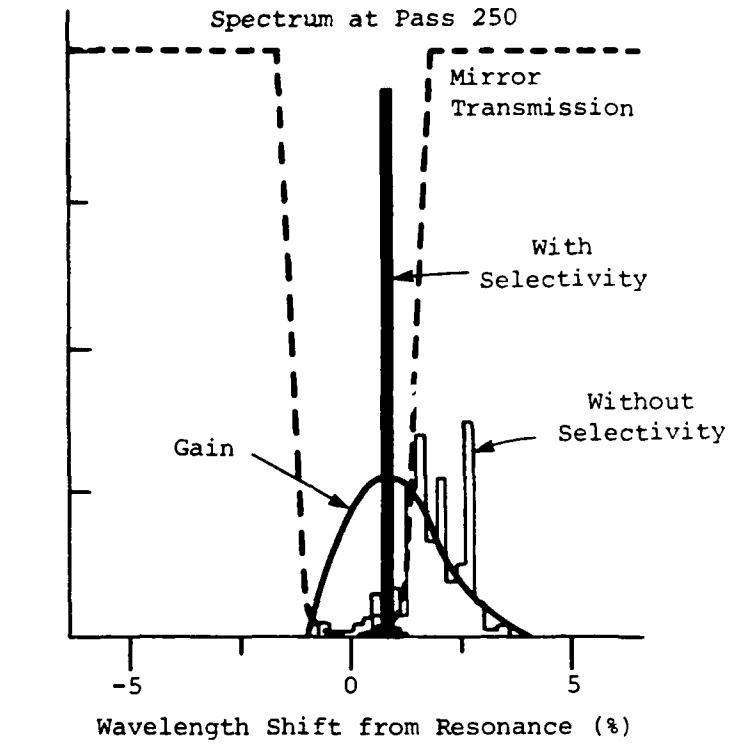

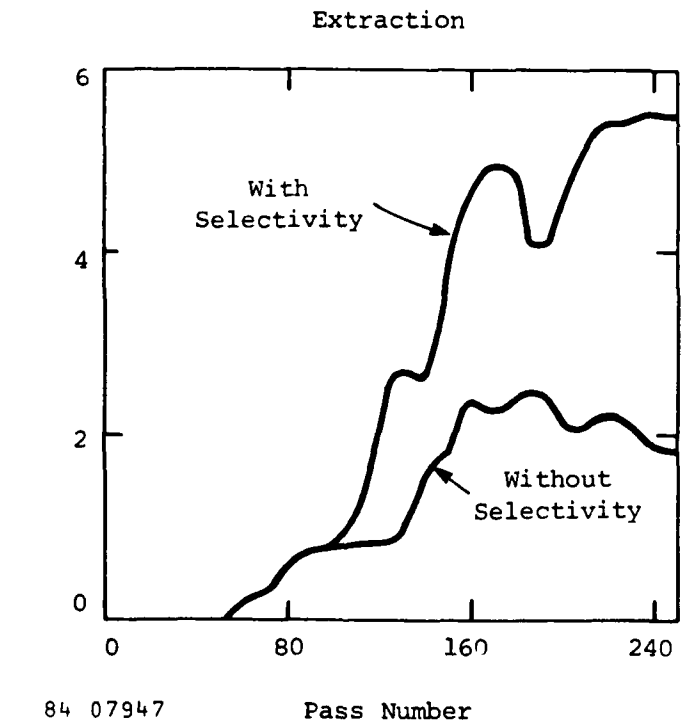

Figure 5-8. Introduction of Wavelength Selectivity Eliminates Sidebands, 15 Percent Output Coupling.

shown on the figure, evolves to about 5.6 percent, which is very close to the design value.

REFERENCES

5-1. D.C. Quimby and J.M. Slater, IEEE J. Quantum Electron., QE-19, 800 (1983), see also D. Quimby and J. Slater, in the Proceedings of the Bendor Free-Electron Laser Conference, J. de Physique 44, p. C1-397 (1983).

5-2. N.M. Kroll and M.N. Rosenbluth, "Sideband Instabilities in Trapped Particle Free-Electron Lasers," in Free-Electron Generators of Coherent Radiation, Physics of Quantum Electronics, Vol. 7, S.F. Jacobs, H.S. Pilloff, M. Sargent, M.O. Scully, and R. Spitzer, eds. (Addison-Wesley, 1980), p. 147. See also, N.M. Kroll, P.L. Morton, and M.N. Rosenbluth, "Free-Electron Lasers with Variable Parameter Wigglers," IEEE J. Quantum Electron., QE-17, 1436 (1981).

5-3. J.C. Goldstein and W.B. Colson, "Control of Optical Pulse Modulation Due to the Sideband Instability in Free-Electron Lasers," in the Proceedings of the International Conference on Lasers 1982, New Orleans, LA, December 15-17, 1982.

5-4. See for example the review by W.B. Colson and A. Renieri, "Pulse Propagation in Free-Electron Lasers," in the Proceedings of the Bendor Free Electron Laser Conference, J. de Physique, 44, p. C1-11 (1983).

5-5. M.N. Rosenbluth, H.V. Wong, and B.N. Moore, "Free Electron Laser (Oscillator) - Linear Gain and Stable Pulse Propagation," in Free-Electron Generators of Coherent Radiation, C.A. Brau, S.F. Jacobs, and M.O. Scully, eds., Proc. SPIE, 453, p. 25 (1984).

5-6. J.C. Goldstein, "Evolution of Long Pulses in a Tapered-Wiggler Free-Electron Laser," in the Proceedings of the 1983 Los Alamos Conference on Optics, Santa Fe, NM, April 12-15, 1983.

5-7. W.B. Colson and R.A. Freedman, "Synchrotron Instability for Long Pulses in Free-Electron Laser Oscillators," Optics Comm. 46, 37 (1983). See also, W.B. Colson, "Chaotic Optical Modes in Free-Electron Lasers," in Free-Electron Generators of Coherent Radiation, C.A. Brau, S.F. Jacobs, and M.O. Scully, eds., Proc. SPIE, 453, p. 290 (1984).

Section 6

OPTICAL CAVITIES

6.1 INTRODUCTION

The optical cavity of the FEL is configured quite differently from that of conventional lasers.[6-1] The main unique feature is the very long and very narrow gain region, with an aspect ratio between 1,000 to 10,000. The small size of the electron beam causes the desired optical mode to have a small radius along the entire length of the wiggler. The wiggler is long for high extraction and gain, so the cavity mode must have a large Rayleigh range. An important additional constraint is imposed by the condition that the mirrors maintain surface integrity and high-quality figure under a high flux of incident optical radiation. This latter requirement implies that the mirrors must be of sufficient size and located far from the center of the optical cavity. The optical cavity, therefore, must have a long, narrow waist which expands to a large spot size at the optical elements. The FEL is also different from conventional lasers in that the gain is unidirectional and the gain media moves at relativistic speeds.

A conventional solution to the FEL optical cavity is a near-concentric cavity with two end mirrors. Since an exactly concentric cavity will be unstable, these end mirrors have radii of curvature which are slightly larger than half the distance between the mirrors. The overall length of this cavity is determined from damage and distortion considerations for the end mirrors. An intracavity telescope consisting of two glancing-incidence mirrors can be used to scale the cavity to higher power levels while retaining reasonable physical lengths. A superior solution for a high power cavity is a ring configuration featuring two glancing-incidence mirrors and two near-normal incidence end mirrors.

The scope of this section is to present the information developed at MSNW for the technological issues as they affect the short wavelength,

i.e., visible, oscillator. This discussion has been divided into two parts, those which apply to a low-power (i.e., low duty cycle) FEL and those which are particular to the high-power (i.e., high duty cycle) FEL. A short, concentric cavity has been chosen to illustrate the low-power cavity, and a four-element, semi-confocal ring cavity has been chosen to represent the high-power cavity. Section 6.2 focuses on the issues for the low-power cavity, while Section 6.3 focuses on the additional considerations for the high-power ring cavity.

6.2 LOW-POWER CONCENTRIC CAVITY

The cavity design for an FEL oscillator is constrained by the choices of optical power, wavelength, and the efficiency of the laser. Large electron-beam energy extraction is needed for high efficiency. For large extraction, high peak optical intensities are needed to provide electron trapping and deceleration. A long, narrow optical waist is required to maximize the intensity within the wiggler. The concentric cavity is the only stable, symmetric, linear cavity that simultaneously produces a focus at the center of the cavity and large spot sizes at both mirrors. This section reviews considerations for a visible wavelength, low-power concentric FEL cavity.

6.2.1 Cavity Dimensions

The dimensions for a concentric cavity suitable for a minimum duty cycle FEL are developed in this section. A simple two-mirror concentric cavity, as shown in Figure 6-1, is considered. The FEL is chosen to be a visible oscillator with laser wavelength of around 500 nm. The e-beam energy extraction is taken to be about 5 percent from 120 MeV electron pulses of ≈3 nC total change. The total wiggler length is about 5 m. The relevant cavity parameters for the example low-power cavity are summarized in Table 6-1.

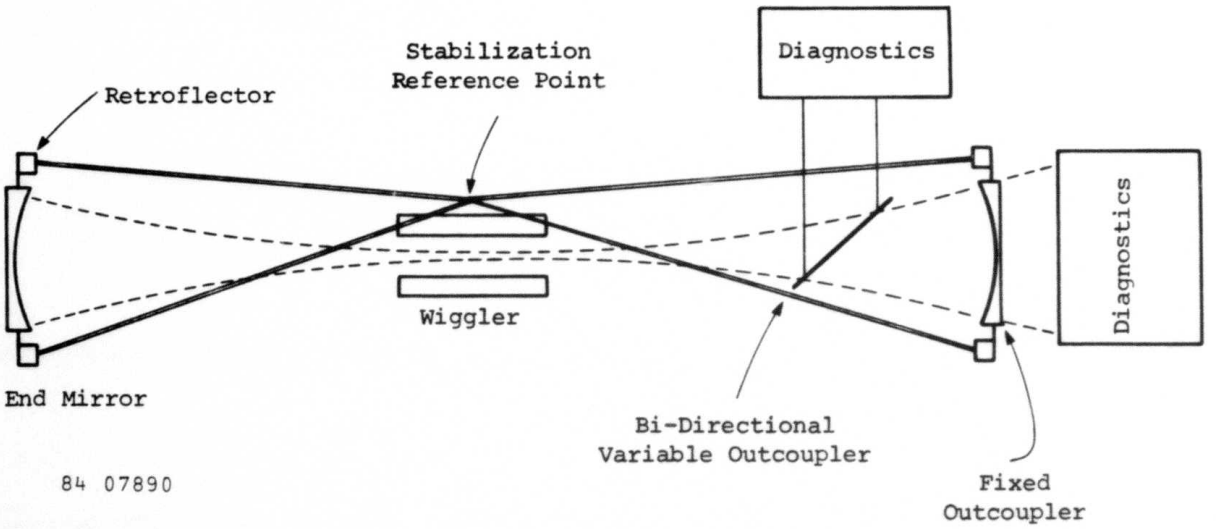

Figure 6-1. Low-Power Concentric Cavity.

Table 6-1

LOW-POWER LASER AND OPTICAL SYSTEM PARAMETERS

Laser	
Wavelength	0.5 μm
Output Power	30 kW
Gain: Small Signal	20 Percent
Saturated	10 Percent
Start-up Time (e^{20} at 7 Percent Coupling)	60 μsec*
Optical Cavity	
Total Length	60 m
Rayleigh Range	2 m
Mirror Spot	ω = 0.8 cm
Maximum Mirror Loading	400 kW/cm^2
Outcoupler	Variable Transmissive Element

*Can be reduced with cavity length.

The length of the waist region is described in terms of the Rayleigh range, Z_R, the distance over which a Gaussian beam radius grows by a factor of $2^{1/2}$. A Rayleigh range chosen to optimize laser performance is typically from 1/2 to 1/4 the wiggler length. Longer wigglers tend to give superior laser performance but at increased wiggler cost and at increased cavity length to avoid mirror damage. Choosing the Rayleigh range and wavelength determines the shape of an unaberrated freely-propagating Gaussian beam diverging from the waist located at the center of the wiggler. The Rayleigh range, for the example concentric cavity, is 2 m. The spot size radius at the wiggler center is 0.6 mm, which provides acceptable spatial overlap of the electron and optical beams.

The minimum cavity length, L, is computed based on the requirement that the optical beam radius at the end mirror be large enough to keep the optical flux below the limits for damage, distortion, or degradation of the mirror. To avoid damage or significant loss of reflectivity of the end mirrors, the beam radius, ω_m, at the end mirror must be far larger than at the waist. Using standard optical formulas for the beam waist, the minimal cavity length set by damage is(6-2)

$$L \geq \left[\frac{8\Gamma Z_R}{\lambda \Phi_D}\right]^{1/2} . \qquad [6\text{-}1]$$

where Γ is either the average power or single-pulse integrated energy exposure within the cavity, whichever is damage limiting; Φ_D is the damage limit for either power density or for single pulse integrated energy density, whichever is damage limiting; λ is the laser wavelength; and Z_R is the Rayleigh range. For an incidence flux limit of 400 kW/cm^2 (see Section 6.2.3), the length of the cavity turns out to be about 60 m. For a 60 m near-concentric cavity, the spot size on the end mirrors is ≈0.8 cm. A mirror with a radius of about three times this value intercepts greater than 99 percent of the beam energy.

The radius of curvature of the end mirrors for a near-concentric symmetric resonator is given by[6-3]

$$R = \left[\frac{L}{2}\right]\left[1 + \frac{Z_R^2}{[L/2]^2}\right] . \qquad [6-2]$$

This relation implies careful selection of mirrors to simultaneously satisfy the cavity length requirement and the small permitted changes in focal length (≈1.5 cm). This topic is discussed in Section 6.2.2.

6.2.2 Alignment Tolerances

End mirror geometric parameters whose values are important to FEL performance include separation, angular pointing, centering in the two transverse directions, and focal length. The angular positioning tolerance of the end mirrors is based on the required spatial overlap of the optical axis with the wiggler axis. The mirror separation (cavity length) tolerance arises from the necessary temporal overlap of the laser pulse with the driving electron pulses. Degradation of optical gain due to misalignment may result from loss of spatial or temporal overlap with the electron beam, aberration due to figure errors or roughness in the optics, or losses at the apertures defined by the wiggler bore.

6.2.2.1 Length Requirement

The spatial length of the electron micropulses will be about 5 to 10 mm. If the cavity length is 10 μm from the design value for exact temporal overlap of the electron and optical pulses, then in 250 round trips (sufficient for start-up) the laser pulse will have walked off of the electron pulse by 2.5 mm (about half of the laser pulse length). Thus 10 μm is a reasonable limit to place on cavity length deviations.

6.2.2.2 Angular Requirement

The alignment tolerance in an FEL is determined by the spatial overlap between the optical beam and wiggler (electron beam) axes over the distance corresponding to the wiggler length. The electron beam is generally slightly smaller than the photon beam and the interaction length is two to three Rayleigh ranges long. For good interaction strength, the photon beam axis should not deviate from the wiggler axis by more than a small fraction of a beam diameter in this interaction region. Tilting a resonator mirror will displace the cavity axis, causing beam walk-off and optical axis tilt. Both effects must be considered to determine the cavity angular tolerance.

The concentric cavity for the FEL has severe alignment sensitivity since the centers of curvature of the end mirrors, which define the optical axis, lie near one another in the wiggler. A small mirror tilt thus results in a magnification of tilt in the optical axis. This magnification is of the order of the distance between the end mirrors divided by the distance between the focii. For near-concentric cavities, the magnification can be very large. This angular alignment tolerance becomes more severe at shorter wavelengths, and the allowed misalignment scales as the square root of the wiggler length and the three-halves power of the laser wavelength.

The alignment tolerance on the end mirrors can be defined by requiring the optical axis to stay within some fraction of the laser beam waist radius. One-third of the waist radius is chosen for this example, which is sufficient to preserve electron beam overlap and eliminate losses at the apertures. When an end mirror is tilted by an angle θ, the optical axis is tilted by an angle ϕ, which is larger than the tilt of the end mirror by a factor of 1.5 times the ratio of the wiggler length divided by the beam waist size. Since the Rayleigh range is much less than the cavity length, the centers of curvature of the mirrors are separated by far less than the wiggler length, and the optical axis can be considered to pivot

about the middle of the wiggler. The mirror centers of curvature are displaced from the cavity center by Z_R^2/R, so that the mirror tilt (θ) and the optical axis tilt (ϕ) can be related by

$$\theta R = \phi \left[\frac{2Z_R^2}{R}\right] . \qquad [6-3]$$

Assuming the wiggler length is about two Rayleigh ranges, then a tolerance on θ can be found in terms of Z_R, λ, Φ_D, and Γ for a cavity where the length (L) is the minimum allowed to avoid mirror damage. The angular tolerance on end mirror tilt is then:[6-2]

$$\theta \leq \frac{Z_R^{1/2}\ \lambda^{3/2}\ \Phi_D}{3\pi^{1/2}\Gamma} . \qquad [6-4]$$

This is the main scaling equation for alignment tolerances based on geometric optics. The mirror alignment sensitivity is seen to be tightened at short wavelengths, short Rayleigh ranges, and at higher powers or energies.

The angular sensitivity of a cavity may also be analyzed by use of standard matrix formalism.[6-3,6-4] As shown in Reference 6-4, a key parameter in this formulation is $\epsilon = (2R-L)/R$, which is a measure of how far the cavity is from being concentric. To determine the tilt sensitivity of a mirror, the matrix for the cavity is determined with the reference plane at the mirror that is to be tilted. After each pass of a ray through the reference plane, twice the angular tilt of the mirror is added to the slope of the ray. The cavity axis is defined by the ray that exactly reproduces itself on one round trip. This ray is unique. The slope and displacement of this ray are the tilt and displacement of the new optical axis from the old optical axis at the reference plane. Propagating this ray through the optical cavity with the matrix formalism yields the axial displacement and tilt at any position in the cavity.

For a two element cavity with $\epsilon \ll 1$, the Rayleigh range (Z_r), spot size at the mirror (ω_m) and at the focus (ω_o) are given by[6-4]

$$Z_r = \frac{L}{2}\left[\frac{\epsilon}{2}\right]^{1/2} \qquad \omega_m^2 = \frac{\lambda L}{2\pi}\left[\frac{2}{\epsilon}\right]^{1/2} \qquad \omega_o^2 = \frac{\lambda L}{2\pi}\left[\frac{\epsilon}{2}\right]^{1/2}. \qquad [6\text{-}5]$$

The tilt and deflection of the central axis at the mirror surface is given by:

$$r_o = -\frac{L\theta_m}{2\epsilon} \qquad r_o' = \frac{\theta_m}{\epsilon} \qquad [6\text{-}6]$$

where θ_m is the tilt of the mirror. This is consistent with Equation [6-4]. Propagating the ray to the cavity center shows that the displacement is small, but the angular tilt is very large. For the low-power concentric cavity described in Table 6-1, the angular tilt tolerance is calculated to be 400 nrad, allowing spot movement within the wiggler of approximately $\omega_o/4$.

The tolerance derived using geometric or ray optics does not change if a telescope is inserted between the wiggler and the end mirror in order to shorten the cavity, if the mirror spot sizes and Rayleigh ranges are equal in the telescoped and untelescoped cavities. To first order, the allowed tilt of the optical axis is unchanged by use of a telescope, and the distance between the centers of curvature of the two mirrors is also unchanged. The lateral displacement of the center of curvature of a mirror, when that mirror is tilted, is unchanged by a beam expander because a magnification, m, in image size corresponds to demagnification, 1/m, in angle. As the cavity length is demagnified, the angle is magnified a corresponding, but inverted, factor so that the displacement does not change with magnification.

6.2.2.3 Mirror Focal Length

The spot size of cavities operating near the stability limit are very susceptible to variations in focusing. This problem was analyzed using the matrix formalism[6-3] to obtain a tolerance on the mirror focal length. The radius of curvature of one of the end mirrors was adjusted until a 5 percent change in the cavity spot size in the wiggler was obtained, with all other focal distances and element separations held constant. For the low-power concentric cavity of Table 6-1, change in mirror radius of curvature of about 3 cm caused a 5 percent change in the spot size.

6.2.3 Optical Components

The optical components of the concentric cavity must be able to withstand high incident fluxes of laser light while maintaining their surface figure and reflectivity. They may also be situated in an environment which has high fluxes of UV and gamma ray radiation. Over the course of a macropulse, the optical elements will also be subjected to thermal loading. The main concerns are damage, distortion, and degradation of the coating or surfaces of the optical elements.[6-5,6-6]

The cavity length was chosen in Section 6.2.1 to reduce the incident laser flux to a tolerable level at the end mirrors. Materials for mirrors suitable to the FEL application have been experimentally found to withstand visible laser pulses with an incident flux of 400 kW/cm^2 in a temporal format similar to that of the FEL.[6-7] This value is consistant with a spot size of 0.8 cm at the end mirrors and a mirror loading of 400 kW.

The thermal distortion of a fused silica mirror has been estimated based on the combined effects of thermal mapping and thermal bending expected in the concentric cavity. The laser radiation was taken to have a 0.8 mm Gaussian radius spot and to be at normal incidence to a 5 cm diameter end mirror. A worst case estimate of the absorption in the multilayer dielectric coating is 10^{-3} of the incident radiation, which

results in a maximum power absorbed of 400 W. The substrate was taken to be effectively transparent. The thermal bending calculation was based on the theory of thermal stresses in plates,[6-8] with asssumption of linear temperature profiles. From this calculation, the mirror distortion caused by thermal mapping was found to be only 10 percent of that caused by thermal bending. The maximum mirror distortion after a macropulse of 100 μs at full power is estimated to be 4.0 nm. The resulting change in apparent radius of curvature is 5 cm. This change somewhat exceeds the 3 cm allowable limit developed in Section 6.2.2.3, but is based on a worst case estimate of both the absorption and average macropulse power (no allowance is made for the 60 μs start-up time).

In order to accurately control the spot size in the wiggler, the effective focal length of the mirrors must be determined and maintained to about one part in a thousand. Fabrication to such exacting tolerances is time consuming and expensive. One solution is to have a lens and mirror combination as one of the end mirrors. The separation distance between the lens and the reflector (which could be flat) serves to adjust the effective focal length. Another solution is to obtain a large set of independently ground and polished substrates with a designed radius of curvature of 30 m. These substrates may have a relaxed tolerance of, say ±3 percent. By carefully measuring the focal length of the mirrors, a matched pair whose centers of curvature are separated by the design value of about 27 cm can be obtained. Measurement accuracies of 0.01 percent of the focal length are possible.[6-9 to 6-11]

An alternative to measuring the focal lengths and then using these focal lengths to calculate the Rayleigh range of the optical cavity is to measure the Rayleigh range directly. A lasing medium, e.g., argon ion, can be placed in the optical cavity and the mode structure, i.e., spot size distribution, can then be determined. By this method, the performance of the actual optical elements is determined before these elements are operated with the FEL.

6.2.4 Stabilization

The ability of interferometers to sense small motions[6-12,6-13] and provide stabilization of laser optics has been demonstrated. Commercial two-color interferometers, such as those manufactured by Hewlett-Packard, can resolve path differences of $\lambda/60$, which is 10 nm. An alternate technique based on an acousto-optical modulator could be utilized to stabilize mirrors to better than $\lambda/100$.[6-13,6-14] A $\lambda/60$ resolution is sufficient to meet the length and angle tolerances of the FEL optical cavity.

The two angular motions of each end mirror can be stabilized with two perpendicular "v" interferometers, as illustrated in Figure 6-2. The two "v" interferometers on each of the end mirrors are capable of sensing both horizontal and vertical tilt of the end mirrors relative to a reference point on the wiggler. Based on a separation between the corner cube reflectors of about 10 cm, a tilt of 400 nrad will cause a path length change of about 40 nm, which is larger than the resolution of the commercial two-color interferometer. The angular adjustment of the mirrors is referenced to the wiggler since the wiggler center axis defines the optical axis of the FEL. As shown in Figure 6-2, the corner cube retroreflectors are mounted on the same mirror mount holding the laser end mirror, and thus will faithfully detect unwanted motions of this end mirror. Two PZT transducers can correct for tilts in the two orthogonal planes after receiving the error signal from the motion sensing interferometers. Another factor which makes this "v" configuration even more attractive is that the path lengths of the two interferometer arms are nearly equal, so that coherence length of the laser source is not of concern.

The alignment of the optical cavity can vary due to both rotational and transverse translational motion of the end mirrors. These motions produce error signals which are not distinguishable with the "v" interferometer. The proper correction of transverse translation can be

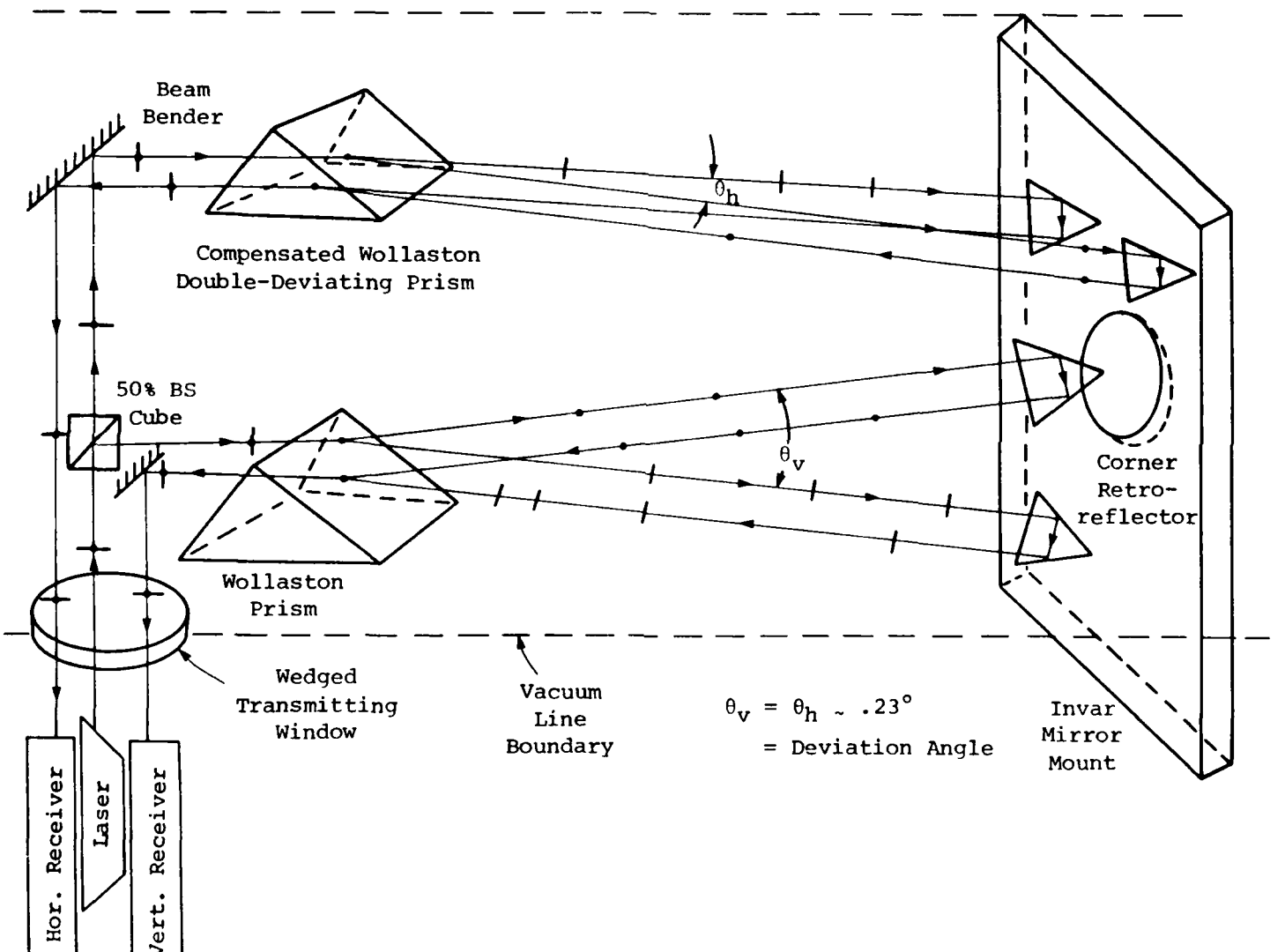

Figure 6-2. Angular Alignment Stabilization Interferometer.

84 07891

achieved by driving the error signal from the "v" interferometer to zero by using the PZT transducers which control the angles. Thus rotational and transverse translation errors need not be distinguishable and either can be used to correct the other.

To take advantage of the high sensitivity of the interferometer, there is a need to maintain accurate control of the speed of light over the interferometer legs, to minimize blooming, and to prevent beam steering. Therefore, the interferometer legs from interferometer to retroreflectors must be inside a vacuum system. However, the vacuum need not be very high for these effects to be rendered negligible.

The "v" interferometers are insensitive to motion along the direction of the wiggler axis, allowing separate control of the distance between the mirrors for the purpose of maintaining temporal overlap between the electron and optical pulses. The length tolerance of 10 μm is three orders of magnitude above the 10 nm resolution of the commercial two-color interferometer. The cavity length can be stabilized to 10 μm with a single-beam linear interferometer.

6.2.5 Output Coupling

The optimum outcoupler would provide variable outcoupling, add no distortion to the phase front of the laser pulse, and not be sensitive to the flux of light or the energetic emissions from the wiggler. For the low power cavity, where transmissive elements can be allowed inside the cavity and the optical elements need not be cooled, the two leading candidates for outcoupling are the partially transmitting end mirror and a thin, highly polished intracavity plate tilted at an angle near Brewster's angle.

The partially transmissive end mirror permits outcoupling without adding transmissive elements inside the cavity and, consequently, the optical round trip time is well defined by the distance between the

mirrors. However, the amount of outcoupling is not variable without changing the mirrors. A mirror change implies several end mirrors, so that this scheme is most appropriate for configurations that do not require mirror curvature known to high precision.

A thin, highly-polished (low scatter) intracavity plate tilted at angles near the Brewster angle can provide a variable outcoupler. Tilting this plate to Brewster's angle to minimize outcoupling can aid in start-up of laser action. Changing the tilt angle increases the outcoupling. The plate can be made of UV absorbing material which is still highly transmissive in the visible (e.g., optosil). Thus the plate can serve to protect the expensive end mirror coatings from potentially damaging UV harmonics produced by the wiggler. The plate is inexpensive relative to the end mirror and replacement could be reasonably rapid since it does not require realignment of the cavity.

The disadvantages of the plate relate to insertion of an optical element into the cavity and production of two output beams. The additional element means greater possibility for wave front distortion, and since the entire circulating power goes through the plate, dynamic distortion due to heat load is added. Since the index of refraction of the plate is different from that of vacuum, the cavity length must be adjusted to maintain the required round trip time. Tilting the plate away from the initial alignment position to adjust the outcoupling changes the cavity length. Due to refraction effects, tilting the plate also displaces the optical axis. Thus, the cavity length control and angular alignment would require minor readjustment when the outcoupling is changed.

A tilt of approximately 4 degrees from Brewster's angle results in a total output coupling of about 10 percent, 5 percent per surface. One surface could be antireflection coated to maximize the power outcoupled into a single beam and to avoid an etalon effect. For a 2 mm thick plate, this tilt causes a displacement of the optical axis by about 0.12 mm from its previous centerline. This amounts to about one-third of the electron

beam radius and, hence, some readjustment of the end mirror may be required. The change in effective cavity round trip distance for the 4 degree tilt from Brewster's angle is 40 μm, which is four times larger than the cavity length tolerance. This would upset the temporal overlap between electron and optical pulses, and thus adjustment of the cavity length will be required when the output coupling is changed.

The advantages of the tilted plate output coupler are significant and place it as the leading contender for a low-power concentric cavity. Particularly important for this recommendation is the potentially important protection role afforded by the relatively inexpensive plate and also the relative ease of variation of the amount of outcoupling.

6.2.6 Wavelength Selectivity

Wavelength-selective optics in the laser cavity may be the solution to the anticipated problem, described in Section 5.2, of sideband growth in the FEL spectrum. The sidebands develop with an offset of around 1 percent from the center wavelength. Thus, the desired wavelength selectivity is approximately 1 percent, i.e., in a range of around 5 to 10 nm. The wavelength-selective element must provide sufficient losses to suppress the sideband evolution without adding losses to the cavity which prevent startup at the design wavelength. The selective optics must add very little wave front distortion, around $\lambda/100$ per surface. This implies highly homogeneous materials, especially for transmissive elements, and very high quality optical surfaces. Possible options for wavelength selectivity include birefringent filters and multilayer dielectric mirror coatings.

Birefringent filters, constructed of uniaxial crystalline quartz, will exhibit a rotation of the plane of polarization of an input light beam which is wavelength dependent. Thus, a birefringent plate can induce a wavelength dependent loss into a cavity due to the reflectivity differences of light waves with p and s polarizations.[6-15] A single birefringent

plate has the property of converting an incident linearly polarized p-wave beam into one with elliptical polarization, which can be thought of as a combination of both p-wave and s-wave components. The light which is transformed into s-wave polarization is no longer available to stimulate emission into the lasing mode at that wavelength. Wavelengths for which the optical axis of the plate is oriented so as to neither alter nor attenuate the incident p-polarized wave, will be the ones most likely to oscillate. The light emitted from the planar wiggler is plane polarized, thus the birefringent filter at Brewster's angle can provide minimum loss at a selected wavelength and greater loss (increased outcoupling) at other wavelengths. Wavelength tuning of the Brewster's angle plate is accomplished by rotation of the crystalline axis in the plane of the plate.

The thickness of the birefringent plate influences the sharpness of the transmission curve of the filter, with thicker plates providing narrower bandwidths. The thickness can be chosen to match the desired wavelength selectivity for the FEL. For example, a 0.76 mm thick crystalline quartz plate tilted at Brewster's angle, with a 50 degree angle between the optical and crystalline axes, can have a transmission peak centered at 550 nm with a bandwidth of 50 nm. The transmission is about 10 percent lower at a wavelength which is 1 percent from the center wavelength.[6-15]

The damage level of this birefringent filter, which is uncoated and used at Brewster's angle, is as high as for a tilted-plate output coupler. The nature of the material (crystalline quartz) ensures very low wave front distortion. When the birefringent filter is inserted into the cavity, the optical round trip time of the cavity is changed by $(n-1)d$ where d is the thickness of the material and n is its refractive index. The optical axis is also displaced. These effects must be taken into account by the positioning and stablization systems.

Frequency-selective maximum reflectance coatings on the mirrors, with sufficient reflectivity and selectivity adequate to control the sideband instability, would require multilayer stacks which are 40-50 periods thick.[6-16] Large stacks are known to have significantly lower resistance to damage than short stacks,[6-17] but the damage thresholds have not been determined for the FEL application. Since the wavelength for maximum gain changes during start-up, it is possible to have a coating which has maximum reflectivity during start-up, with lower reflectivity, and hence higher outcoupling (if the substrate is transparent), at the saturated wavelength.

6.3 HIGH-POWER RING CAVITY

For high power systems there exists a particular ring geometry which has clear advantages over the concentric cavity described in Section 6.2. The principal advantage is a greatly relaxed alignment tolerance; the advantage increases as the power and optical element size increases. Other advantages include reduced heat loading and figure requirements on the optical elements. In this section the ring concept is developed for the high power FEL. High power operation would most likely be realized by decreasing the spacing between micropulses rather than increasing the energy content of individual micropulses.

6.3.1 The Semi-Confocal Ring

Given the physical constraints, the high incidence flux, and the quest for the least number of elements in the cavity, the most promising ring configuration has four elements, is symmetric around the plane that bisects the center of the wiggler, and is perpendicular to the optical axis. As shown in Figure 6-3, this ring is composed of two beam-expanding glancing-incidence mirrors, one on either side of the wiggler, and two end mirrors tilted slighty from normal incidence. It is similar to a confocal ring, but differs in that the optical length of the top leg is significantly shorter than the bottom leg. A shallow glancing incidence

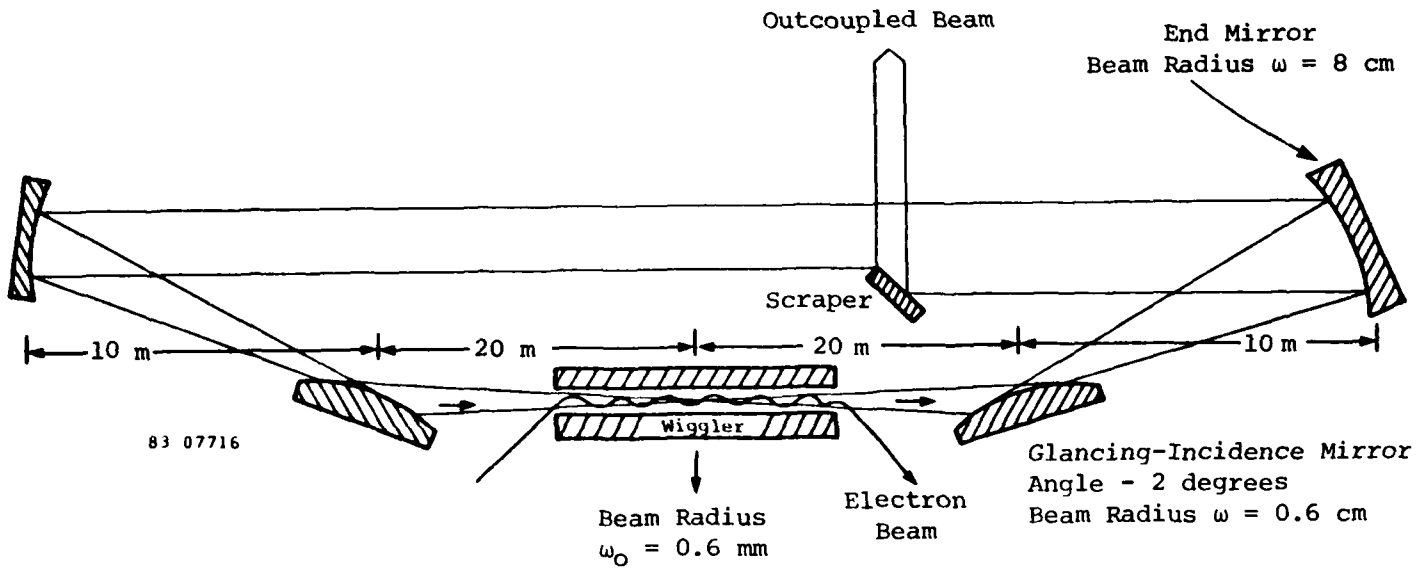

Figure 6-3. Diagram of Four-Element Ring Cavity with Output Scraper.

angle serves both to increase the reflectivity of the mirror, and to decrease the mirror thermal loading by increasing the beam footprint on the optics. Each end of the ring cavity acts as a telescope, and it has a long narrow focus centered in the wiggler. As discussed previously, such a focus is necessary to maximize the FEL interaction. Both electron and optical pulses will circulate in the same direction in the cavity, and the pulses will be similar in length. When the separation between electron micropulses exactly matches the cavity optical round trip time, a single pulse will be present in the cavity. As higher harmonics of this frequency are employed, the number of independently circulating laser pulses will increase accordingly, resulting in higher laser power.

6.3.2 Cavity Dimensions

An example ring cavity design is illustrated in Figure 6-3, with the nominal dimensions shown. The axial dimensions are quite similar to those of the concentric cavity since they both need to satisfy the same constraints on the spot size in the wiggler and the coincidence of the electron and optical pulses. The end mirrors are somewhat larger, however, to provide higher power handling capability. The wiggler length is 5 m. To avoid the problems of lateral curvature of the glancing-incidence mirrors, as discussed in Section 6.3.5, and still have a suitable telescopic magnification, the glancing-incidence mirror is located about 10 m from the end mirror. If the glancing-incidence mirrors are at 2 degrees and the Rayleigh range is 2 m, then the glancing-incidence mirrors can be located 20 m from the center of the wiggler. This gives a factor of seven higher surface loading on the glancing-incidence elements than on the end mirrors. The overall cavity length is 60 m. As shown schematically in Figure 6-3, the spot size is approximately constant at around 8 cm across the entire distance of the return leg. This large beam cross-section may prove useful for insertion of transmissive outcoupling and frequency tuning elements.

In the case of the four-element ring, all elements are reflective and thus can be cooled elements, when required. The nominal sizes of the optical elements are listed in Table 6-2. The ring cavity is sized in accordance with the expected damage limit of the optical coatings as in the low-power concentric cavity. The higher duty factor desired for the ring leads to larger mirror sizes. The spot size at the end mirrors is chosen to be 8 cm and the diameter of the end mirrors is 24 cm. To expand the spot size to this dimension, the glancing-incidence mirrors, when placed at two degrees to the optical axis, require curvatures of the order of 5 cm in the lateral direction and 40 m in the longitudinal direction. The radius of curvature of the end mirrors must then be around 20 m to provide the proper telescoping. Since the laser pulse circulates in one direction, each optical surface sees the pulse only once per round trip. This halves the expected loading on the glancing-incidence surfaces when compared to an equivalent concentric cavity incorporating glancing-incidence elements. The spot size at the glancing-incidence mirrors is about 0.6 cm and the size of the glancing-incidence mirror is 50 cm in the longitudinal direction and 1.7 cm in the lateral direction.

6.3.3 Advantages

The four-element ring cavity as described schematically in Figure 6-3 has significant advantages over the equivalent concentric cavity. The principal advantage is that the pointing tolerance of the end mirrors, which is developed in Section 6.3.4, is approximately 10 times less stringent. The laser pulse travels through the wiggler only once per round trip, so that the diffractive losses at the wiggler are decreased. The glancing-incidence mirrors see each pulse only once per round trip, thus seeing only half the heat load that would be incident for an equivalent telescoping concentric cavity. Also the figure requirement on the glancing-incidence mirrors would be less severe than for the equivalent telescoping concentric cavity, since each glancing-incidence mirror contributes only once to the wave front distortion.

Table 6-2

GENERIC HIGH-POWER RING CAVITY DIMENSIONS

Overall

Gain - 40 Percent

Spot Radius at Wiggler - 0.6 mm

Rayleigh Range at Wiggler - 2 m

Optics

	End Mirrors	Glancing Mirrors (at 2 degree)
Diameter (cm)	24	1.7 Lateral, 50 Longitudinal
Curvature (m)	20	0.05 Lateral, 40 Longitudinal
Figure Error	$\lambda/100$	$\lambda/4$

For the concentric cavity, two-sided scraping is necessary to avoid driving the beam off-axis. A scraper outcoupler need only scrape on one side of the beam in the ring cavity because rays flip from the inside to the outside of the beam on alternate passes. A detailed mode calculation is required to determine the amount of disruption caused by the scraper. The large beam size, nearly collimated leg of the ring resonator provides a good location for frequency-selective elements.

6.3.4 Tolerances

The angular alignment tolerance for the ring cavity is drastically relaxed compared to that of the equivalent concentric cavity. The tolerance for the ring is given approximately by the ratio of the displacement allowed at the wiggler divided by the effective optical distance from the wiggler center to the end mirror. Comparison of the permitted angular variation is made in Table 6-3 for example concentric and ring cavity designs. The geometric alignment tolerance for the ring is relaxed by an order of magnitude relative to the diffractive alignment tolerance (discussed below) of the equivalent concentric design. Diffractive effects have not yet been calculated for the ring geometry, but they can only relax the tolerance and are not expected to be large.

Diffractive beam steering effects are quite important in the concentric cavity. For the example concentric design, the mirror alignment tolerance based on the geometric analysis of Section 6.2.2 is about 4 nrad. The diffraction limit of the mirror (the wavelength of the light divided by the mirror diameter) is about 1 μrad, over two orders of magnitude larger than the alignment tolerance. To sense an angular tilt as small as the alignment tolerance, the beam must circulate many times in the cavity. Since it takes many cavity round trips before sensing the losses associated with the misalignment, diffractive effects may cause the true optical axis, defined by the intensiy centroid, to be displaced from the geometric axis. To calculate how long it takes an off-axis ray to locate the geometric axis, consider the situation shown in Figure 6-4. An off-

Table 6-3

ALIGNMENT TOLERANCE COMPARISON

Parameter	Concentric	Ring
Wavelength (μm)	0.5	0.5
Equivalent Cavity Length (m)	500	500
Rayleigh Range (m)	1	1
Wiggler Spot Radius (mm)	0.4	0.4
End Mirror Spot Radius (cm)	10	10
Geometric Alignment Tolerance (nrad)	4	400
Diffraction Alignment Tolerance* (nrad)	55	-
G.I. Mirror Geometric Tolerance (nrad)	-	6700
Total Cavity Length Tolerance (μm)	10	10
End Mirror to G.I. Length Tolerance (μm)	-	250
G.I. to G.I. Mirrors Length Tolerance (μm)	-	20,000

*At 5 percent scraping loss.

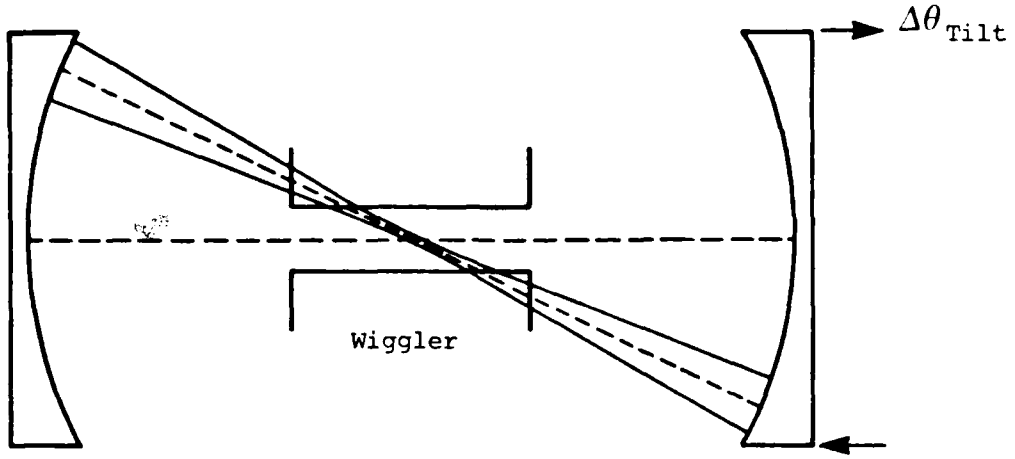

Figure 6-4. Geometric Picture of the Case Studied to Determine Diffractive Beam-Steering Effects. The cavity was misaligned so that the optical axis intersects the aperture and geometrical losses are near 100 percent.

axis ray circulates paraxially in a near-concentric cavity. By using the matrix formalism, the number of cavity round trips, n, needed for a ray to self-replicate is determined to be

$$n \cong 1.5\ L/Z_R\ . \qquad [6\text{-}7]$$

The ray will cross the new axis in roughly one-quarter this number of passes.

A model of wave front propagation in a near-concentric gain-free FEL cavity was used to determine alignment sensitivity. The case studied is given by: a cavity length of 500 Rayleigh ranges, a wiggler three Rayleigh ranges long, a wiggler bore 4 ω at the exit, and a Rayleigh range of 1 m. Optical propagation is modeled using a fast Fourier transform expansion of the wave front into a series of plane waves traveling at different spatial angles. A TEM_{00} wave is injected into the cavity along the original untilted axis, but the end mirror is tilted. The diffractive loss due to clipping at each end of the wiggler is calculated and evolution to a steady mode structure is observed. For the case shown in Figures 6-4 and 6-5, $\Delta\theta$ was 55 nr, enough for the wiggler aperture to intersect the geometrical optical axis and create ≈100 percent loss per pass. The computed losses are far lower, equilibrating at about 5 percent per round trip. Consequently, the alignment tolerance defined by the geometric analysis is far too restrictive. This is true in only the cases when L/Z_R is very large, perhaps 10^2 or greater. Even with this effect, tolerances are still far tighter than the diffraction-limited pointing tolerance.

The angular tolerance of the ring can be determined following the analysis of Reference 6-4. We may define L_1 to be the physical distance between the end mirrors and L_2 to be the effective optical path length between the end mirrors along the leg of the ring containing the wiggler. The length L_2 is fixed at $2f(1-\epsilon)$ where f is the focal length of the end mirrors and $\epsilon \ll 1$. When L_1 is reduced to be less than L_2, the beam propagating along L_1 becomes collimated with a large spot size, and a tight

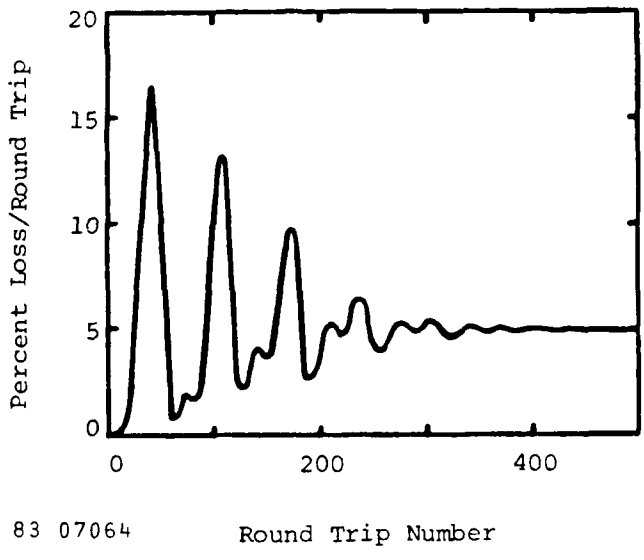

Figure 6-5. Optical Losses per Round Trip Including Diffractive Beam Steering Effects for the Case Shown in Figure 6-4.

focus appears at the center of L_2. The parameter ϵ has an equivalent effect on the resonator mode spot size as it does in the concentric cavities. The Rayleigh range (Z_r), mirror spot sizes (ω_m) and the focal spot size (ω_o) are given by

$$Z_r = \frac{L_2}{2}\left[\frac{\epsilon}{j_1}\right]^{1/2} \qquad \omega_m^2 = \frac{\lambda L_2}{2\pi}\left[\frac{j_1}{\epsilon}\right]^{1/2} \qquad \omega_o^2 = \frac{\lambda L_2}{2\pi}\left[\frac{\epsilon}{j_1}\right]^{1/2} \qquad [6\text{-}8]$$

where $j_1 = 1 - L_1/2f$. The parameter ϵ has almost no effect on the angular tolerance. The cavity tilt and displacement, at the tilted mirror, are given by

$$r_o = -\frac{j_1 L_2 \theta_m}{2} + O(\epsilon) \qquad r_o' = \left[1 - j_1\right]\theta_m + O(\epsilon) \qquad [6\text{-}9]$$

which are well defined even when ϵ goes to zero. Propagating the central ray to the wiggler shows that the beam wander is given by $f\theta_m$.

In order to compare the geometrical alignment tolerances of the semi-confocal ring with a concentric resonator design, consider the 500 m long designs given in Table 6-3. Each cavity has a 0.4 mm focal spot size and a 10 cm spot size on the mirrors. Tilting the concentric cavity mirror 4 nrad causes insignificant focal point wander, but the cavity axis tilts 125 μrad. This produces a 0.125 mm beam wander 1 m from the focus and a 3 cm beam wander on the mirrors. For a semi-confocal ring, with the same cavity length, a mirror tilt of 0.4 μrad causes a beam wander of 0.1 mm at the focus and less than 0.4 μrad tilt of the cavity axis. Therefore, in this example, the semi-confocal ring has 100 times greater geometric tilt tolerance than the concentric cavity. As already discussed, diffraction improves the concentric cavity alignment tolerance if some scraping losses at the wiggler are acceptable. The 5 percent scraping loss in Table 6-3 would be excessive in a realistic system.

As a physical justification for the great difference in angular tolerances for the two cavities, consider the effect of the tilt on the

original central ray. In the concentric cavity, if a zero slope ray is tilted by a positive amount, it propagates around the cavity through two focii and returns with a positive slope. The mirror tilt then adds to this slope and deviates the ray further away from the original direction. In the ring cavity, when a zero slope ray is tilted by a positive amount, it propagates around the ring through a single focus and returns with a negative slope. Adding the mirror tilt pushes the ray back towards the original direction. This round trip cancellation is the source of the angular stability. By adding an odd number of additional cavity mirrors, the angular stability of the ring cavity can be destroyed.

For high-power FELs, required cavity lengths for simple concentric cavities are very long. To decrease this length, glancing-incidence optics are included in the design. The presence of these elements actually simplifies the ring system. In both the linear and ring cavities, the effect of glancing-incidence mirrors is to form a beam-expanding telescope with the end mirrors. For equal spot sizes, the alignment tolerances are equivalent for long cavities and short cavities with telescopes. In the ring system, the telescope magnifies the optical length of L_2 such that it is much greater than L_1 even when the physical distances are nearly equal. Therefore j_1 will be approximately equal to 1, which is optimum for establishing large mirror spot sizes. Ray tracing and matrix analysis have been used to verify that the angular tolerances of simple ring and telescoped ring cavities are equivalent.

The effect of the position of the glancing-incidence mirrors on the length and tilt tolerances in the symmetric four-element ring cavity was determined for a cavity defined by: total path length of 120 m, laser wavelength of 532 nm, spot size in the center of the wiggler of 0.4 mm, glancing incidence angle of 1.5 degrees, and the spot size on the end mirrors of 100 mm. The optical axis displacement and tilt at the ring cavity focus when the glancing-incidence and end mirrors are tilted were determined as a function of the position of the glancing-incidence mirrors. Tolerances are defined as the displacement or tilt which produces

a 0.1 mm optical axis displacement within the wiggler. The displacement in the legs of the ring cavity which would result in a 5 percent change in the spot size at the focus was also determined. For these calculations, only one side of the cavity was altered, so that the cavities deviated only slightly from being symmetric. Results are given in Table 6-3. The tilt tolerance of the end mirror, at ≈400 nrad, is independent of the location of the glancing-incidence mirror. The tilt tolerance for the glancing-incidence mirror varied from 10 to 4 μrad as the glancing-incidence mirror was moved away from the focus. The length tolerance between the center and the glancing-incidence mirror tightened from about 35 to 15 mm as the glancing-incidence mirror was moved away from the center. The length tolerance from one glancing-incidence mirror to its corresponding end mirror (i.e., only one such leg changed) also tightened as the glancing-incidence mirror moved away from the center, with the values of about 250 μm for the closest and 8 μm for the furthest position. Large changes, greater than a meter, in the distance between the end mirrors are required for even a 0.1 percent change in spot size at the focus. The tolerance for total cavity length is determined by the required overlap between the circulating laser pulse and the electron pulses, hence, the tolerance is 10 μm for both the ring and concentric cavities. The 10 μm tolerance on the total cavity length is more stringent than the tolerances on any of the legs.

The ring cavities use spherical end mirrors at non-normal incidence. To first order, this causes the optical beam to become elliptical. The effective focal lengths in the tangential and sagittal planes are different from each other and different from the normal-incidence focal length. These two focal lengths are dependent on the angle of incidence. The effect of the angular variation on focal length is significant in the ring cavity design, and can be compensated, to first order, by appropriate design of the curvatures of the glancing-incidence mirrors.

As was indicated in Section 6.2.2, the spot size of cavities operating near the stability limit are very susceptible to variations in

focusing. This problem was analyzed for the ring cavity using the matrix formalism to obtain tolerances on the mirror focal lengths. The radii of curvature of the mirrors was adjusted independently until a 5 percent change of the spot size in the wiggler was obtained. For the ring cavity, the focal length tolerances for a 5 percent change in the spot size were found to be ≈250 μm for the end mirrors and 2.2 cm for the glancing-incidence mirror. These tolerances indicate to what level focal length distortion must be limited during FEL operation. The manufacturing tolerance for the mirrors is much larger because the effective focal length of the cavity is determined both by the focal lengths of the two mirrors forming the beam-expanding telescope and their spacing.

6.3.5 Glancing-Incidence Optics

Glancing-incidence optics have been proposed as the leading element of a beam-expanding telescope in the region close to the wiggler where the radiation flux is too high for normal-incidence optics. In such an arrangement, the spot size on the normal-incidence (or near normal incidence for a ring configuration) end mirrors can be much larger than would be possible without the additional beam divergence provided by the glancing-incidence mirrors. Consequently, the end mirrors can be moved closer to the wiggler and the total cavity round trip time is decreased. Without the glancing-incidence optics acting as beam expanders, the beam would spread slowly by diffraction, and hundreds of meters separation would be necessary between the wiggler and end mirrors.

Glancing-incidence mirrors are capable of handling high intensity due to increased reflectivity at glancing incidence as well as the enlarged illuminated surface area. If the damage mechanism is thermal, the power-handling capability ideally scales as the inverse of the square of the cosine of the incidence angle, where the angle is measured from the normal and the electric field must be perpendicular to the plane of incidence and reflection for this scaling. The glancing-incidence concept has been

identified with high-power optical systems,[6-18] although relevant performance data[6-19] exists only at 10 μm and for only modest angles.

An example of the high reflectivity at glancing incidence is given in Figure 6-6 (taken from Reference 6-20). Very near grazing incidence, light with both polarizations have the same functional dependence of reflectivity versus angle, but with widely differing coefficients. The s-wave direction is preferred when high reflectivity is necessary. If a glancing-incidence element is used at 88 degrees, the footprint of the beam is increased by a factor of 29. With a reflectivity of 0.997, the thermal problems should be manageable. This reflectivity is about what might be expected with unoxidized aluminum at the same angle. Therefore, a dielectric coating might not be necessary for some designs, although a coating would allow higher reflectivity.[6-21] If a dielectric coating is not required, the problems of dielectric coating damage (at least to the glancing-incidence element) due to UV and X-ray emission can be avoided. Such short wavelength emissions can be expected from harmonic generation in the FEL and bremsstrahlung radiation due to e-beam scraping at apertures.

Another interesting aspect of glancing-incidence optics is the relatively low surface figure requirement. The shallow grazing angles make these optics less sensitive to figure errors. For the end mirror, $\lambda/100$ figure is required, but for the glancing-incidence element the equivalent figure is only about $\lambda/4$. This difference can be roughly explained by considering the path length change experienced by a reflection off of a surface feature which differs from the nominal surface. The path length change is proportional to the cosine of the incidence angle. If a glancing-incidence element is used at 88 degrees, the ratio of cosines of the normal incidence angle and the glancing incidence angle is 29, the same ratio as the difference in figure requirement.

A Gaussian beam has a radius of curvature which depends on the axial position. The section of the glancing-incidence mirror which is physically closest to the wiggler sees a different radius of curvature than the part

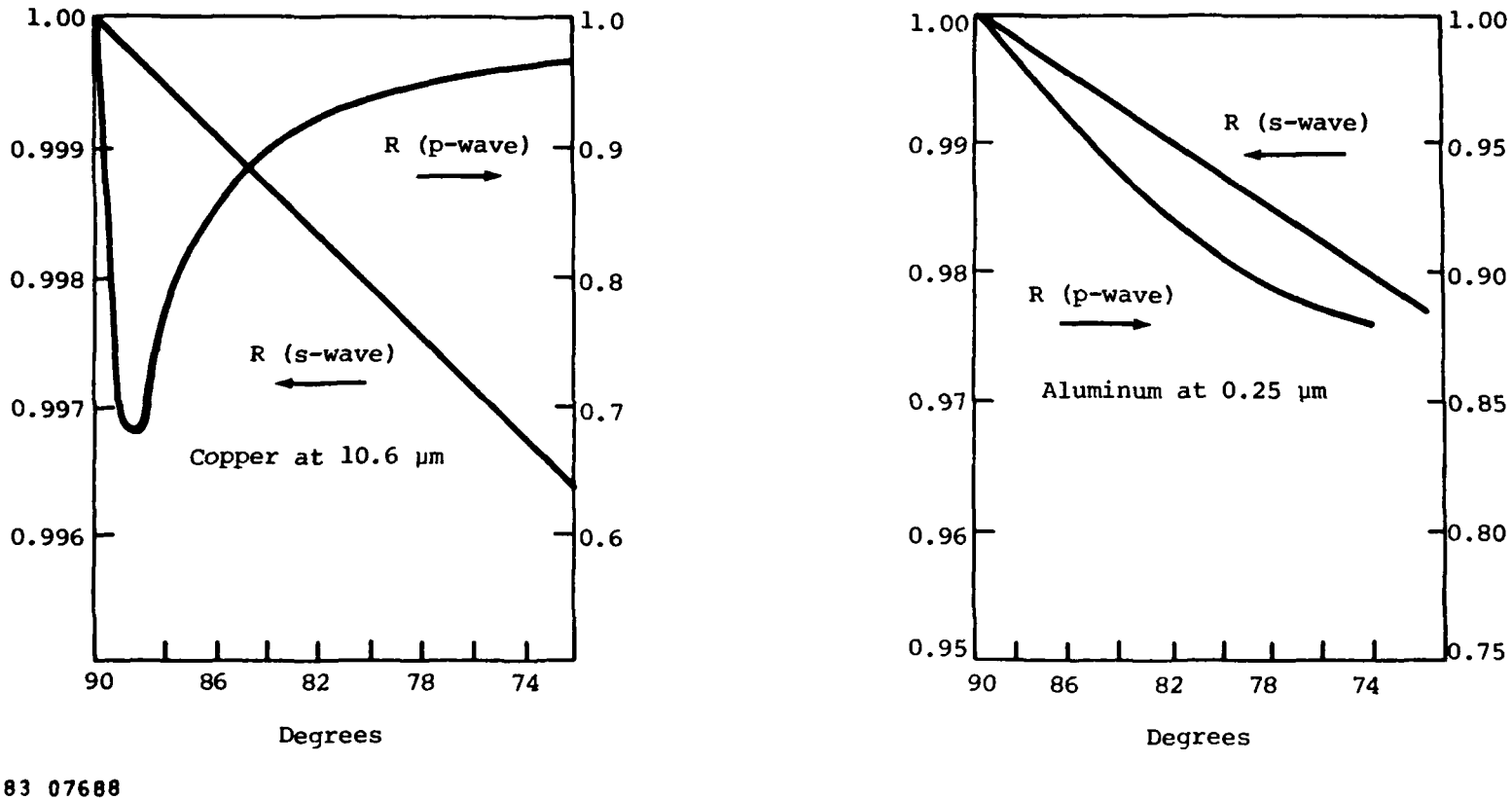

Figure 6-6. Calculated Effect of Glancing-Incidence Angle and Polarization on Reflectivity.[6-20]

which is farthest away. The desired surface shape is that which best maps a spherical wave at the wiggler to a spherical wave in the ring return leg, under the constraint that the end mirrors are spherical. This dictates that the glancing-incidence mirrors be nonspherical. For this FEL application, a best-fit circle can approximate the appropriate mirror surface fairly closely, deviating approximately 50 μm rms.[6-21] This deviation is still large by optical standards and indicates that computer controlled grinding and polishing techniques will have to be employed in the fabrication of the glancing-incidence optics.

The feasibility of construction of glancing-incident mirrors for the FEL was one of the subjects of a subcontract to Perkin-Elmer from MSNW.[6-21] The conclusion on this topic is that given the required shape, size, and heat loading on the glancing-incidence mirrors, elements could be built that meet all of the surface requirements of the high power FEL. The preferred method of fabrication of the glancing-incidence mirror is computer-controlled, cylindrical polishing coupled with metrology by mechanical profilometry. Such techniques are currently being applied at Perkin-Elmer in the Advanced X-Ray Astrophysical Facility/Technology Mirror Assembly for which the rms grazing-incidence figure error is 10 times more stringent than required for the FEL.

There are a few tradeoffs which are required for design of glancing-incidence mirrors for the FEL. To obtain a large footprint on the glancing-incidence mirror, the glancing incidence angle is decreased. But this also increases the length of the glancing-incidence mirror, increasing the difficulty and risk of fabrication. To obtain high magnification of the beam expanding telescope, the radii of curvature are decreased. As the radii of curvature are decreased, the orientation of the polarization direction of the incident light with respect to the surface changes near the edges of the mirror. Thus the reflectivity at the edges will be less than at the center. This effect is actually only important for the lateral curvature, which is far more severe than the longitudinal curvature. Also,

as the lateral radius of curvature decreases, the difficulty and risk of fabrication increase.

6.3.6 Stabilization

The ring cavity as illustrated schematically in Figure 6-3 has four elements, each of which has five degrees of freedom. As for the concentric cavity, two of these motions are not important: motion along the wiggler axis and rotation around the wiggler axis. Fortunately, not all of the angular degrees of freedom are sensitive and the lengths of the individual legs are less sensitive than the total length.

Due to the high angle of incidence of the glancing-incidence mirrors, the round trip distance of the cavity is within 1 percent of twice the distance between the end mirrors. Therefore, the total cavity round trip distance can be controlled by controlling the distance between the end mirrors. In order to maintain the magnification of the telescopes between the glancing-incidence and end mirrors, the distance between these two mirrors must be maintained to around 250 μm, which is much less stringent than the tolerance on the total cavity length. As indicated by the tolerances given in the previous section, only these three lengths would require control.

The end mirrors require angular control in both planes, but with much less restrictive angular control requirements compared to a concentric cavity of equivalent length. The angular tilt tolerance is in fact equal to that of the non-telescoped low-power concentric cavity described in Section 6.2. The pointing tolerance for the glancing-incidence mirrors is around 10 μrad which indicates that these mirrors probably only require fine positioning, but not active control.

When compared to the low-power concentric cavity, stabilization of the ring requires placing two additional linear legs under control. While stabilization requirements on the distance between the end mirrors is the

same as for the low-power cavity, the tolerance on all of the remaining angles is less stringent and the stabilization for the two additional legs is much less stringent than on the total cavity length.

6.3.7 Wavelength Selectivity and Output Coupling

Most of the considerations for outcoupling and wavelength selectivity are the same for the low-power concentric cavity and the high-power ring. When the power levels are increased, however, all the optical elements must be cooled so that transmissive optics are not suitable. This limits the choices for wavelength-selective optics and output coupling schemes. At high average powers, the leading candidates for output coupling are gratings and scrapers, and the leading candidates for sideband suppresion are gratings and frequency-selective dielectric mirrors.

For a grating to operate as a sideband suppressor, the dispersion of the grating must be large enough to misalign the sideband component and small enough that all frequency components of the desired micropulses are still aligned in the cavity. This is possible, since the transform-limited spectral width of the micropulse is much less than the sideband shift. Another requirement is efficiency. If the grating is not the output coupler, the grating efficiency should be greater than 99 percent. Another consideration which may limit the selectivity is potential cavity misalignment due to chirp during the start-up phase.

For the high-power cavity, multilayer dielectric stacks with differential reflectivity between the desired wavelength and the sideband are candidates as sideband suppressors. Requirements such as the minimum differential reflectivity, manufacturability, and the effect of excess power absorption due to reduced reflectivity must be addressed.

A grating is also a candidate for the output coupler, independent of sideband suppression. In this mode, the intracavity component comes from the specular reflection and the outcoupling arises from a higher order

diffraction. The dispersion of the grating is still limited. If the dispersion is too high, the finite frequency components of the micropulse will be dispersed in angle, reducing the effective beam quality of the outcoupled light. However, a second compensating grating may be included, in the near field of the output, to recollimate the frequency components and reproduce the orginal beam quality. Based on etched silicon technology, grating output couplers with better than 99 percent in the zeroth and first orders may be feasible.[6-22] Output coupling of greater than 20 percent should be possible. Further consideration of this technology is required to determined its applicability.

A scraper output coupler is also a viable concept. In the ring cavity, one-sided scraping, which produces a single (nonannular) output appears feasible. The major issue is the intracavity effects of the induced diffraction from the scraper. The presence of the scraper will induce spatial ripple in the beam, which may damage or distort optics, affect the spot size of the mode in a non-linear fashion, decrease the intensity of the optical beam along the optical axis, and induce additional intracavity losses due to the reduced focusability of a clipped Gaussian beam. Physical optics codes will be needed to evaluate these effects. A second problem is that the output beam is not Gaussian and therefore not diffraction limited. However, since the output is single phase, it will be close to diffraction limited.

For low-power ring cavities, the options of a near Brewster's angle plate and a multilayer dielectric tack are viable. The tilted plate becomes even more favorable than in a concentric cavity since the laser pulse travels in only one direction, thus halving the absorption and wave front distortion and providing a single output beam. This plate provides an output beam with nearly the same wave front quality as the laser pulse.

REFERENCES

6-1. S.A. Mani and J.H. Hammond, "Optics and Resonator Design Issues for High-Power Free Electron Lasers," in the Proceedings of the International Conference on Lasers '81, pp. 586-592.

6-2. W.M. Grossman and D.C. Quimby, "Scaling of Alignment Tolerances for Free-Electron Lasers," in Free Electron Generators of Coherent Radiation, C.A. Brau, S.F. Jacobs, and M.O. Scully, eds., Proc. SPIE, 453, p. 453 (1984).

6-3. A.E. Siegman, An Introduction to Lasers and Masers, McGraw-Hill Book Co., San Francisco (1971).

6.4. J.M. Eggleston, "Angularly Stable Ring Resonators for High Power FELs," in Proceedings of the International Conference on Lasers '83, December 1983.

6-5. Y.K. Danileiko, A.A. Manenkov, and V.S. Nechitailo, "The Role of Absorbing Defects in the Laser Damage of Transparent Materials," in NBS special bulletin on Laser Damage in Optical Materials (1980).

6-6. T.A. Wiggins and R.S. Reid, "Observation and Morphology of Small-Scale Laser Induced Damage," Applied Optics, 21, 1675 (1982).

6-7. B. Newnam, Personal Communication.

6-8. B.A. Boley and J.H. Weiner, Theory of Thermal Stress, John Wiley and Sons, New York (1960).

6-9. D.G. Kocher, "Automated Foucault Test for Focus Sensing," Applied Optics, 22, 1887 (1983).

6-10. J.M. Khosrofian and B.A. Garetz, "Measurement of a Gaussian Laser Diameter Through the Direct Inversion of Knife Edge Data," Applied Optics, 22, 3406 (1983).

6-11. J.T. Knudtson, "Laser Beam Spatial Analysis Using a Two-Dimensional Photodiode Array," Rev. Sci. Instrum., 54, 856-860 (1983).

6-12. Y. Ohtsuka and I. Sasuki, "Laser Heterodyne Measurement of Small Arbitrary Displacements," Optics Comm., 10, 362 (1974).

6-13. C.P. Wang, R.L. Varwig, and P.J. Ackman, "Measurement and Control of Subangstrom Mirror Displacement by Acousto-Optical Technique," Rev. Sci. Instrum., 53, 963 (1982).

6-14. C.P. Wang and R.C. Varwig, "Measurement of Phase Fluctuations in a HF Chemical Laser," J. Appl. Phys., 50, 7917 (1979).

6-15. D.R. Preuss and J.L. Gole, "Three-Stage Birefringent Filter Tuning Smoothly Over the Visible Region: Theoretical Treatment and Experimental Design," Applied Optics, 19, 702 (1980).

6-16. Gary DeBell, Spectra-Physics, Optical Coating Division, Personal Communication.

6-17. A.F. Stewart and A.H. Guenther, "Preliminary Experimental Results of Spot Size Scaling in Laser Induced Damage to Optical Coatings," in Laser Induced Damage in Optical Materials, pp. 517-532 (1981).

6-18. P.B. Mumola, et al., "Advanced CO_2 Laser Fusion Driver Concepts," in Proceedings of the Lasers '80 Conference, December 1980.

6-19. J.F. Figueira and S.J. Scott, "Damage Thresholds at Metal Surfaces for Short Pulse IR Lasers," IEEE J. Quant. Elect., QE-18, 1381 (1982).

6-20. P.B. Mumola and D.C. Jordan, "Glancing Incidence Optics for High Power Lasers," SPIE Proceedings, Vol. 288, pp. 54-62 (1981).

6-21. P.R. Akkapeddi and P.E. Glen, "FEL Optics," Perkin-Elmer Corporation, Danbury, Connecticut, October 1983.

6-22. P.B. Mumola, Perkin-Elmer Corporation, Private Communication.